Development of New Techniques for Three Dimensional Tracking of Charged Particles for Possible Applications in the Search for Neutrinoless Double Beta Decay

Entwicklung neuer Techniken für die dreidimensionale Spurrekonstruktion geladener Teilchen für eine mögliche Anwendung bei der Suche nach dem neutrinolosen doppelten Betazerfall

der Naturwissenschaftlichen Fakultät
der Friedrich-Alexander-Universität Erlangen-Nürnberg
zur Erlangung des Doktorgrades Dr.rer.nat

vorgelegt von
Mykhaylo Filipenko
aus Kiew

ERLANGEN CENTRE FOR ASTROPARTICLE PHYSICS

IMPRS physics of light

Als Dissertation genehmigt von der Naturwissenschaftlichen Fakultät
der Friedrich-Alexander Universität Erlangen-Nürnberg

Tag der mündlichen Prüfung:	23.02.2015
Vorsitzender des Promotionsorgans:	Prof. Dr. Jörn Wilms
Gutachter:	Prof. Dr. Gisela Anton Prof. Crister Fröjdh

Contents

Zusammenfassung

Seitdem der neutrinolose doppelte Betazerfall 1937 als Möglichkeit vorgeschlagen wurde, die Majorana-Natur des Neutrinos nachzuweisen [1], beschäftigt die Suche danach schon mehrere Generationen an Experimentatoren. Auf der einen Seite würden sich mit einem Nachweis dieses sehr selten, hypothetischen Zerfalls eine Reihe von bedeutenden Fragen der Teilchenphysik beantworten lassen. Auf der anderen Seite jedoch ist das ganze Unterfangen mit einer Vielzahl an Herausforderungen verbunden, die gemeistert werden müssen.

Die schwierigste Aufgabe besteht darin, das gesuchte Signal von möglichen Untergrundsignalen unterscheiden zu können, da die Wahrscheinlichkeit, dass der gesuchte Zerfall stattfindet sehr, sehr klein ist. Um eine Unterscheidung zwischen verschiedenen Zerfällen machen zu können, muss die Energie gemessen werden. Zusätzlich könnte das Messen der Trajektorie der Zerfallsteilchen bedeutend dabei helfen, Signal und Untergrund voneinander zu trennen.

Im Rahmen dieser Promotion wurden verschiedene Techniken entwickelt und erprobt, um solche Trajektorien vermessen zu können und experimentell gezeigt, dass anhand der Trajektorien eine Unterscheidung verschiedener Zerfallsarten tatsächlich möglich ist. Mit dem Timepix, einem hybriden Halbleiterdetektor, der 1 mm Cadmium-Tellurid als Sensormaterial hatte, wurden zweidimensionale Spuren von comptongestreuten Elektronen und Elektron-Positron Paaren gemessen. Mit Hilfe von künstlichen neuronalen Netzen konnten beide Ereignistypen voneinander unterschieden werden. Anschließend wurde zum ersten mal gezeigt, dass sich mit dem Timepix Detektor dreidimesionale Spuren von hochenergetischen Elektronen im Halbleitersensor rekonstruieren lassen.

Weiterhin wurde ein neues Konzept erarbeitet, um dreidimesionale Teilchenspuren anhand von Szintillationslicht rekonstrukieren zu können. Dieses konnte bei einem Erstversuch erfolgreich angewendet werden, um dreidimensionale Spuren von hochenergetischen Elekronen zu rekonstruieren. Dazu wurde ein neuer Detektor - der hybride Photonendetektor - verwendet, dessen absolute Quanteneffizienz im Vorfeld mit der Methode von Klyschko vermessen wurde.

Abstract

Since its prediction in 1937 [1], several generations of experimental physicists have tried to confirm the neutrinoless double beta decay. An observation would have fundamental consequences for the understanding of particle physics. However, the experimental requirements are very demanding wherefore the race is still ongoing between many collaborations.

The main challenge in this field is the reduction of background. Any decay in the natural decay chain is orders of magnitude more likely than the neutrinoless double beta decay. The half-life of this decay is known to be longer than 10^{25} years. Therefore, any detector will see a vast majority of events which are not signal events. Such events have to be identified and rejected. Primarily, this is done by measuring the kinetic energy of the decay products but also the trajectory of the particles resulting from the decay can be used for identification.

Within the scope of this thesis different techniques were developed and tested which can be used to record such trajectories. It was shown that trajectories can be used indeed to identify and distinguish different types of events. The hybrid semiconductor detector named Timepix was used to record two-dimensional tracks of Compton-scattered electrons and electron-positron pairs in a 1 mm thick cadmium-telluride sensor layer. Artificial neural networks could successfully be employed to distinguish both event types. Furthermore, a "proof-of-principle" experiment was successfully performed where three dimensional trajectories of high energetic electrons could be reconstructed from data recorded with a similar Timepix detector.

Also, a new concept, where three dimensional trajectories of ionizing particles are imaged by scintillation light, was developed and successfully tested. In a "proof-of-principle" experiment three dimensional trajectories of high energetic electrons through a scintillator were reconstructed from data taken with a novel single photon detector - the hybrid photon detector. Beforehand the detector's absolute quantum efficiency was determined with the method of Klyshko.

I Introduction

With the recent discovery of the Higgs-Boson the Standard Model of particle physics is complete. Does this mean that physicist who work in the field of elementary particle physics are going to be unemployed soon? The answer is definitively no. There is overwhelming evidence for physics beyond the standard model, i.e. experimental data which we are not able to understand within the framework of the standard model. Two prominent examples are indirect observations of dark matter and the observation of neutrino oscillations. Reasonable explanation for the observed phenomena can be given by different extensions to the standard model. Further important predictions of these theories can be tested in so called low-background experiments.

A specific example for such an experiment is the search for neutrinoless double beta decay. The prediction is that particular nuclei can undergo a very rare decay where two neutrons within the nucleus decay to two protons and two electrons; and no antineutrinos are emitted. Hence, the name - neutrinoless double beta decay. As no antineutrinos are emitted the electrons carry away the full Q-value of the decay as their sum kinetic energy. So far, so good but what makes this prediction so exciting?

A couple of facts: First of all, the decay violates lepton number conservation. Secondly, the decay can occur only if the neutrino is a Majorana particle and consequently its own anti-particle - a total exception in the case of fermions. Both facts give direct evidence to physics beyond the standard model and would make it unavoidable to extend the standard model by the framework of Majorana particles. Until now, the observation of neutrinoless double beta decay (or the neutrinoless double electron capture) is the only way to definitely proof the Majorana character of neutrinos (and anti-neutrinos). At last, from the half-life of neutrinoless double beta decay capable nuclei, one can calculate the effective Majorana mass and draw conclusions about the neutrino mass hierarchy - an unsolved problem of particle physics and cosmology.

Essentially, one can say, that the search for neutrinoless double beta decay bears an enormous potential for new discoveries in particle physics. Of course, these discoveries are not for free - the technical requirements for such experiments are at least as high as the possible benefits for the physics community: A very large amount of nuclei under investigation and therefore a large detector mass are necessary. At the same time, a good energy resolution and as little background as possible are inevitable.

Talking about backgrounds - what is background in the case of a neutrinoless double decay experiment? Background is any kind of ionizing radiation that will deposit as much

energy as the Q-value of the particular neutrinoless double beta decay in the sensitive detector volume. Since the decay under observation is very rare, any kind interaction of the sensitive volume with an ionizing particle such as α-, β- or γ-particle that is released from a decay in the natural decay chain or from cosmic radiation, is way more probable that the actual decay. This will produce false positive events and eventually lead to wrong conclusions.

The conventional way to deal with background is to reduce external background by shielding and internal background by using radiopure materials for detector fabrication. Yet, no matter how radiopure the detector components are and how thick the shielding is, some background events might still occur in the detector and lead to false positive event.

A different way to deal with background is to use active background suppression techniques (instead of only passive ones). One of these techniques is particle identification by tracking: Since different types of particles will have different propagation trajectories through the sensitive detector volume, a pixelated detector can be used to detect two dimensional trajectories (of these particles) and distinguish them. However, three dimensional trajectories provide way more information for particle identification and therefore it is desirable to have a detector technology which makes it possible to acquire three dimensional trajectories. The scope of this thesis was to investigate the feasibility for the realization of a detector which can provide three dimensional trajectories of particles propagating through its sensitive volume.

For this purpose two different detectors were used. Firstly, a Timepix-detector with a cadmium-telluride sensor was used which makes it possible to measure two dimensional tracks of ionizing radiation propagating through its sensor layer. Single electron tracks from Compton-scattering and pair-production events, generated by 2.6 MeV photons from a ^{208}Tl source, were measured and artificial neural networks were successfully applied to distinguish between both types of events. The result demonstrated that the idea of active background reduction by tracking works in general but as simulations show three dimensional trajectories promise much better separation power.

This was the starting point to investigate how a detector could be constructed that can fulfill this goal: A similar Timepix-detector was used for a "proof-of-principle" experiment of three dimensional particle tracking in a semiconductor layer. Ahead of the experiment, an algorithm was developed by my colleague, Thomas Gleixner, which is capable to reconstruct three dimensional tracks from data which could be acquired with an optimized, specific pixelated semiconductor detector. Although the Timepix does not have all the functionality required for this method, we could successfully reconstruct electron tracks from data that was taken at the DESY T-22 beam line with 4.4 GeV electrons. Such particles can be regarded as minimal ionizing and therefore produce straight tracks within the sensor layer as well as deposit nearly the same energy in every pixel. This provides the additional information that cannot be acquired with the Timepix detector but is needed for the reconstruction algorithm.

Although a Timepix detector with a thin sensor layer can provide valuable tracking information, one can imagine that it is hard to built up a large mass experiment from sensors which have a mass of only 1.2 g each. One could think about thicker sensors but there is a physical limitation to the sensor thickness if tracking should be possible and that limitation is set by diffusion. If charge carriers (like in a semiconductor detector) are drifted vertically across the sensor volume they diffuse horizontally at the same time. After some centimeters of drift, it is hardly possible to see a nice trajectory since the trajectory information is smeared out by diffusion.

A possibility to overcome this problem is to use the scintillation signal (photon signal) instead of the ionization signal for tracfking. This requires a detector which is able so detect single photons and provide spatial and temporal information about them simultaneously. Such a detector is the hybrid photon detector, a novel device based on a photocathode, a stack of micro channel plates and four Timepix-ASICs. The third part of this thesis is about the operation and calibration of this detector. Here, the goal was to determine the absolute quantum efficiency for optical photon detection which was performed by the method of Klyshko in collaboration with the Max-Planck Institute for the Physics of Light.

In the forth part a "proof-of-principle" experiment for particle tracking by scintillation light is presented. The idea of the experiment was to image multiple two dimensional projections of electron tracks through a scintillator onto the HPD and reconstruct three dimensional tracks from these projections. The optical setup consisted of a plastic scintillator, two lenses, two mirrors and the HPD. Data was taken at the DESY T-24 beamline with electrons of 5 GeV and their tracks through the scintillator could successfully be reconstructed.

The manuscript is structured as follows: The second chapter gives an introduction to the neutrinoless double beta decay, the common experimental techniques in the field and recent experimental results. The third chapter presents the two publications about tracking and three dimensional track reconstruction with cadmium-telluride Timepix detectors. Chapter four presents both publications which involve the application of the hybrid photon detector. In chapter five, the results are summarized and an outlook on possible improvements is given.

II The Neutrinoless Double Beta Decay

Contents

II.1 A Short Introduction to the Theory of Neutrinoless Double Beta Decay

The double beta decay ($2\nu\beta\beta$) is a forth-order weak process where two neutrons in a nucleus decay to two protons, two electrons and two antineutrinos:

$$\begin{aligned} 2n &\rightarrow 2p + 2e^- + 2\bar{\nu}_e \\ {}^{136}\mathrm{Xe} &\rightarrow {}^{136}\mathrm{Ba} + 2e^- + 2\bar{\nu}_e \quad \text{(example)} \end{aligned} \tag{II.1}$$

This process is possible if a nucleus is in an energy state as shown in Fig. II.1a: A usual beta decay would be possible if the state E_t was energetically favorable, i.e. $E_t < E_i$ but this is not the case. Only the state E_f is energetically favorable ($E_f < E_i$) and therefore such nuclei decay by a double beta decay. Under particular conditions, which are described below, such a nucleus could also decay by the so-called neutrinoless double beta decay ($0\nu\beta\beta$):

$$\begin{aligned} 2n &\rightarrow 2p + 2e^- \\ {}^{136}\mathrm{Xe} &\rightarrow {}^{136}\mathrm{Ba} + 2e^- \quad \text{(example)} \end{aligned} \tag{II.2}$$

There are about 60 natural nuclides capable of this decay. The most fashionable ones concerning experiments are listed with their most important properties in table II.1. The Feynman diagram of this process is shown Fig. II.1b. As no antineutrinos are present in the final state (i.e. are not emitted in the decay process), the lepton number conservation is violated. Thus, $0\nu\beta\beta$ is a process which can only take place if physics beyond the standard model exists. Two additional theoretical assumptions beyond the standard model are necessary to describe this process:

First of all, in the standard model the neutrino and the antineutrino are regarded as two different particles. In a beta decay, an antineutrino is emitted whereas in an inverse beta decay, a neutrino is absorbed by the neutron and a proton and an electron are present in the final state. The neutrinoless double beta decay can be regarded as a simultaneous occurrence of both processes. However, since in the beta decay an antineutrino is involved (i.e. going out from the vertex) and in the inverse beta decay a neutrino (i.e. going into the vertex), one has to assume that a conversion mechanism exists or that the condition $\bar{\nu}_e \equiv \nu_e$ is fulfilled (i.e. the neutrino is its own anti-particle). In fact for the first time this idea was proposed by Ettore Majorana in 1937 [2], wherefore neutrinos which fulfill this property are referred to as Majorana neutrinos.

Besides the mechanism shown in Fig. II.1b, where the neutrino is assumed to be a Majorana-particle, other mechanisms are theoretically possible which predict the existence of $0\nu\beta\beta$ as well. Several mechanisms have been proposed and discussed in the past, like the emission of a Majoron or the exchange of SUSY-particles between the vertices II and III (see [6, 10]). However, in 1982 Schlechter and Valle could prove that, if the $0\nu\beta\beta$ truly exists, the neutrino is a Majorana particle indeed - no matter what kind of mechanism is

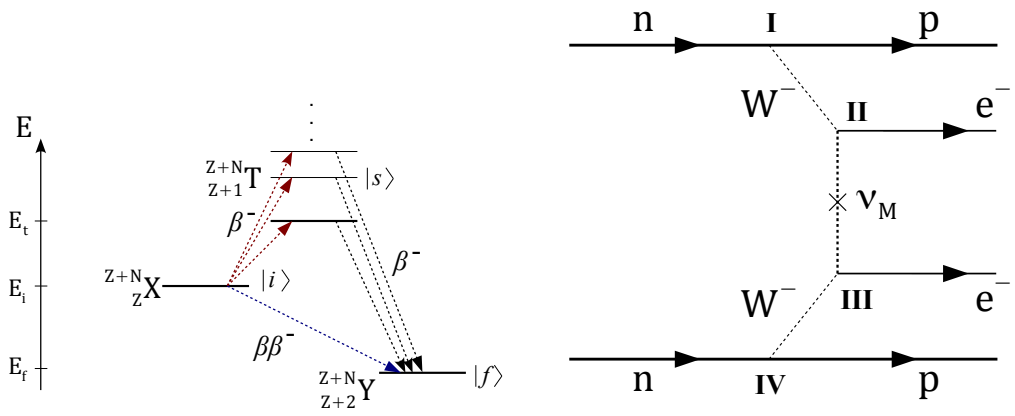

Figure II.1: a) Energy levels (schematic) of a nucleus capable of the double beta decay. The transition to the state E_t by a single beta decay is not possible. A second-order transition can happen to the state E_f by a double beta decay. b) Feynmann diagram of $0\nu\beta\beta$ in the case of Majorana neutrino exchange.

responsible for the decay to happen [4].

Secondly, in the standard model the neutrino is regarded as a massless particle. However, due to evidence from neutrino oscillation experiments, neutrinos seem to have a small but non-zero rest mass. This is also required in the case of $0\nu\beta\beta$ due to the following reason: Neutrinos can couple to W^--bosons only if they are left-handed and antineutrinos only if they are right-handed. Therefore between both vertices (II and III), the neutrino/antineutrino has to flip helicity. The helicity H of particle can be written as

$$H = \frac{\vec{s} \cdot \vec{p}}{|\vec{s}|\,|\vec{p}|}, \tag{II.3}$$

where $\vec{s}$ is the spin and $\vec{p}$ the momentum of the particle. Therefore, the helicity can flip if the direction of the momentum changes, i.e. if such a reference frame can be found that $\vec{p}$ changes its sign. This is only possible if the particle travels with a speed slower than the speed of light and therefore must have a non-zero rest mass. Details about the theory of $0\nu\beta\beta$ can be found in [7, 8, 9, 10].

The idea to use the neutrinoless double beta decay in order to proof the Majorana nature of neutrinos dates back to 1937 [1]. In order to examine how realistic this goal is, the half-life $T_{0\nu}^{-1}$ of nuclides which are capable of $0\nu\beta\beta$ had to be derived [3]. It is given by the following formula [5]:

$$T_{0\nu}^{-1} = G_{0\nu}(Q_{\beta\beta},Z)\,|M_{0\nu}|^2\,\frac{|m_{\beta\beta}|^2}{m_e^2} \tag{II.4}$$

The first expression on the right hand side $G_{0\nu}(Q_{\beta\beta},Z)$ is the phase space volume of the process which depends on the full Q-value ($Q_{\beta\beta} = E_i - E_f$) of the decay and the mass number of the nucleus Z. The second factor $M_{0\nu}$ is the transition matrix element which

Isotope	$Q_{\beta\beta}$ [keV]	Natural Abundance [%]	Lower limit on $0\nu\beta\beta$ half-life [a]
^{76}Ge	2039	7.44	$2.2 \cdot 10^{25}$
^{130}Te	2528	33.799	$1.8 \cdot 10^{24}$
^{116}Cd	2814	7.49	$1.7 \cdot 10^{23}$
^{136}Xe	2458	8.9	$3.4 \cdot 10^{25}$
^{48}Ca	4272	0.187	$5.8 \cdot 10^{22}$
^{100}Mo	3034	9.63	$1.1 \cdot 10^{24}$
^{82}Se	2995	8.73	$3.6 \cdot 10^{23}$
^{150}Nd	3367	5.64	$1.8 \cdot 10^{22}$

Table II.1: A list of important isotopes capable of double beta decay with their Q-value, natural abundance and measured limits on the half-life. Values were taken from [10, 21, 20, 24, 44].

incorporates the dynamics of the transition, i.e. properties of the particular nuclei that are involved in the transition. The last factor is the effective Majorana-mass $|m_{\beta\beta}|$. Although the formula for the half-life takes this simple form, the calculation of the individual parts is complex.

The easiest part is the phase-space volume which is a known integral over the momentum space of all final states. Numerical values can be found in [8]. In contrast to this calculating the transition matrix elements $M_{0\nu}$ is a highly non-trivial task. Several methods have been developed over the past 30 years to cope with this problem. Details about these methods can be found in [16]. Among others the most common methods are IBM-2 (Interacting Boson Model), QRPA (quasiparticle random phase approximation) and LSSM (Large Scale Shell Model) which are compared in [17]. The results of the different methods for several nuclides are shown in Fig. II.2. They have relatively high uncertainties and the results may differ from each other for particular nuclides by almost a factor of 2. The exact knowledge of the matrix elements is important for a precise determination of the effective Majorana mass $|m_{\beta\beta}|$ by inverting formula II.4 after measuring $T_{0\nu}$.

In contrast no value or constraints can be derived solely from theory for the effective Majorana mass $|m_{\beta\beta}|$ which is defined as

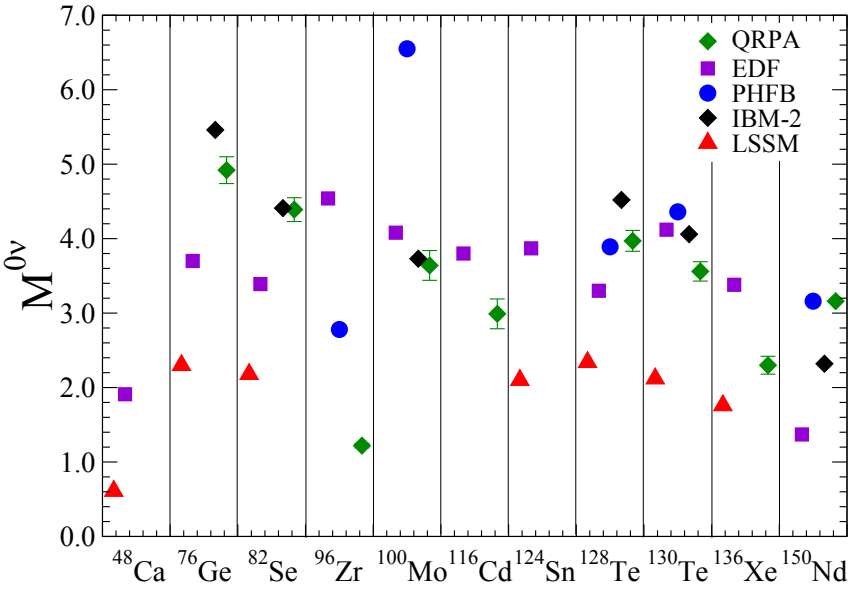

Figure II.2: Matrix elements for different $0\nu\beta\beta$ nuclei calculated with IBM-2, QRPA and LSSM approaches. Taken from [8].

$$|m_{\beta\beta}| = \left| \sum_i {U_{ei}}^2 m_i \right|, \tag{II.5}$$

where m_1, m_2 and m_3 are the masses of the three neutrino mass eigenstates and U_{ei} are the elements of the PMNS-mixing matrix [20]. The PMNS-mixing matrix describes the probability of a particular neutrino flavor eigenstate to be found in a particular mass eigenstate. As the factors U_{ei} are complex numbers, a problem for experiments arises. It is illustrated in Fig. II.3a and II.3b: If one assumes an optimistic scenario, nature has chosen the phases α_i in such a way that $|m_{\beta\beta}|$ is large enough and the $0\nu\beta\beta$ can be observed experimentally. On the other hand if a pessimistic scenario is assumed, the phases cause a cancellation ($|m_{\beta\beta}| \approx 0$) or such a small effective Majorona mass that an observation is practically impossible. The whole parameter space is shown Fig. II.5 where the absolute value of the effective Majorana mass is plotted versus the lowest neutrino mass $m_{\nu,low}$. The outer right area is disfavored by results from cosmology; the outer top area is excluded by results of past experiments. The NS area belongs to the normal mass scenario ($m_1 < m_2 < m_3$) and the IS area to the inverted scenario ($m_3 < m_1 < m_2$) [8].

The neutrino mass hierarchy is another unsolved problem of neutrino physics: From neutrino oscillation experiments only two neutrino mass differences (Δm_{12} and Δm_{23}) could be determined so far. Hence, the arrangement of the neutrino masses allows for three different scenarios which are shown in Fig. II.4; which one is chosen by nature is unknown until now [11]. The knowledge about the three possible hierarchies puts strong constraints on the effective Majorana mass as shown on the plot in Fig. II.5. On the other hand, if a value for the effective Majorana mass can be determined experimentally, it would nail down the neutrino mass hierarchy and solve another fundamental problem of neutrino physics.

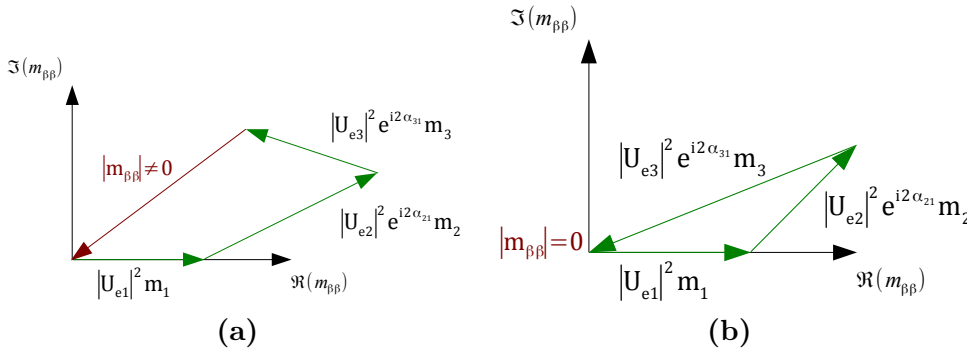

Figure II.3: Two random examples of possible scenarios for Majorana phases. In the first case (a) the Majorana phases have such values that $|m_{\beta\beta}| \approx 0.2$ eV and an experimental observation is possible. In the second case (b) the Majorana phases cause an effective Majorana mass of $|m_{\beta\beta}| \approx 0$ which is impossible to observe experimentally.

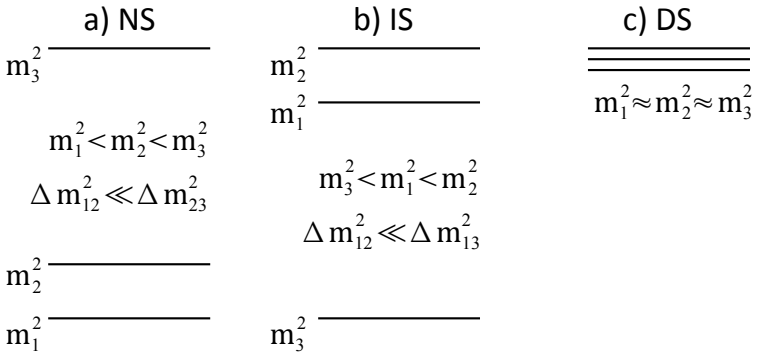

Figure II.4: Schematic visualization of the three possible scenarios for the neutrino mass hierarchy: a) normal scenario; b) inverted scenario; c) quasi degenerate scenario.

At this point it is also interesting to broach the implications for $0\nu\beta\beta$ which emerge if models with sterile neutrinos are considered [11]. Such models assume that there are more than three neutrino flavors and those additional neutrinos cannot interact electromagnetically, weekly or strongly (with other particles). Their existence can be proven by neutrino oscillation: A SM neutrino (electron, muon or tau) could oscillate into a sterile neutrino and thus disappear from our observations. If we know the total neutrino flux, we will measure less neutrinos that we would expect. Currently, such models are widely discussed in theory and several experiments are running to measure this kind of neutrino disappearance [13]. For a scenario with one sterile neutrino the parameter space for $|m_{\beta\beta}|$ and $m_{\nu,low}$ is shown in Fig. II.6a and II.6b, respectively. The plot on

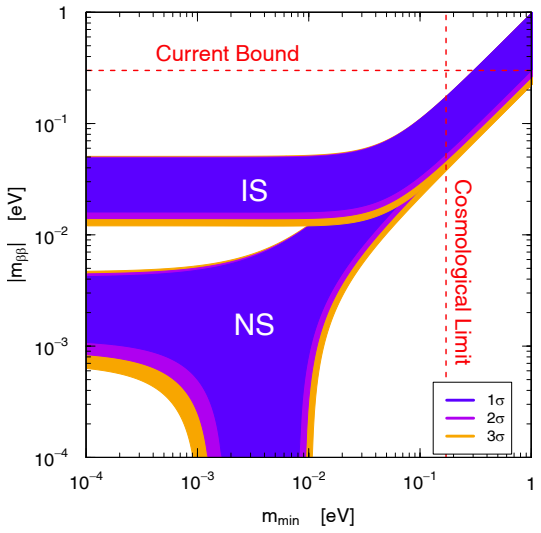

Figure II.5: The constraints on the effective neutrino Majorana mass $|m_{\beta\beta}|$ for the different neutrino mass hierarchies. The two bands represent the inverted scenario (IS) and the normal scenario (NS), respectively. Taken from [8].

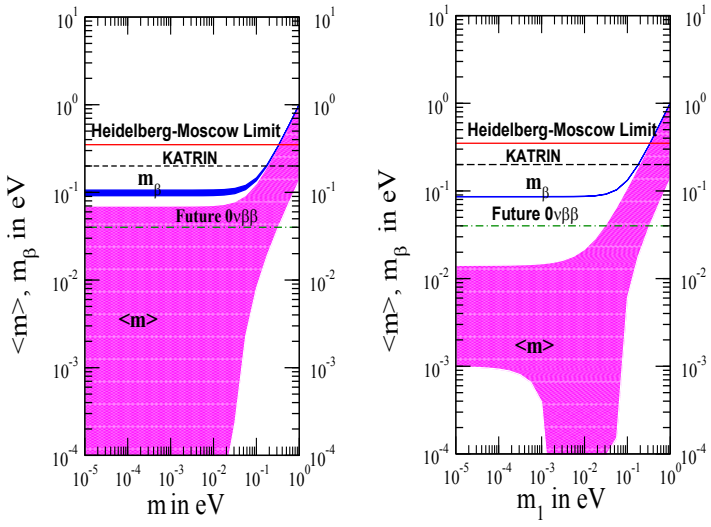

Figure II.6: The parameter space (pink) for $|m_{\beta\beta}|$ in the case of one sterile neutrino. The left plot corresponds to the normal scenario and the right to the inverted scenario. The blue area are the constraints for the neutrino mass $|m_{\beta\beta}|$ which can be determined in tritium-decay experiments like KATRIN [12]. The plots are taken from [11].

the left corresponds to the normal hierarchy whereas the plot on the right refers to the inverted hierarchy with one sterile neutrino. Here, the sterile neutrino is assumed to be the heaviest in a 4-neutrino mass hierarchy. Apparently, in such a case neither the effective Majorana mass $|m_{\beta\beta}|$ has practical constraints which are motivated by the neutrino mass hierarchies[1] nor a knowledge about $|m_{\beta\beta}|$ can be used to conclude which neutrino mass hierarchy is chosen by nature.

II.2 Experimental Methods and Techniques

II.2.1 Detector Mass and Energy Resolution

The starting point for experimental considerations is the expected half-life for $0\nu\beta\beta$ decays: $T_{0\nu} > 3.4 \cdot 10^{25}$ a (for ^{136}Xe, [44]). It ultimately dictates the mass of the experimental setup which is required to make an observation. This fact is easy to understand if one assumes the (obviously) unrealistic scenario that there are no backgrounds for $0\nu\beta\beta$. In this case, after an observation time T (also often called exposure time), the number of observed $0\nu\beta\beta$ events (which is the number of decayed nuclei since there are no backgrounds) is given by

1 All regions which would be excluded by the neutrino mass hierarchy argument are already excluded by direct search for $0\nu\beta\beta$.

$$N(t) = N_0 - N_0 \cdot \exp\left(-\frac{T \ln 2}{T_{0\nu}}\right). \tag{II.6}$$

N_0 is the number of nuclei at the beginning of the experiment: $N_0 = \frac{m}{m_A} \cdot N_A \cdot \varepsilon$, where m is the mass of the experiment in kg, m_A the atomic mass of the isotope, N_A the Avogadro constant ($N_A = 6.0233 \cdot 10^{23} \frac{1}{mol}$) and ε the degree of enrichment of the isotope within the detector. On a practical time scale exposure times between 1 and 5 years are considered to be reasonable and an enrichment grade of about 80 % is feasible. Therefore, to be able to detect at least five $0\nu\beta\beta$ event on this time scale, the detector mass has to be at least

$$M > 30\,\text{kg}. \tag{II.7}$$

This basically points out the first main challenge for experimentalists: Any detector technology that is suitable to be used for $0\nu\beta\beta$ search must be scalable to large masses at reasonable cost and reliably operate for a long time.

During its operation the detector must measure the sum energy of the two electrons which are created during a $0\nu\beta\beta$ decay. As in the case of $0\nu\beta\beta$ the full decay energy is shared only amongst the two electrons, one expects to measure a distinct peak at the Q-value. However, every nucleus which can undergo $0\nu\beta\beta$ is also able to decay via $2\nu\beta\beta$; and this decay will happen with a much higher probability since $2\nu\beta\beta$ is not forbidden in the standard model. In this case the energy is shared amongst four particles, namely two electrons and two antineutrinos, wherefore a broad energy distribution is measured for the energy sum of the two electrons. If an ideal detector, which means a detector with perfect energy resolution, was used for the experiment, an energy spectrum as shown in Fig. II.7 should be measured with a broad distribution for $2\nu\beta\beta$ (blue) and a prominent peak (red) at the Q-value for $0\nu\beta\beta$ (assuming the decay exists and the experiment has enough mass and exposure time).

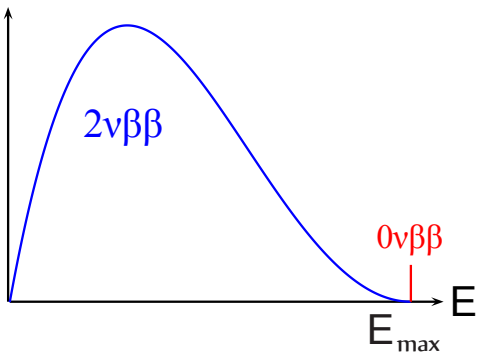

Figure II.7: The expected schematic spectrum of a $0\nu\beta\beta$ nuclide measured with an ideal detector. The blue distribution is produced by $2\nu\beta\beta$ whereas the prompt peak (red) at the Q-value is due to $0\nu\beta\beta$. Taken from [14].

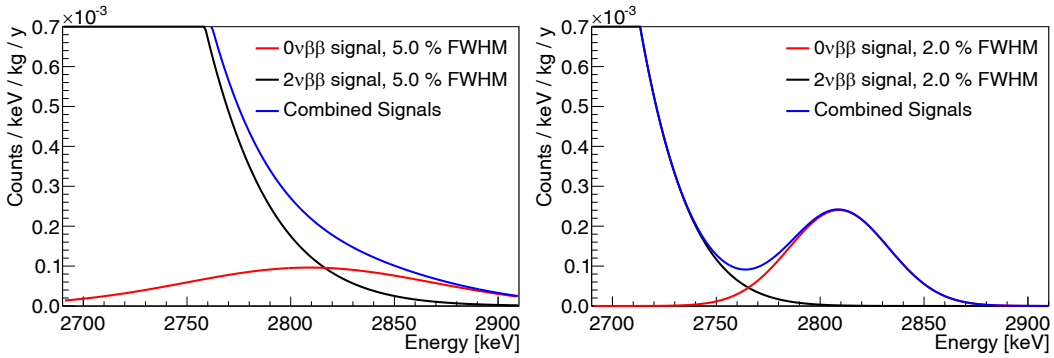

Figure II.8: The $2\nu\beta\beta$ and $0\nu\beta\beta$ spectrum of ^{116}Cd around the Q-value (2.814 MeV) as expected to be measured with a detector of 5.0 % FWHM (left) and 2.0 % FWHM (right) energy resolution at the Q-value. The half-lifes are assumed to be $T_{0\nu} = 2.9 \cdot 10^{19}$ a ($2\nu\beta\beta$) and $T_{0\nu} = 1 \cdot 10^{26}$ a ($0\nu\beta\beta$). Even if no other backgrounds existed, still a sufficient energy resolution is required to distinguish between $2\nu\beta\beta$ and $0\nu\beta\beta$ events. Taken from [14].

Unfortunately, in reality detectors always have a finite resolution and therefore $2\nu\beta\beta$ provides an unavoidable background to $0\nu\beta\beta$. The energy resolution $Res(E_0)$ of a detector is the ratio between the full width at the half maximum (FWHM) of a peak and the peak average energy E_0 if the peak is fitted with a Gaussian distribution:

$$Res(E_0) = \frac{FHWM_{keV}(E_0)}{E_0} = 2.355\frac{\sigma_{keV}(E_0)}{E_0}. \tag{II.8}$$

In Fig. II.8 a zoom around the Q-value is shown. The plots show the theoretical prediction for the double beta spectrum measured with a ^{116}Cd detector system with an energy resolution of 2.0 % (FWHM) and 5.0 % (FWHM), respectively [14]. The half-lifes for $2\nu\beta\beta$ and $0\nu\beta\beta$ are assumed to be $T_{2\nu} = 2.9 \cdot 10^{19}$ a ($2\nu\beta\beta$) and $T_{0\nu} = 1 \cdot 10^{26}$ a ($0\nu\beta\beta$). Thus, the $0\nu\beta\beta$ peak is really tiny compared to the $2\nu\beta\beta$ spectrum. At an energy resolution of about 2.0 % it is clearly separated whereas an energy resolution of 5.0 % is not sufficient any more. The larger the $0\nu\beta\beta$ half-life actually is, the better the detector resolution has to be. This comparison is illustrated in Fig. II.9 (taken from [15]). If a half-life of $6.7 \cdot 10^{23}$ a is assumed, the peak can be resolved at an energy resolution of 4.0 %; however, this is not the case if the half-life is larger than $1.6 \cdot 10^{25}$ a .

In order to fulfill these two requirements - a large detector mass and a good energy resolution - most experiments are designed in such a way that the decaying material is used as the sensitive volume of the calorimeter. This has two advantages: The first one is that the electrons go through the sensitive volume immediately after their decay and hence no energy is lost during the propagation through non-sensitive volume. This reduces the uncertainty in the energy measurement and increases the energy resolution. Secondly, this allows to built detectors with a good volume-to-surface ratio which can be used to

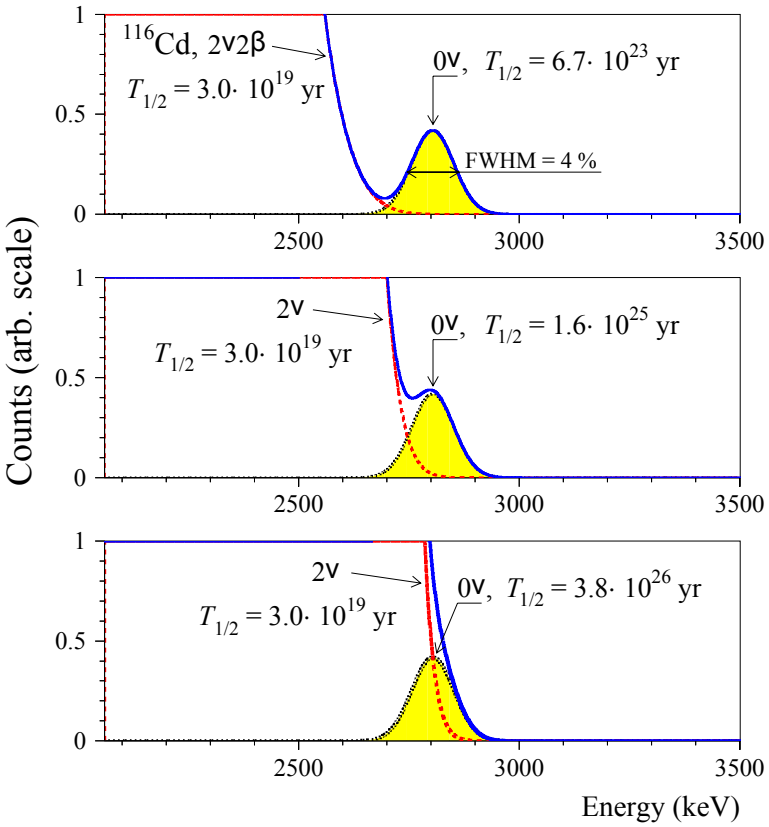

Figure II.9: The $2\nu\beta\beta$ and $0\nu\beta\beta$ spectrum of ^{116}Cd around the Q-value (2.814 MeV) as expected to be measured with a detector of 4.0 % (FWHM) energy resoultion. Depending on the actual half-life of $0\nu\beta\beta$ the energy resolution might be not sufficient to distinguish between $2\nu\beta\beta$ and $0\nu\beta\beta$ events. Taken from [15].

assign a so-called fiducial volume within the detector: If a position sensitive detector is used, events on the detector surface are rejected and only events within an "inner volume" - the fiducial volume - are taken into account as non-background events. Past and currently running experiments have proven fiducializing to be a valuable technique to reduce the background level for $0\nu\beta\beta$ by orders of magnitude because most background is provided by contamination on detector surfaces or from surroundings in the underground laboratories in which $0\nu\beta\beta$ experiments are normally located [23].

II.2.2 Backgrounds

In this subsection a detailed review on radioactive backgrounds for $0\nu\beta\beta$ will be given. Backgrounds are events due to any kind of radiation but not $0\nu\beta\beta$ which occur in the sensitive detector volume and deposit as much energy as the Q-value [28]. They can be confused with the $0\nu\beta\beta$ if no further information about the event is provided and hence give a false positive although no actual $0\nu\beta\beta$ event occurred. It turned out to be the most

important task for $0\nu\beta\beta$ experiments to understand deeply which sort of background can occur and how it can be avoided or rejected after data analysis. For any $0\nu\beta\beta$ experiment it is also important to know the composition of its background since particular types of backgrounds are very easy to deal with whereas some backgrounds are very hard to get rid off. In principle, there are five main sources of background which are listed below:

α-particles from natural decay chains (mostly from ^{238}U, ^{235}U and ^{232}Th decay chains). Such events occur usually on the detector surface due to contamination within the detector electronics. This type of background is the easiest to be rejected by fiducializing, pulse shape discrimination and tracking. As the penetration depth of α-radiation is very small (a few micrometers in solids and liquids), α-radiation from the outside of the detector can be shielded easily.

Muons which are usually produced in cosmic ray showers. To avoid this background the detector is placed into an underground facility. The rock above the detector is basically used as shielding from the muons coming from the sky. This way the muon flux can be reduced by more than 6 orders of magnitude [29] (Labr. Nat. del Gran Sasso). As muons have a high mass and travel nearly at the speed of light, they behave like minimal ionizing particles which penetrate the complete detector on a straight line. In order to reject muon events from the data, one can take advantage of this fact and construct either a muon veto, which is in principle a scintillation detector panel (above the actual detector) run in coincidence, or use a tracking detector for identification of the straight muon lines within the sensitive detector volume.

Electrons from β-decays can produce surface events if they are due to contamination in the detector electronics but also provide background events within the sensitive volume. Electrons from β-decays have a wide energy spectrum which can go up to above 10 MeV for a large variety of nuclides, and therefore can always make the detector click exactly at the Q-value. What makes this kind of background especially challenging is that the β-decay can be followed by **internal conversion** (IC) or **Møller-scattering** (Fig. II.10a). In the first case the nucleus is in an excited state after the β-decay and instead of emitting a photon the nucleus falls back to ground state by transferring its energy to an electron in the shell which is emitted. In the case of Møller-scattering the electron from the β-decay scatters-off an electron from a nearby atom. Both processes takes plac on a time scale of 10 to 100 ps wherefore they both have the same signature as a $0\nu\beta\beta$ event if the sum energy of both electrons is at the Q-value. Most elements have β-decaying isotopes and there are β-decaying isotopes in all natural decay chains. Thus, it is hardly possible to avoid this background completely [28]. Although electrons from the outside can be shielded easily, this is not possible for electron background from inner parts of the detector. Tracking (e.g. with pixelated detectors) and can be applied to reduce single electron background.

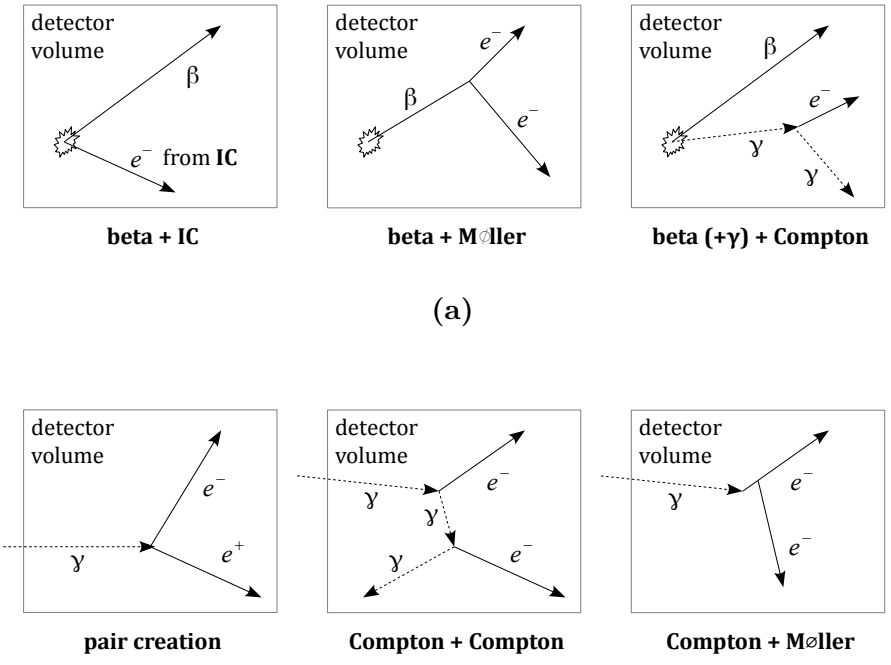

Figure II.10: Radioactive backgrounds that can be caused by β- (a) and γ-radiation (b). Adopted from [28].

Photons with high energies can be emitted after any kind of radioactive decay and penetrate the complete detector volume. Such photons can be shielded from outside up to a particular level - but never completely, since this would require a very high amount of shielding material around the detector which in turn contains radioactive material. Within the detector photons can produce single electrons by photoabsorption or Compton-scattering (Fig. II.10b). Additionally, two electrons can be produced either by double Compton-scattering, Compton-scattering followed by photoabsorption or after a single electron production process followed by Møller-scattering. Another possible process is electron-positron production. Fortunately, all photons from natural decay chains do not have enough energy to produce electron-positron pairs at the Q-value of most $0\nu\beta\beta$ isotopes used for experiments. A discrimination of single-site versus multi-site events (two events which happen at different parts of the sensitive volume simultaneously) can be used to reduce Compton-scattering background (for instance by pulse shape discrimination or tracking).

Neutrons with low kinetic energies can penetrate the complete detector and do not produce background events by themselves since they are neutral. However, neutrons can be captured by any nucleus. This leads to an excitation of the nucleus and during relaxation primary photons but also electrons or α-particles can be emitted. Neutrons are

usually created outside of the detector and can be shielded by hydrogen-rich materials like water (moderation of fast neutrons), paraffin or boron (capture of slow neutrons).

II.2.3 Signal Readout Techniques

As next the focus should be switched to technical aspects, namely to the methods of signal acquisition. If a $0\nu\beta\beta$ event occurs in a solid or liquid material[1] the two electrons from the $0\nu\beta\beta$ lose a significant fraction of their energy already on the first 100 µm of their trajectory. If the sensor is placed outside of the decaying material the uncertainty in the depth of the decay leads to a decrease in energy resolution. To avoid this problem, most experiments use the decaying material as the detector's sensor. When the electrons (primary particles) propagate through the sensor, scattering processes inside of the sensor lead mainly to the production of secondary particles: These are free electrons (plus holes or ions), photons and phonons.

Every type of secondary particle can be used to determine the energy deposited by the propagating electrons within the sensor volume since the amount of secondary particles, that are created, is proportional to the energy deposited by the ionizing radiation: $N_{sp} \propto E_{dep}$. This number can be calculated as $N_{sp} = \frac{E_{dep}}{W_{eff}}$[2], where W_{eff} is the effective ionization energy for the particular kind of secondary particle. The effective ionization energy is the average energy which is required to create one secondary particle. It is higher than the real excitation energy because it takes losses into account. Losses in this case are the creation of secondary particles which do not contribute to the particular signal. For instance, if a silicon semiconductor detector is considered, only the charge signal (collection of electrons or holes) can be read out and the excitation of photons and phonons is considered as losses. The excitation energy for an electron-hole pair in silicon is about $E_g = 1.1\,\text{eV}$ (the band gap) but $W_{eff} = 3.61\,\text{eV}$. For the charge signal the effective ionization energy can roughly be approximated as [31]

$$W_{eff} = 2.2E_g + \frac{\lambda_i}{\lambda_h} E_r. \tag{II.9}$$

In formula II.9 E_g denotes the energy gap between valence and conduction band, λ_i and λ_h the mean free path of the ionizing particle between electron and phonon collisions, respectively, and E_r the highest energy of optical phonon modes.

1 At this point, only materials in their solid or liquid phase are considered since almost all materials that have $0\nu\beta\beta$ capable nuclei are solid or liquid regarding their use as detector sensor.

2 As described below this number is not fixed but undergoes fluctuations that lead to a finite energy resolution for any real detector.

Free electrons are produced basically in an electron-electron scattering process. If the material is in a gaseous or liquid phase, electron-ion pairs are produced; in a solid material electron-hole pairs are created and the electrons in the conduction band are considered as free. Free electrons can be drifted by an electric field and collected at an anode. In the case of solid state detectors sometimes the holes are collected instead (at a cathode) if the mobility (and drift velocity) of the holes is higher. This is often referred to as charge or ionization signal.

The number of secondary electrons created at a fixed deposited energy is not constant but undergoes fluctuations as cross-sections give only probabilities for a process to occur. These fluctuations give the physical limit for the energy resolution which can be achieved using a particular detector material. In 1947 Fano could derive the expression

$$\sigma_{Fano} = \frac{\sigma_{keV}(E_0)}{E_0} = \sqrt{F \cdot \frac{W_{eff}}{\varepsilon \cdot E_0}} \tag{II.10}$$

for the smallest relative width which can be achieved with a detector if there are only fluctuations in the number of free charge carriers created during the ionization process [33]. This relative width is often called the "Fano-limit" for the energy resolution of a detector measuring the energy E_0. The factor F in formula II.10 is called the Fano-factor. It is a material-specific constant which is often determined experimentally. ε is the efficiency of signal collection. If other effects of broadening like electronics-noise, DAC noise, thermal noise, dark current noise etc. are taken into account they add up quadratically to the full width:

$$\sigma_{full} = \sqrt{\sigma^2_{Fano} + \sigma^2_{elect} + \sigma^2_{DAC} + \sigma^2_{thermal} + ..} \tag{II.11}$$

Consequently, it is necessary to eliminate any source of noise to achieve the Fano-limit with a detector. For different types of materials the Fano-limit varies drastically. In table II.2 the Fano-factor F, the effective excitation energy W_{eff} and the typical collection efficiency are given for some materials widely used in detector applications.

Detectors based on the charge signal have big advantages if thin sensors (usually made of semiconductors) or materials with a sufficient free electron life-time (e.g. highly purified noble gases) are used. In fact, the working principle of such a detector is simple: Free electrons (or holes, for example in case of silicon) are drifted towards the cathode (or anode). They are either collected at the cathode (or anode) or induce mirror currents in the cathode (or anode). This leads to a current pulse which is integrated. The integral gives an information about the deposited energy.

The advantages of semiconductors like silicon are the relatively low Fano-factors and low effective ionization energies W_{eff} to produce one electron-hole pair. In the case

Material	Fano-Factor F	W_{eff} [eV]
LAr	0.11	23.6
LXe	0.06	15.6
GXe	0.15	21.9
HPGe	0.13	3.0
Si	0.12	3.6
CdTe	0.09	4.43

Table II.2: A list of typical materials used for detectors based on charge collection. Values taken from [31, 35]. G = gaseous, L = liquid, HP = high-purity.

of highly purified germanium detectors (HPGe) an energy resolution of 0.2 % at 2 MeV can be achieved [23]. This value differs from the Fano-limit by less than a factor of 1.5. Detectors based on cadmium-telluride (CdTe) have slightly worse energy resolution but the advantage of a higher detection efficiency for high-energy photons and room-temperature operation. The disadvantages of semiconductor detectors (for instance with a ^{116}Cd(Zn)Te sensor) for $0\nu\beta\beta$ applications are the high costs to manufacture and process high quality semiconductor crystals and to make them radiopure. This limits the size of experiments that can practically be built with this approach.

A part of the free electrons can recombine with ions (or holes) and release the excitation energy as photons. Furthermore, in scintillating materials photons can be created due to various other mechanism like the de-excitation of excitons, excited atomic levels or exited dimer states [35, 36]. If a sensor material is used which the photons can escape from, photomultiplier PMTs), avalanche photodiodes (APDs) or silicon photomultipliers (SiPMs) can be placed outside of the sensor volume to detect the photons. This signal is called the light or scintillation signal.

For scintillation detectors, the achievable energy resolution is usually determined by the quantum efficiency of the PMT and the number of photons which are produced per 1 MeV of energy deposited by the ionizing radiation. Typical values for widely used scintillator materials are given in table II.3. The energy resolution of scintillation detectors ranges usually from about 3 % to 15 %. In Fig. II.11 the same spectrum is shown twice, once measured with a NaI scintillation detector and a second time with a HPGe detector [32]. The enhancement in energy resolution with germanium is obvious.

There are several reasons for this: The effective excitation energy to produce a photon is high (compared to around 3 eV for an electron-hole pair in a semiconductor) and can go up to several 100 eV. Additionally, the Fano-factor is 1, which is about an order of magnitude larger than for semiconductor detectors, and the detection efficiency[1] of PMTs, especially for photon energies higher then 7 eV (in this case often a wavelength-shifter has

1 The detection efficiency of a PMT is often called quantum efficiency.

to be used) is low. Despite the moderate energy resolution (compared to other signals), the scintillation signal has a number of advantages which makes it useful in many applications:

Firstly, for the detection of photons PMTs are used which is an old, cheap and widely established technology. A scintillation detector is usually easy to realize: A scintillation material is optically connected to a PMT or a module of PMTs. The scintillator and the PMTs are shielded from background optical photons by metal and black paper to reduce the noise in the PMT. Ionizing radiation leads to the excitation of states in the scintillator and after deexcitation, the photons travel through the scintillator and are detected in the PMTs.

Secondly, if a fast scintillator[1] is used, the photons arrive at the PMTs within few nanoseconds, even in a large detector. Also, modern PMTs can deliver their signal pulse within some nanoseconds. Silicon photomultipliers can work even faster. This combination makes the scintillation signal a good choice for trigger applications. At last, for really large detector volumes the light signal has the advantage that it can travel through the sensor material without being absorbed within the sensor itself (depending on the self-attenuation of the material). For instance, free electrons have usually a limited life-time and therefore large detectors are more difficult to realize because of signal loss during electron transport. Also, photons do not diffuse like electrons (or holes) on their way through the sensor.

The third possibility is to exploit the phonon or heat signal. Phonons are quanta of lattice vibrations and can be created either by direct scattering of ionizing radiation with the lattice or by relaxation of electrons which were excited by the ionizing radiation from the valence into the conduction band beforehand. Phonons cannot be detected as individual particles but as a rise in the material's temperature. For this purpose usually transition edge sensor (TES) are used which are placed at the surface of the sensor volume. Transition edge sensors are very precise bolometers constructed from superconductors which are held at transition temperature from the superconducting to the normal conducting state. At this temperature the gradient $\frac{\mathrm{d}R}{\mathrm{d}T}$ is very high and therefore

Material	Photons per MeV	λ[nm]	τ [ns]
CsI(Tl)	60000	540	800
NaI	76000	303	60
$CdWO_4$	7000	530	15000
LAr	37000	130	7
LXe	47600	180	2

Table II.3: A list of typical scintillator materials used for detector applications. The rows contain the values for the number of photons per MeV, the central emission wavelength and the decay time. Taken from [34, 35].

1 Fast in this context means, that the deexcitation of populated states takes place within less than nano- or hundreds of picoseconds.

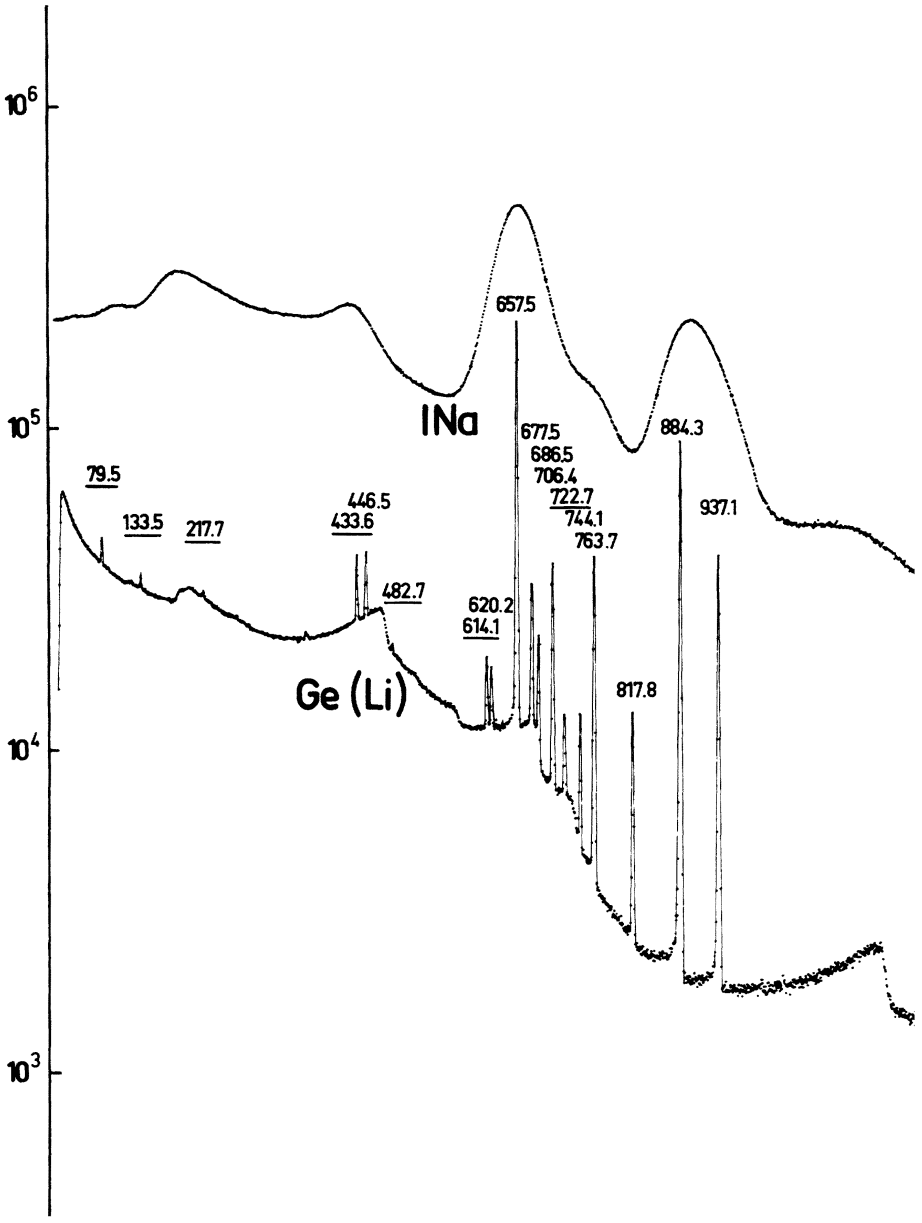

Figure II.11: Comparison between a spectrum from a ^{110}Ag source measured with a high purity germanium and a NaI scintillation detector. Taken from [32].

by measuring the resistance of the superconductor one gets a very sensitive bolometric device. As superconductors are involved and the change in temperature caused by the primary particles has to be above the temperature fluctuations of the sensor material, very low temperatures ($< 100\,\mathrm{mK}$) are required to use this technique.

Phonon based detectors (or bolometers) come into play, if one desires to push the energy resolution down as low as possible. The reason for this is that phonons have very low excitation energies. Therefore, the resolution limit is several orders of magnitude lower than for any kind of scintillation or charge based calorimetric detector. The absolute resolution limit for a bolometric calorimeter can be calculated by

$$\Delta E_{FWHM}[\mathrm{eV}] = 2.355\sqrt{4k_B T c_V V}, \tag{II.12}$$

where k_B is the Boltzmann-constant, T the temperature of the detector system, V the detector volume and c_V the specific heat of the detector [37]. With typical values ($T_0 = 0.1\,\mathrm{K}$, $c_V \approx 1\frac{J}{m^3 K}$) the energy resolution for a tiny detector $V \approx 100\,\mu\mathrm{m}^3$ can be as good as $\Delta E = 10\,\mathrm{eV}$. This is more one order of magnitude better than with any charge or scintillation based detector and can be pushed even further by cooling down and using materials with lower c_V. However, the cryogenic efforts can easily rule out the gains in energy resolution.

In the case of bolometers the sensor material is usually read out with a small TES attached to the sensor material. As the TES is much smaller than the sensor, only a few percent of the phonons are actually detected. But even with collection efficiencies of less than 1% bolometric detectors still provide the best energy resolution for a calorimeter that is possible up to now. The drawback of this technology are the low and stable temperatures in the range of 10 mK that are required for the detectors to run. This, of course, is a cost issue and makes it very expensive to built large scale setups.

II.2.4 Detector Segmentation

All of the signals can be used to detect tracks of the propagating particles. This can be done by a detector segmentation. Tracking can provide a powerful tool to perform active background rejection during the data analysis. In the case of PMTs many individual small size PMTs can be used and a center of gravity method applied to reconstruct tracks. The position resolution which is usually achieved this way is 1 mm to 2 mm. Hence, only sufficiently long tracks of several centimeters can be resolved [38]. Far better is the position resolution with semiconductor detectors where either the cathode or anode is pixelated. Modern CCDs are available with a pixel size of 2 µm which is good enough to resolve tracks with a length of only 50 µm. Hybrid active pixel detectors have a pixel size of about 50 µm to 100 µm and tracks with a length of about one millimeter can be well resolved. Some examples are shown in Fig. II.12 which are tracks from different kind of ionizing radiation detected with a 110 µm pixel pitch Timepix detector [39]. Bolometric

detectors can be segmented up to a pixel size of 75 µm to 200 µm but only on a small area ($< 1\,\mathrm{cm}^2$) so far [40].

II.2.5 Experimental Sensitivity

Suppose now, one can build a bunch of different experiments combining various signals and methods of passive or active background rejection. How to compare these? In the end, what counts is the lowest effective Majorana-mass $|m_{\beta\beta}|$ that can be measured in the experiment if the $0\nu\beta\beta$ exists. This quantity is called the sensitivity of a $0\nu\beta\beta$ experiment and calculated as the upper limit that can be set on $|m_{\beta\beta}|$ if no $0\nu\beta\beta$ event is measured in the experiment. First, the sensitivity for a background free experiment is given (Eq. II.13):

$$|m_{\beta\beta}| = K_1 \sqrt{\frac{n_\sigma}{\varepsilon MT}} \tag{II.13}$$

Here, M is the detector mass and T the exposure time. The product of both, MT (usually given in kg · year), is called the exposure. ε is the detection efficiency and K_1 a constant only depending on the isotope of choice. n_σ is the confidence level of the result in σ. However, an ideal experiment can hardly be realized in reality; if finite energy resolution

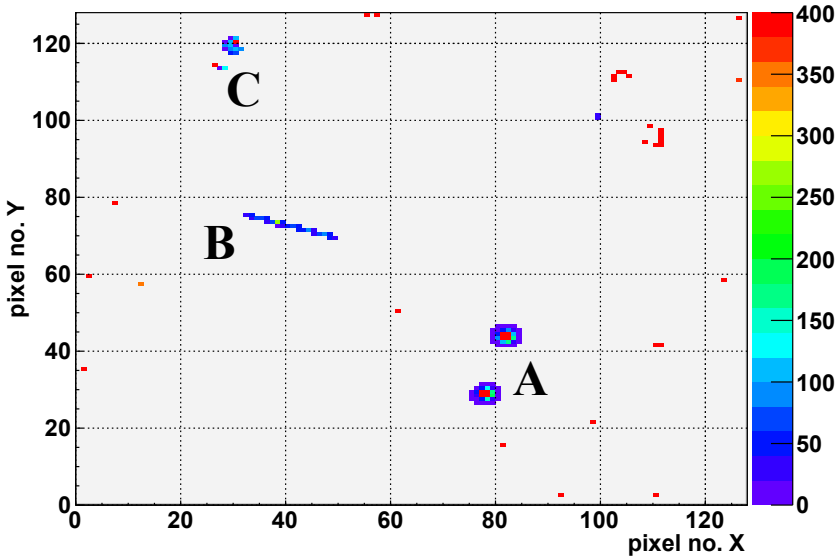

Figure II.12: Image of deposited energy in the pixels of a CdTe Timepix detector during an exposure time of 5 s. The color denotes the energy deposition in keV. One can deduce that two α-particles (A), a muon (B) and an electron (C) have interacted with the sensor. Single red dots (and multiple only red dots next to each other) are noisy pixels. Taken from [39].

and non-neglectable background are taken into account the sensitivity can either be calculated accurately by a numerical method described in [22] or in approximation it is given by

$$|m_{\beta\beta}| = K_1 \frac{1}{\sqrt{\varepsilon}} \left(\frac{b\Delta E}{MT} \right)^{\frac{1}{4}}. \tag{II.14}$$

In this formula, ΔE is the energy resolution (FWHM) of the detector in keV and b the background level. The background level is the number of non $0\nu\beta\beta$ events per keV, kg and year around the Q-value in the interval ΔE. The important message contained in formula II.13 and II.14 is that sensitivity scales with the square root of exposure in an ideal experiment but only as the forth root in the case of an experiment with background. Both cases are shown in Fig. II.13a and II.13b, respectively. For the ideal case pure expectations for different isotopes are shown whereas for the realistic scenario the values from current and proposed experiments are used. As one can see, the impact is immense. For example, in the case of ^{76}Ge about one order of magnitude in sensitivity is lost for large exposures at a background of $1 \cdot 10^{-3} \frac{\text{cts}}{\text{keV} \cdot \text{kg} \cdot \text{a}}$ (which is already low and hard to achieve).

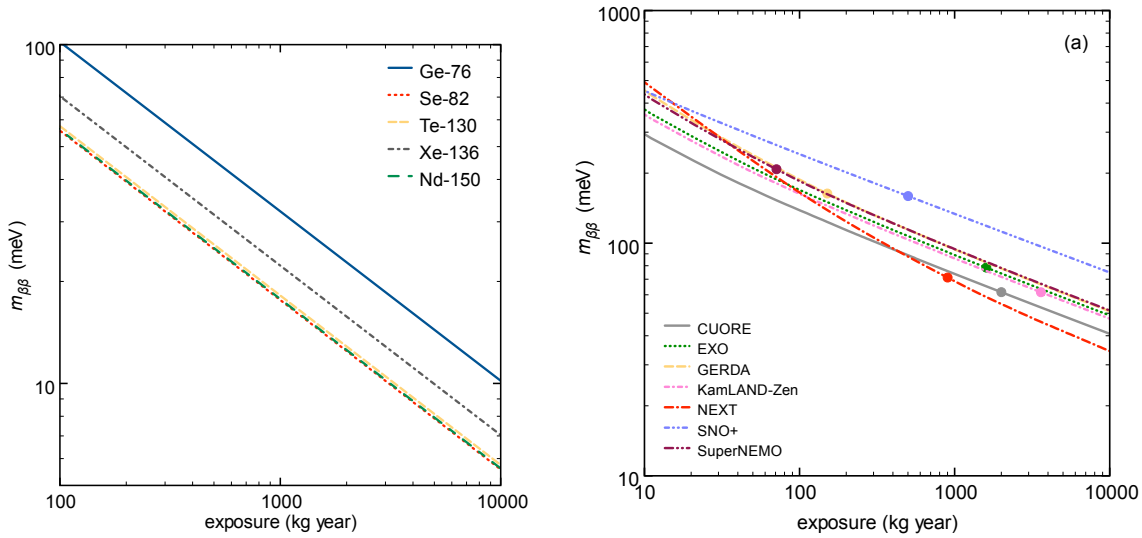

(a) **(b)**

Figure II.13: Sensitivity in effective Majorana mass $|m_{\beta\beta}|$ plotted against exposure for an ideal experiment (a) and for real proposed experiments (b). Taken from [22].

II.2.6 Important Experiments and Results

The first important experimental result on the double beta decay was the observation of the neutrino accompanied double beta decay ($2\nu\beta\beta$) by Inghram and Reynolds in 1950 [30]. They proved its existence for ^{130}Te and measured a half-life of $T_{2\nu} = 1.4 \cdot 10^{21}$ a with a geochemical technique. A claim that $0\nu\beta\beta$ has been observed for ^{76}Ge was published in 2004 by H.V. Klapdor-Kleingrothaus et al. [19]. The claim (published by a part of the Heidelberg-Moscow collaboration) is based on over 10 years of data taken with an array of high purity germanium detectors with a total mass of 11 kg of enriched germanium. The experiment was performed by the Heidelberg-Moscow collaboration in the Gran Sasso Underground Laboratory [18]. According to Ref. [19] the $0\nu\beta\beta$ half-life of ^{76}Ge is supposed to be $T_{0\nu}(^{76}\text{Ge}) = 1.19 \cdot 10^{25}$ a. The community responded critically to this result [25] which was ruled out by the GERDA collaboration in 2013 [24].

The GERDA experiment [23] is the successor of Heidelberg-Moscow/IGEX (International Germanium Experiment). The GERDA collaboration made significant progress in reducing the background level with HPGe detectors by radiopurity material studies, pulse shape discrimination and other techniques. In the current Phase-I of the experiment they ruled out the Klapdor-claim (Fig. II.14) and set a limit of $T_{0\nu} > 3.0 \cdot 10^{25}$ a for the half-life of ^{76}Ge [24] (in combination with the data from previous experiments). Their goal is to achieve a background level of $10^{-3} \frac{\text{cts}}{\text{keV} \cdot \text{kg} \cdot \text{a}}$ and a sensitivity of $2 \cdot 10^{26}$ a (90 meV). A similar goal in sensitivity (81 meV) has the experiment CUORE which plans to use TeO_2 crystals under cryogenic conditions as bolometers [41]. The isotope under investigation is ^{130}Te. The experiment should consist of 988 bolometers with a total isotope mass of 204kg.

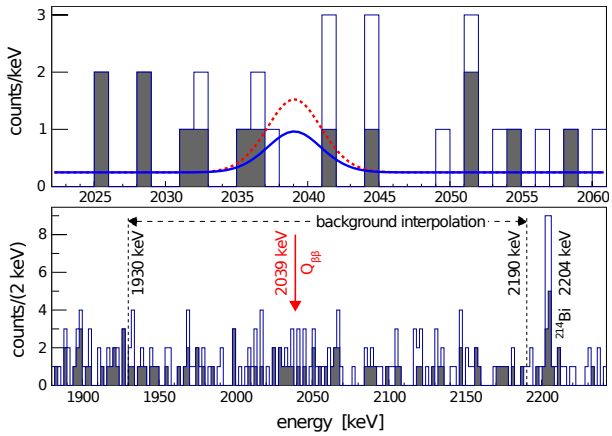

Figure II.14: The result of GERDA Phase-I. The plot shows the combined energy spectrum of all detectors around $Q_{\beta\beta}(^{76}\text{Ge})$ with (filled) and without (open) pulse shape discrimination. The expectation from the claim in Ref. [18] is shown as red dashed and the curve corresponds to the limit on $T_{0\nu}(^{76}\text{Ge})$ according to the results from GERDA Phase-I. Plot taken from [24].

A different detector concept is realized within the scope of the Super-NEMO experiment [28]: The Super-NEMO detector contains the isotope as a thin-foil within a magnetic field surrounded by a tracker and calorimeter. By this approach many different isotopes can be investigated and therefore the NEMO collaboration has set the $0\nu\beta\beta$ limits for a big variety of double beta isotopes. Currently, the use of ^{150}Nd (and ^{82}Se) are considered as they have a high Q-value and a preferable, large matrix element. The intended sensitivity is about $2.6 \cdot 10^{25}$ a (70 meV).

The other major category of experiments are based on noble gas time projection chambers (TPCs) filled with enriched ^{136}Xe. The basic functionality of a time-projection chamber is shown schematically in Fig. II.15: A noble gas is filled in a cylinder where the top plane contains PMTs and the inner volume contains two meshes: One at the top (cathode) and one at the bottom (ground). An electric field is applied over the inner cylinder volume between the meshes. Ionizing radiation creates excited xenon atoms, excited dimers, free electrons and ions. The excited states fall back to ground state and a part of the free electrons recombines with the ions. This gives rise to the scintillation signal which is detected with the PMTs. It is usually called S1 in the case of noble gas TPCs. The other part of the free electrons drifts towards the mesh G. Here, two planes of crossed wires (or pixelated detectors) are used to measure the charge signal (called S2). By the time difference between S1 and S2, the drift speed v_d and a 2D segmentation of the wires (or the PMTs), the 3D position of an event within the sensitive volume (or even the track topology) can be reconstructed.

The main modern neutrinoless double beta experiment using liquid xenon is EXO which could observe the neutrino accompanied double beta decay ($2\nu\beta\beta$) for ^{136}Xe for the first time [42]. Currently, a TPC[1] with 200 kg of enriched xenon is taking data. The

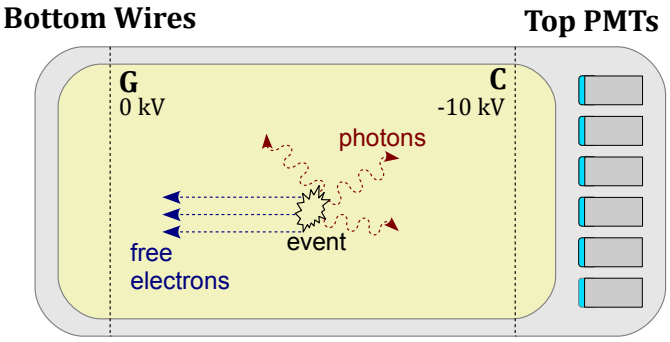

Figure II.15: Scheme of a time-projection chamber (TPC): During an event scintillation light and free charge carriers are generated. The scintillation light is detected with the PMTs (S1). The charge carriers drift in an electric field towards the ground mesh (G) where they are measured by wires or a pixelated structure (S2).

1 The EXO TPC differs in many details from the simple schematic TPC shown in Fig. II.15.

results on the first run were recently published and set a limit of $T_{0\nu} > 1.9 \cdot 10^{25}$ a for the $0\nu\beta\beta$ half-life of ^{136}Xe. The energy resolution at the Q-value is about 4 % (FHWM) at a background level of $1.5 \cdot 10^{-3} \frac{\text{cts}}{\text{kg} \cdot \text{year} \cdot \text{keV}}$ [46]. For the next phase the background should be reduced further by about two orders of magnitude and the isotope mass increased to 5 t (nEXO). EXO also plans to implement the concept of barium tagging for enhanced background rejection. The idea of barium tagging is that after a double double beta decay the xenon is transformed into barium which has to be extracted from the xenon and detected in an ion trap. The demonstration of single barium ion detection in an ion trap was successful but it has remained an unsolved problem to extract the barium out of the liquid xenon. The overall goal is to reach a sensitivity of less then 25 meV (with barium tagging and 5 t of ^{136}Xe).

A second notable neutrinoless double beta experiment with ^{136}Xe is NEXT [38] which employs xenon in the gaseous phase under high pressure (5 to 10 bar). The TPC used for NEXT has an array of silicon photomultipliers installed at the bottom and also a second mesh (A) below the mesh G. In the space between the meshes G and A such a high electric field is applied that free electrons can excite but not ionize the gas multiple times ($\approx$ 10000 times per electron) on their way between the meshes. This way an amplification of the charge signal (S2) is achieved which is detected by the PMTs (at the top plane) and by the array of silicon photomultipliers (at the bottom plane) as a light signal. The advantage is that a better energy resolution can be achieved due to the amplification and a track topology can be measured for each event by the array of silicon photomultipliers (at the bottom plane). This topology should be used for background rejection.

An important competitor of EXO is Kamland-Zen. In this experiment enriched ^{136}Xe is dissolved in a liquid scintillator which is filled into a spherical tank. The walls of the tank are equipped with photomultipliers. Only the scintillation signal is measured. For shielding, this spherical tank is placed into a second outer tank filled with a liquid scintillator only (with out xenon dissolved in it). The main disadvantage of this concept is the energy resolution of the detector. However, the concept has two advantages: On the one hand its simplicity in signal read-out makes it possible to reach large exposure masses easier. On the other hand the large volume of the detector is well suited for background reduction by fiducializing. In Phase-I the mass of ^{136}Xe in the detector was 179 kg. In December it was increased to 383 kg and it is planned to increase the mass up to 600 kg and then to 1 t in the next years. A combined analysis of the recent Kamland-Zen and EXO-200 data gives a result of $T_{0\nu} > 3.4 \cdot 10^{25}$ a for the half-life of ^{136}Xe which corresponds to a limit on the effective Majorana mass of $|m_{\beta\beta}| < 120\,\text{meV} - 250\,\text{meV}$ [44]. This is the best upper limit set for the effective Majorana mass so far.

III Tracking Capabilities of Timepix Detectors with a Cadmium-Telluride Sensor

Contents

The Timepix detector is a pixelated semiconductor detector which was originally developed for X-ray imaging applications by the Medipix collaboration together with EUDET [45]. It is a hybrid active pixel detector, i.e. the sensor layer and the signal read-out chip (ASIC) are two separate pieces which are connected to each other via bump-bonds. This allows to combine the ASIC with different sensor materials. Besides silicon, Timepix detectors with cadmium-telluride can be fabricated. Cadmium-telluride offers high X-ray absorption efficiency, allows a good energy resolution for spectroscopic applications and (in contrast to germanium) can be operated at room-temperature.

The Timepix is not only a photon-counting detector but has also a spectroscopic mode (called "time-over-threshold") which allows to measure the energy deposited in every pixel by an ionizing particles in the sensor layer; and a temporal mode (called "time-of-arrival") which allows to measure when a particular pixel was triggered by an ionizing particle. Therefore, if an ionizing particle (like an electron from a β-decay of ^{113}Cd) is created and stopped within the sensor layer completely, one can measure the particle's initial kinetic energy and also its two dimensional trajectory through the sensor layer due to the pixelation. This feature makes the Timepix technology an interesting candidate for a neutrinoless double beta decay experiment with active background rejection by tracking since both cadmium and tellurium have isotopes capable of the neutrinoless double beta decay.

The COBRA collaboration has the goal to observe the neutrinoless double beta decay of ^{116}Cd. ^{116}Cd is the isotope of choice since its Q-value is 2.814 MeV which is above the energy of any γ-photon that can be emitted from a radioactive nucleus in the natural

decay chains. Enriched cadmium should be used to grow cadmium-telluride (or cadmium-zinc-telluride) crystals that should be employed into a large number of semiconductor detectors. These detectors are supposed to run in an underground facility for several years. Cadmium-zinc-telluride is usually used as a sensor material for coplanar-grid detectors which are not pixelated and cadmium-telluride for pixelated detectors such as the Timepix. Although coplanar-grid detectors cannot provide particle tracks, they have a main advantage: It is easier to fabricate coplanar-grid detectors with good energy resolution and larger sensors.

In order make a choice which kind of detector should rather be used for a large scale experiment, one has to compare the gains in sensitivity by active background rejection to the losses in sensitivity due to the reduced efficiency (and energy resolution) of pixelated detectors (compared to coplanar-grid detectors). A detailed measurement of the energy resolution for a Timepix detector after its calibration is presented in the first paper. It also covers the separation between measured single electron and electron-positron events by artificial neural networks as a demonstration of the active background rejection capabilities.

Because two dimensional tracking did not provide results as satisfying as expected, the possibility of three dimensional tracking was investigated. As a major result, it was demonstrated experimentally that full three dimensional tracking is possible in a cadmium-telluride sensor layer with particular modifications to the Timepix-ASIC. This is presented in the second paper. In the last section of the chapter the results are compared to other proposed and operating neutrinoless double beta experiment.

III.1 Publications

III.1.1 Publication: Characterization of the Energy Resolution and the Tracking Capabilities of a Hybrid Pixel Detector with CdTe-Sensor Layer for a Possible Use in a Neutrinoless Double Beta Decay Experiment

The publication “Characterization of the Energy Resolution and the Tracking Capabilities of a Hybrid Pixel Detector with CdTe-Sensor Layer for a Possible Use in a Neutrinoless Double Beta Decay Experiment” (Eur. Phys. J. C **73** (2013), 2374) covers the following issues:

- Pixel-by-pixel calibration of a CdTe-Timepix detector.
- Measurement of the energy resolution for a 1 mm thick CdTe-Timepix detector under different working parameters.

- Simulations on the detection of neutrinoless double decay with CdTe-Timepix detectors.
- Successful experimental demonstration of electron background identification by artificial neural networks.

The author's contributions to this paper were partly achieved within the scope of the author's master thesis. However, the publication was written and submitted during the time of the PhD thesis. Since the results presented in this publication are important for the rest of the thesis, they are included here.

My own contributions to the publication:

- Programming of an algorithm for automatic pixel-by-pixel calibration.
- Detector calibration.
- Optimization of the detector's working parameters concerning the energy resolution.
- Contributions to simulations (detector response to X-ray fluorescence photons).
- Experimental design, preparation and data acquisition.
- Contributions to data analysis (evaluation of the energy resolution, clustering, α-particle and muon recognition).
- Manuscript writing (corresponding author).

Contributions of the co-authors to the publication:

- Experimental idea.
- Contributions to simulations.
- Preparation and training of artificial neural networks for the data evaluation.
- Contributions to data analysis.
- Contributions to manuscript writing.

Eur. Phys. J. C (2013) 73:2374
DOI 10.1140/epjc/s10052-013-2374-1

THE EUROPEAN PHYSICAL JOURNAL C

Special Article - Tools for Experiment and Theory

Characterization of the energy resolution and the tracking capabilities of a hybrid pixel detector with CdTe-sensor layer for a possible use in a neutrinoless double beta decay experiment

Mykhaylo Filipenko[a], **Thomas Gleixner**[b], **Gisela Anton, Jürgen Durst, Thilo Michel**

University of Erlangen-Nuremberg, Erlangen Centre for Astroparticle Physics, Erwin-Rommel-Straße 1, 91058 Erlangen, Germany

Received: 27 November 2012 / Revised: 5 March 2013 / Published online: 3 April 2013
© The Author(s) 2013. This article is published with open access at Springerlink.com

Abstract Many different experiments are being developed to explore the existence of the neutrinoless double beta decay ($0\nu\beta\beta$) since it would imply fundamental consequences for particle physics. In this work we present results on the evaluation of Timepix detectors with cadmium-telluride sensor material to search for $0\nu\beta\beta$ in ^{116}Cd. This work was carried out with the COBRA collaboration and the Medipix collaboration. Due to the relatively small pixel dimension of $110 \times 110 \times 1000$ µm^3 the energy deposited by particles typically extends over several detector pixels leading to a track in the pixel matrix. We investigated the separation power regarding different event-types like α-particles, atmospheric muons, single electrons and electron-positron pairs produced at a single vertex. We achieved excellent classification power for α-particles and muons. In addition, we achieved good separation power between single electron and electron-positron pair production events. These separation abilities indicate a very good background reduction for the $0\nu\beta\beta$ search. Further, in order to distinguish between $2\nu\beta\beta$ and $0\nu\beta\beta$, the energy resolution is of particular importance. We carried out simulations which demonstrate that an energy resolution of 0.43 % is achievable at the Q-value for $0\nu\beta\beta$ of ^{116}Cd at 2.814 MeV. We measured an energy resolution of 1.6 % at a nominal energy of 1589 keV for electron-positron tracks which is about two times worse that predicted by our simulations. This deviation is probably due to the problem of detector calibration at energies above 122 keV which is discussed in this paper as well.

[a] e-mail: mykhaylo.filipenko@physik.uni-erlangen.de
[b] e-mail: thomas.gleixner@physik.uni-erlangen.de

1 Introduction

1.1 Neutrinoless double beta decay

The neutrinoless double beta decay is a hypothetical weak decay process in which two neutrons of a nucleus decay to two protons and two electrons:

$$2n \rightarrow 2p + 2e^- \tag{1}$$

This decay is forbidden in the standard model of particle physics since the lepton number is not conserved. Additionally, this process can occur only if neutrinos are massive Majorana-particles and consequently, the neutrino has to be its own antiparticle [1].

The half-life for nuclides which can undergo this process, like ^{76}Ge, ^{136}Xe or ^{48}Ca for example, can be calculated by the formula [2]

$$T_{0\nu}^{-1} = G_{0\nu}(Q_{\beta\beta}, Z)|M_{0\nu}|^2\langle m_\nu\rangle^2 \tag{2}$$

where $G_{0\nu}$ is the phase space volume, which depends on the Q-value ($Q_{\beta\beta}$) of the decay and the charge number Z of the nuclide. $M_{0\nu}$ is the $0\nu\beta\beta$ transition matrix element and $\langle m_\nu\rangle$ the effective Majorana-neutrino mass. If, according to claims of a past experiment [3], an effective neutrino mass of $\langle m_\nu\rangle < 0.39$ eV is assumed, half-lifes of $T_{\nu 0} > 10^{25}$ a are expected. Therefore, an experimental observation of this process is highly challenging and could not be achieved until now; but since an observation of $0\nu\beta\beta$ would provide insight into new fundamental physics beyond the standard model [1], many experiments are running or being developed to achieve an experimental proof for $0\nu\beta\beta$.

In an experiment the $0\nu\beta\beta$ is identified by measuring the sum energy of the two electrons, which is equal to the full Q-value of the decay [4]. The main goal is to construct a detector with sufficient resolution and high mass. High mass is indispensable to achieve a good sensitivity on the effective

Fig. 1 The Timepix detector with a USB-Readout [9]

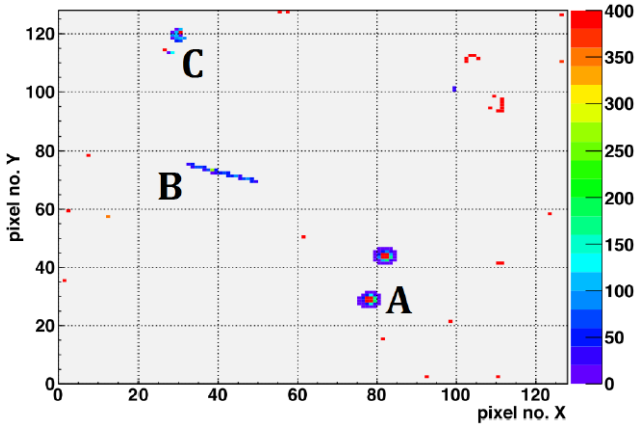

Fig. 2 Image of deposited energy in the pixels of the CdTe Timepix detector during an exposure time of 5 s. The color denotes the energy deposition in keV. One can deduce that two α-particles (A), a muon (B) and an electron (C) have interacted with the sensor

neutrino mass which is the lowest effective neutrino mass $\langle m_\nu \rangle$ that can be set as the limit with an experiment of mass M at an exposure time T if no signal event was measured. The sensitivity can be approximated by the formula [5]:

$$\langle m_\nu \rangle = K \left(\frac{b \Delta E}{MT} \right)^{\frac{1}{4}} \tag{3}$$

An excellent energy resolution ΔE is not only required to enhance the sensitivity but also to discriminate $0\nu\beta\beta$ against the neutrino accompanied double beta decay [4]. In order to avoid energy loss at insensitive detector boundaries, most experiments use a detector which contains the considered nuclide in the sensor material. K is an isotope depending constant. As the mass M and the exposure time T are limited by practical or cost issues and the energy resolution by the fano-limit, the only way to increase sensitivity further is to reduce the background rate b as good as possible. The background in the region of interest is mainly provided by α-particles, muons and electrons.

In this paper we investigated the concept of active background reduction by the tracking capabilities of Timepix detectors with CdTe sensors: The Timepix (Fig. 1) is a hybrid semiconductor pixelated imaging detector which is explained below. When a charged particle propagates through the sensor layer it induces electron-hole pairs proportional to the amount of energy which was deposited by the particle. By applying a bias voltage over the sensor layer, the electrons drift towards the electrodes where the induced charge is collected. If a particle is stopped within the sensor layer completely, its total kinetic energy is deposited. Therefore, if $0\nu\beta\beta$ takes place within the sensor layer, the total energy of the electrons can be measured. Indeed, there are several possible isotopes for this purpose in CdTe [7] but as ^{116}Cd has the highest Q-value of 2.814 MeV [8], which is larger than the highest γ-energy (2.614 MeV) from a natural decay chain, enriched cadmium should be used as the decaying isotope. The advantage of the pixelation (in contrast to CdZnTe Coplanar Grid detector) is that a topological pattern is produced for each event (Fig. 2). This information might be used for event identification and active background rejection. As preliminary measurements show, α-particles produce a round shaped pattern (Fig. 2 A) and muons produce straight lines (Fig. 2 B). Hence, they are very unlikely to be confused with the pattern of $0\nu\beta\beta$, which we estimated by simulations. A detailed discussion on the identification of this sort of background will be presented elsewhere. The most severe problem, which we want to focus on in this paper, is to distinguish between single electrons and $0\nu\beta\beta$ events (Fig. 3(a) and (b)). We used simulation data to study the particular properties of both event types. Afterwards we trained artificial neural networks (ANNs) and estimated their performance first on simulated and then on experimental data.

1.2 The timepix detector

Our Timepix detector comprises a 1 mm thick CdTe sensor with ohmic contacts bump-bonded to an ASIC of 65536 pixels. The Timepix ASIC has been developed by the Medipix collaboration [6] in cooperation with the EUDET project in IBM 0.25 µm CMOS technology. Each pixel has a size of 55 µm. The pixels are organized in a matrix of 256 rows and 256 columns thus giving an active area of 1.4×1.4 cm^2. In our detector only every second pixel is bump-bonded to the sensor layer wherefore the effective pixel size is 110 µm. The CdTe sensor is fully depleted with an electric potential difference of 500 V between the common electrode (facing the source) and the pixel electrodes. Electron-hole pairs are produced by ionizing particles in the sensitive pixel volume and drifted towards the pixel electrodes where they influence currents due to their drift motion. Each sensor pixel is connected by an indium-tin bond to the input electrode of an electronics cell in the ASIC. In each pixel cell the influenced current signal is converted to a triangular shaped voltage

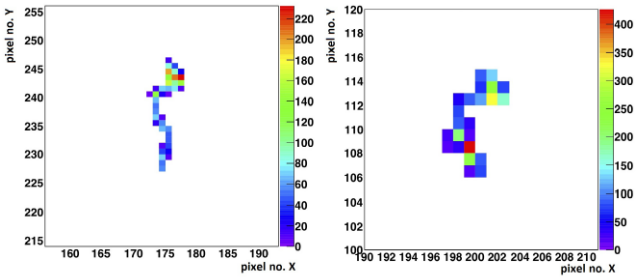

(a) an electron event (b) a $0\nu\beta\beta$ event

Fig. 3 Examples for pattern of a simulated electron (**a**) and a simulated $0\nu\beta\beta$ (**b**) event in ^{116}Cd. The color denotes the energy deposition in keV

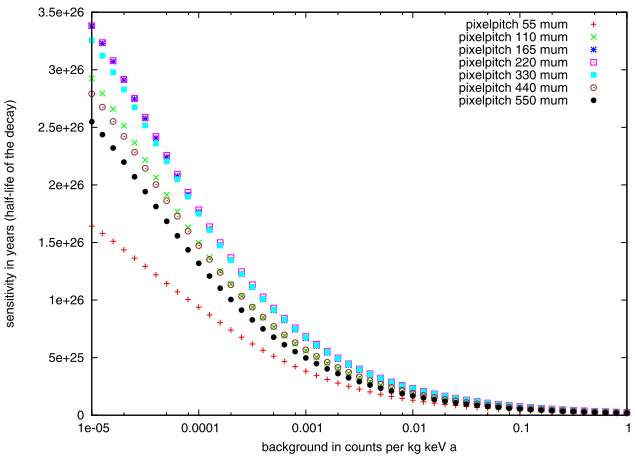

Fig. 4 Sensitivity versus background rate of a CdTe-Timepix detector with a 3 mm thick CdTe sensor. The best sensitivity can be achieved with a pixelsize of 165 µm

pulse by a charge sensitive amplifier of Krummenacher type. The shaping time is approximately 120 ns. The length of the falling edge of the amplifier is in the order of microseconds, depending on the energy deposited in the pixel. This voltage pulse is compared to a globally adjustable threshold in a leading-edge discriminator in each pixel. The minimum threshold that can be set with negligible amount of noise-triggered pixels is approximately 5.5 keV. The gain of the preamplifier, the falling edge of the preamplifier and the threshold can be set externally by a DAC. The DAC-values are referred as PreAmp, Ikrum and THL, respectively. After the amplifier the processing is purely digital and depends on the operation mode which is chosen. Each pixel can be configured in one of three modes of digital operation. We used only the spectroscopic mode which is called "time-over-threshold" (TOT). It is described in the calibration section.

2 Simulations

The simulations were performed with the in-house developed Monte-Carlo simulation ROSI, which is based on EGS4 and has a low energy extension with the interaction codes LSCAT [10]. Each event is simulated independently by propagating the corresponding particles (photons, electrons, holes) through the sensor and calculating the detector response (i.e. the energy measured in each pixel). The initial momentum of the particles is calculated with decay 0 [11].

We used the simulations to estimate the detector response to $0\nu\beta\beta$ events. A typical pattern for such an event is shown in Fig. 3(b). The two main aspects of the detector performance concerning $0\nu\beta\beta$ experiments are the energy resolution, which is required to distinguish between the regular double beta decay ($2\nu\beta\beta$) and $0\nu\beta\beta$, and the spatial resolution which determines the tracking quality. Both properties depend on detector parameters like the pixel size, the thickness of the sensor layer or the bias voltage. The energy resolution can improve with increasing pixelsize and increasing bias voltage since effects like charge sharing (leakage of the charge to neighbor pixel by repulsion and diffusion) [12] have smaller contribution. In contrast, a large pixel size provides less tracking information and therefore a compromise is needed. In Fig. 4 the simulated sensitivity at given background rate for a 3 mm thick sensor is shown which suggests that the best sensitivity can be achieve with pixels of either 165 µm or 220 µm size. However, a smaller pixel size is apparently preferable for tracking. As this paper focuses on the performance of the Timepix performance with experimental data, the details of this evaluation will be discussed in a future paper. Although it turned out that a reasonable tradeoff between the two effects is achieved at a pixelsize of 165 µm, we used a detector with 110 µm pixel size detector for the experiments because only those were available to us.

A simulated sum energy spectrum—i.e. the energy deposited by the two electrons from the ^{116}Cd decay—around the Q-value is shown in Fig. 5 for a Timepix with 165 µm pixelsize and a thickness of 3 mm. The simulation yields a resulting energy resolution of 0.43 % ($\frac{\sigma}{E}$) at the Q-value of 2.814 MeV which allows a reasonable separation of $0\nu\beta\beta$ events from the $2\nu\beta\beta$ spectrum. The $0\nu\beta\beta$ would be observed at lower energies compared to the full Q-value due to various mechanisms of charge loss within the detector. For the simulations we assumed a half-life of 2.75×10^{25} years, a detector mass of 400 kg with 90 % enriched ^{116}Cd observed over 3 years and well-calibrated detectors. In fact, the calibration of the Timepix is non-trivial and will be discussed in Sect. 3. Especially, a calibration up to energy depositions of several hundred keV per pixel is required since such depositions often have non-negligible contributions to the total energy of the event: In Fig. 6 the contribution of the deposited energy per pixel $P(E_{dep})$ to the total detected event energy is plotted against the energy deposition per pixel E_{dep}. $P(E_{dep})$ is defined as

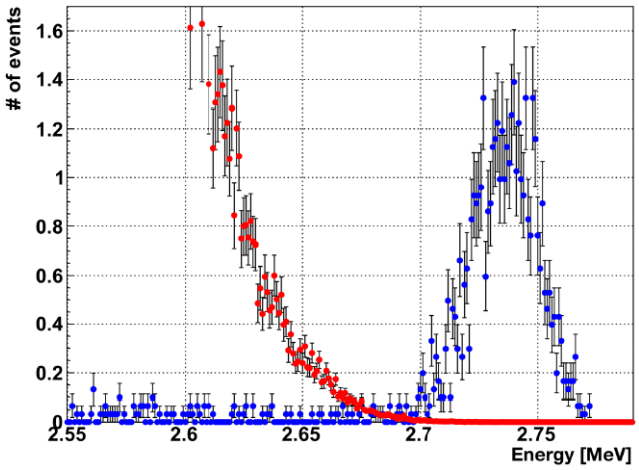

Fig. 5 The simulated spectrum of $2\nu\beta\beta$ (*red*) and $0\nu\beta\beta$ (*blue*) events around the Q-value. The bin size is 1 keV. The assumptions of the simulation are given in the text

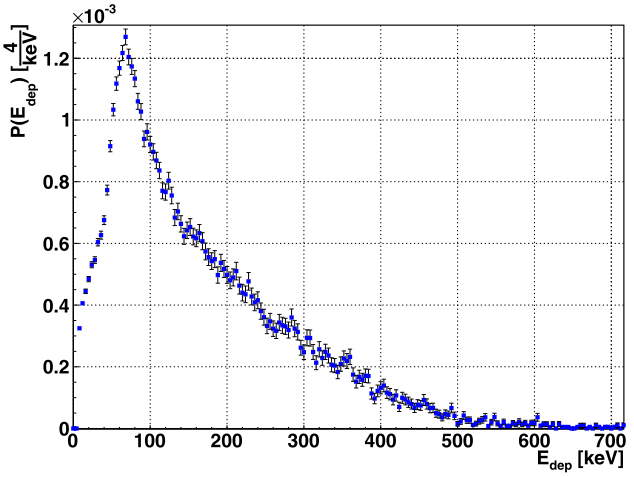

Fig. 6 The contribution of a particular energy deposition per pixel to the full energy of an event. The *error bars* are Poissonian

$$P(E_{dep}) = \frac{1}{N_{events}} \cdot \left(\frac{E_{dep}}{Q} \cdot N_{pix}(E_{dep}) \right), \tag{4}$$

where N_{events} is the number of simulated events and $N_{pix}(E_{dep})$ is the number of pixels (summed over all events) which had an energy deposition of E_{dep}. The bin size in the histogram is 4 keV. We see that even depositions up to 600 keV are relevant.

As stated in the introduction single electrons produce pattern which may be very similar to the pattern of $0\nu\beta\beta$ and therefore a unique event identification can hardly be performed. Nevertheless this problem can be addressed by several pattern identification techniques. We used Artificial Neural Networks (ANNs) which were implemented with the open source library FANN [13]. The networks had a feed forward structure with the following parameters:

- 10 input units
- 1 output unit
- 5 hidden layers
- between 20 and 200 neurons per layer
- $\tanh(0.3x)$ as activation function
- Resilient Propagation as learning algorithm.

We used the following properties of the track pattern as features for the ANN input:

1. The number of pixel with $E > E_{th}$, where E_{th} is the energy threshold for each pixel.
2. The distance between the energy weighted and the energy unweighted centroids of the coordinates of the triggered pixels.
3. The energy of a two pixel structure that can mark the begin of a single electron track.
4. The energy of a three pixel structure that can mark the begin of a single electron track.
5. The length of a structure that can mark the begin of a single electron track.
6. The maximum distance of pixels above 250 keV.
7. The number of pixels with an energy sum below 185 keV with their neighbor pixels.
8. The number of straight lines above a certain length in a track.
9. The number of pixels with only two triggered pixel touching the pixel from the side, which form a straight line together.
10. The number of pixels with only two triggered pixel touching the pixel from the side, which form a triangle together.

The networks are trained on the same number of simulated single electron and $0\nu\beta\beta$ events. Each event is assigned a ranking R between 0 and 100 (which is not a physical quantity) and a particular cut value c ($c \in [0; 100]$) is chosen. If the rating of an event R is smaller than the cut parameter c, it is classified as a single electron event and vice versa. The identification performance of the networks on independent simulated data sets[1] is shown on Fig. 7. On the x-axis the value of the cut parameter is plotted and on the y-axis the part of events which have a rating $R < c$. That means, if we fix a particular value for c, for instance 70, we can reject about 90 % of the single electron background but will lose 40 % of the $0\nu\beta\beta$ events (because of classification errors). In order to test the performance of this method on real data, we carried out the experiment which is presented in Sect. 4.

[1] Independent in this context means, that the data which was used for the performance analysis was not used for the network training beforehand.

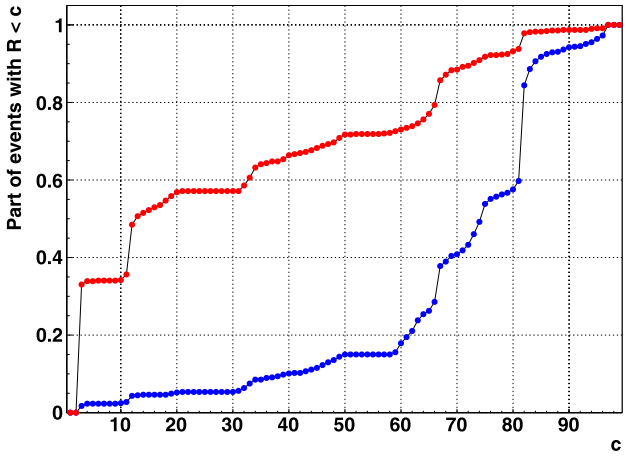

Fig. 7 Performance of artificial neural networks on simulated data from single electron (*red*) and $0\nu\beta\beta$ (*blue*) events

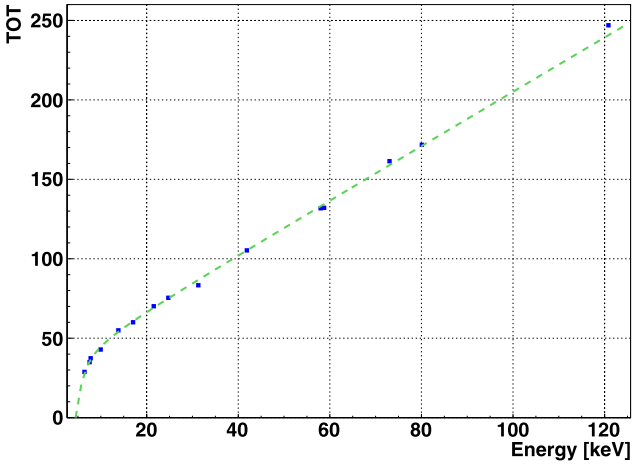

Fig. 8 Interdependency between TOT and energy; data points are from illumination with monoenergetic X-rays sources. The *dotted curve* is a fit assuming $TOT(E) = a \cdot E + b + \frac{c}{E-t}$ with parameters a, b, c and t common for all pixels (global calibration)

3 Calibration and energy resolution

The Timepix detector enables the measurement of the energy deposited in each pixel by running in the so called "time-over-threshold" (TOT) mode. Energy deposition in a pixel leads to the generation of electron-hole pairs. An electric field, which is applied over the sensor layer, drifts these charges towards the pixel electrodes. While the charges are drifted, they induce a signal in the pixel electrodes that is integrated and converted to a voltage signal in the preamplifier. A particular threshold level (THL) is chosen. When the signal rises above this threshold, the counting of clock pulses is started and continued until the signal falls below the threshold again. The number of counts—called time over threshold (TOT)—depends non-linearly on the energy and an interdependency between both has to be determined. To perform this task we used the method described in [14]: The peaks in the TOT spectra[2] of known photon radiation sources are fitted with Gaussian distributions and the mean of the distribution is taken for a TOT versus energy calibration. From measurements with different X-ray sources the diagram in Fig. 8 was obtained. The real energy depositions by the X-ray photons have to be estimated by a simulation since they are slightly shifted to lower energies (compared to the energies of the absorbed photons) due to trapping, charge sharing and other effects of charge loss [12]. The TOT(E) interdependency is approximated by [14]:

$$TOT(E) = a \cdot E + b + \frac{c}{E - t} \tag{5}$$

The calibration can be performed with one parametrization for all pixels (global calibration) or for every pixel individually (pixel-by-pixel calibration). For the global calibration we used all points as shown in Fig. 8; for the pixel-by-pixel calibration we used the L- and K-line complexes[3] of gadolinium (6.43 keV, 41.88 keV), the K-line complex of molybdenum (17.03 keV), the 59.54 keV-line of ^{241}Am and the 122.06 keV-line of ^{57}Co. We calibrated and used a Timepix with a 1 mm thick CdTe sensor layer, ohmic contacts and a pixel size of 110 µm (128 × 128 pixel) which was delivered by X-ray Imaging Europe GmbH XIE[4] [15]. The bias voltage was 500 V, the clock frequency 80 MHz and the most important DAC settings: Ikrum 10 (return to zero time of the preamplifier), THL 190 (threshold level), which corresponds to an energy threshold of about 5.4 keV, and PreAmp 210 (preamplifier gain). For the data acquisition a USB-Readout 2.0 [9] and the Pixelman software package v2.0.3 were used [16].

After reconstructing the energy spectra (see Fig. 9 for example) for single pixel hits[5] we investigated the energy resolution ($\frac{\sigma}{E}$ of the fitted Gaussians) of the detector for various peaks. The results are shown in Fig. 10. The blue points are the energy resolution if a global calibration is used for energy reconstruction, the red points if a pixel-by-pixel calibration is used and the brown points are the results of simulations which take into account only the physics within the sensor layer but no other effects of broadening in the readout electronics. Hence, the brown points correspond to the

[2]The spectra that we used were single clustering spectra. That means, that only the data of pixels is used which had no triggered neighbor pixels during the same frame.

[3]The L- and K-line complexes are an overlay of the α- and β-lines since these cannot be resolved individually.

[4]www.xi-europe.de, Freiburger Materialforschungszentrum, Stefan-Meier-Straße 21, D-79104 Freiburg i. Br.

[5]Single pixel hits means that the energy of the incident photon is deposited in one pixel in such a way that no neighboring pixel is triggered.

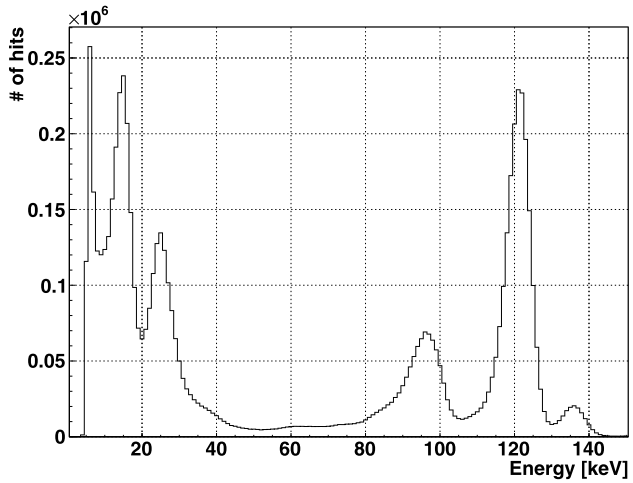

Fig. 9 The energy deposition spectrum of photons from a ^{57}Co source, reconstructed with a pixel-by-pixel calibration

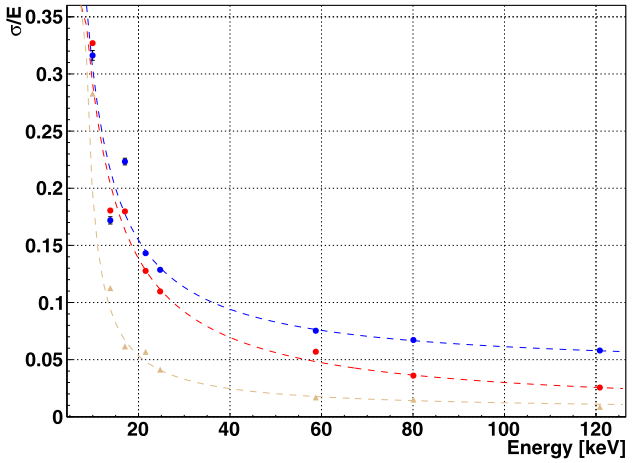

Fig. 10 The energy resolution for K- and L-Shell X-rays and radioactive γ-lines with a global calibration (*blue*); with a pixel-by-pixel calibration (*red*) and for ROSI simulation data (*brown*) with IKrum 10 and THL 190. For further explanations see text

physical possible limits set by the detection material which theoretically could be achieved. We fitted a function of the form

$$\frac{\sigma}{E}(E) = \alpha + \frac{\beta}{E - \gamma} \tag{6}$$

to the data in Fig. 10 to estimate the energy resolution for single pixel hits at high energy depositions per pixel. The energy resolution limit α was determined to be $\alpha = 4.10$ % for the global calibration, $\alpha = 1.01$ % for the pixel-by-pixel calibration and $\alpha = 0.54$ % for the ideal detector. We compared the performance of the detector to the simulations which included the noise of readout electronics. The deviations between simulation and theory are shown in Fig. 11.[6] We obtain a good agreement between experiment and simulation.

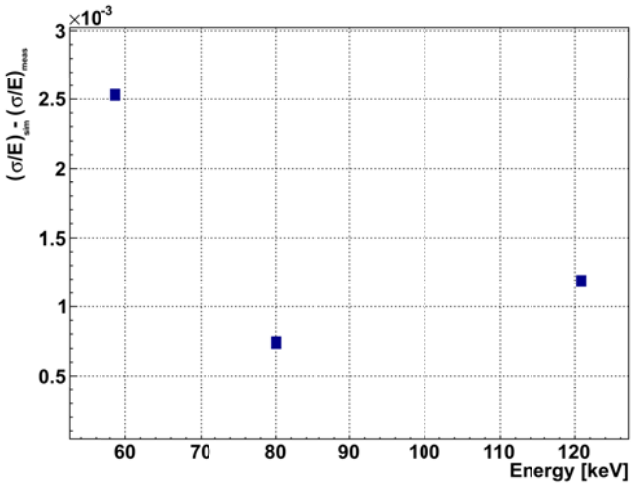

Fig. 11 Difference of measured relative energy resolution and simulated relative energy resolution versus photon energy. Statistical errors are small and not visible

Since the shape of the voltage signal used in the integrator to calculate the TOT depends on the working parameters of the detector (Ikrum, THL and the bias voltage), we investigated the influence of different parameter sets for Ikrum and THL on the energy resolution. We could achieve an improvement in the energy resolution as presented in Table 1 by going from the usual settings that we used (Ikrum 10, THL 190) to the lowest possible Ikrum (04) and a THL of 210. The dependence on the bias voltage is presented in Fig. 12. The blue points are the energy resolution for the 59.54 keV peak of ^{241}Am and the red points for the 122.06 keV peak of ^{57}Co. As expected, the energy resolution improves with higher bias voltage because the effect of charge sharing [12] is reduced with higher bias voltage. The highest voltage that we could use without exceeding a critical value of the leakage current (40 µA) was about 800 V. Nevertheless going up with the bias voltage leads to an additional negative effect: The number of useless pixels (pixels which are permanently counting) increases rapidly (Fig. 13). The dependence of the number of useless pixels on the bias voltage can roughly be approximated by a power-law (red curve). We didn't investigate this problem in more detail but a reasonable explanation could be the following: It is well-known that the leakage current rises with the voltage. However, the leakage current in every pixel is slightly different due to sensor and ASIC fabrication. Some pixels have always a higher leakage current because of inhomogeneities in the CdTe-crystal and the leakage-current compensation.

[6]For this plot as for some other in this paper the error bars are small and invisible because for every point the statistics is very high which is the number of pixels on the matrix (16384).

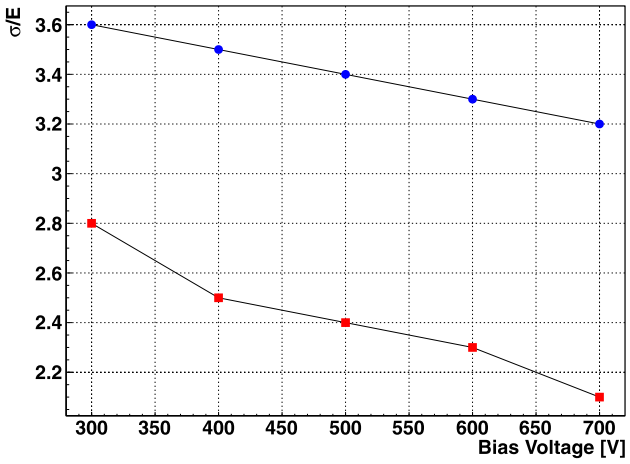

Fig. 12 Energy resolution versus bias voltage for ^{241}Am (at 59.54 keV) (*blue*) and ^{57}Co (at 122.06 keV) (*red*) with a pixel-by-pixel calibration for IKrum 04 and THL 210. Statistical errors are very small and thus not visible

Table 1 The measured relative energy resolution for ^{241}Am, ^{133}Ba and ^{57}Co (122.06 keV) given in % for two different DAC settings; the bias voltage was 500 V

DACs	^{241}Am	^{133}Ba	^{57}Co
IKrum 10, THL 190	5.6	3.5	2.5
IKrum 04, THL 210	3.4	3.2	2.3

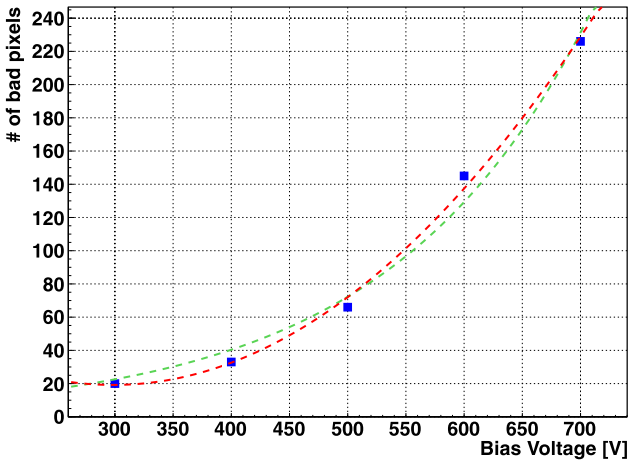

Fig. 13 Number of useless pixels on the detector matrix as function of the bias voltage. A power law (*red*) of the form $N(V) = a \cdot (V-b)^2 + c$ and an exponential function (*green*) of the form $N(V) = a \cdot \exp(-b \cdot V)$ are shown as possible fit functions. The detector contains 16384 pixels in total

Once, the noise produced by the leakage current rises above the threshold level in these particular pixels, the pixels are permanently counting.

The highest photon energy that could be used for a pixel-by-pixel calibration on a practical timescale was 122.06 keV.

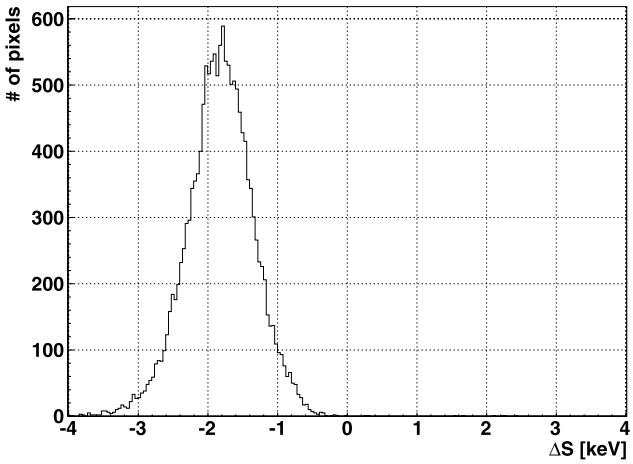

Fig. 14 The distribution of ΔS at the ^{241}Am peak (59.54 keV) for all pixels. It is (almost) a Gaussian distribution around -1.88 keV with a width of $\sigma = 0.43$ keV

For higher energies the efficiency for single pixel hits is far too small. This has two reasons: Firstly, the absorption efficiency for a thick 1 mm CdTe sensor is smaller than 10 %. Secondly, with higher photon energies the travel distance of the photoelectron within the CdTe increases and is usually larger than the pixelsize of 110 µm. This means, that single pixel hits, which are needed for calibration, become more and more unlikely with increasing energy. We measured one week to achieve 300 counts over the whole matrix at the 356.02 keV peak of ^{133}Ba. Assuming that we can take data 50 times faster with a new read-out and that at least 200–400 counts are required in one pixel for a reliable calibration, a total measurement time of about $\frac{16384}{50 \cdot 52} \approx 6.3$ years is needed. Therefore, a calibration cannot be done this way on practical timescales.

However, as electrons can often deposit energies in the MeV range in one pixel, it is important to estimate the quality of the calibration beyond the highest pixel-by-pixel calibration point. Beyond an energy of 122.06 keV we used four peaks with energies at 136.47 keV (^{57}Co), 184.35 keV (^{137}Cs Compton backscattering), 238.63 keV and 356.02 keV (^{133}Ba). For this purpose we define the quantity $\Delta S(E)$ which is the difference between the expected peak position and the reconstructed peak position with a pixel-by-pixel calibration at a peak energy E:

$$\Delta S(E) = \text{Expected peak position at energy } E - \text{Reconstructed peak position at energy } E \quad (7)$$

The distribution of ΔS (59.54 keV) among all pixels of the matrix is shown in Fig. 14. For other energies the distribution has a similar shape. For an ideal calibration we would expect a very sharp peak centered around 0 keV. The averaged value of ΔS over all pixels for the energies given in the previous paragraph is shown in Fig. 15. We can see that $\overline{\Delta S}$

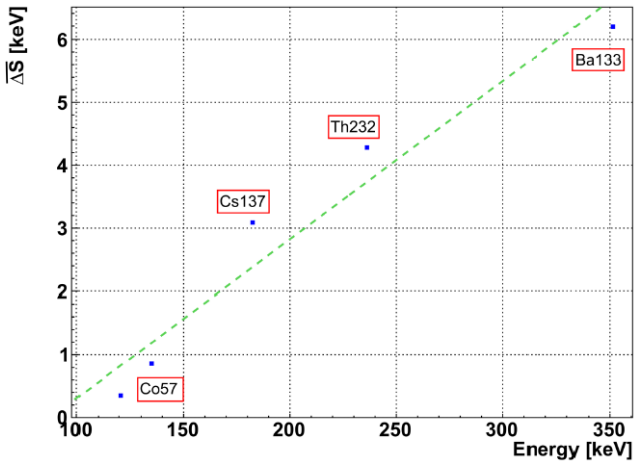

Fig. 15 Data points: averaged ΔS for peak energies above the pixel-by-pixel calibration range; the *green line* is a linear fit to the data. Statistical errors are very small and thus not visible

increases with energy (Fig. 15). We performed an additional calibration step to cope with this effect. It turned out that using a linear fit (green line) for the given data points and to subtract the value of the linear function from the regular TOT calibration curve leads to a significant improvement at energies beyond 120 keV. The positive effect on the peak position and the energy resolution are discussed in the next section.

4 Tracking of electrons

In order to investigate the performance of neural networks on experimental data, we performed the following experiment with a ^{232}Th source: About 35 % of the photon flux radiated by natural ^{232}Th are 2.614 MeV photons from ^{208}Tl which is the last nuclide in the natural decay chain of ^{232}Th. In the CdTe sensor such photons can be Compton-scattered, which produces single electrons, or generate electron-positron pairs with a total kinetic energy of 1.588 MeV. Apparently, electron-positron pairs starting at one point produce a similar pattern to the two electrons in $0\nu\beta\beta$ and hence electron-positron tracks can be used as a substitute to verify experimentally the pattern recognition power of the Timepix in a $0\nu\beta\beta$ experiment.

In the actual experimental setup (Fig. 16) we used a ^{232}Th source (1) with an activity of 14.8 MBq which was placed 40 cm away from the detector (2). The geometry was chosen in such a way that the photon momentum is approximately parallel to the sensor layer and every 0.3 s one or two pair production events are expected to occur. The detector was fixed onto a lead block and surrounded by a light shield box (3) to shield the detector from optical photons and by lead (4) for additional gamma shielding. We recorded and evaluated 34.4 hours of data. This gives us 3646025 events comprising 606813 electron events (both single and pair production) after the rejection of α-particle and muon events.

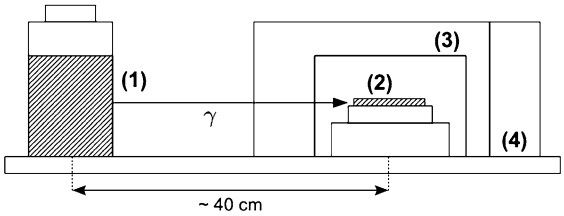

Fig. 16 A scheme of the experimental setup for the ^{232}Th measurement. (*1*) The ^{232}Th source, (*2*) the sensor layer, (*3*) the cardboard and (*4*) the lead wall. The distance between the source and the detector was about 40 cm

Such events are clusters on the pixel matrix as shown in Fig. 2 and Fig. 3. A cluster is a set of triggered pixels which are direct neighbors with each other. The energy deposited in a particular cluster is calculated as the sum over the energy depositions in all individual pixels belonging to the particular cluster. As electrons in the MeV energy range always trigger more than one pixel, all energy spectra in this section are spectra of such clusters, which means that every entry in the spectrum is due to a cluster and not to the energy deposition in a single pixel. We divided the data into two packages. We used the first to check our data analysis and the energy resolution. On the second package we tested the artificial neural networks.

4.1 Energy resolution of electron-positron pairs at 1.6 MeV

The energy spectrum of events in the region of interest (Fig. 17) consists of Compton background and the pair production peak at about 1.6 MeV. At this energy most of the event clusters consist of about 14–17 pixels in average. The energy resolution ($\frac{\sigma}{E}$) at the peak is 2.2 % (red) and the reconstructed peak energy is 1614.1 MeV if the regular calibration curve is used (Eq. (5)). If we apply the additional calibration step explained in the previous section, the reconstructed peak position is 1589.1 MeV (blue) and the energy resolution improves to 1.6 % which is twice the value that we would expect from simulation.

We estimate that the reduced resolution is due to the weak energy calibration at high energies. The calibration data cover energies up to 130 keV with high statistics and energies up to 350 keV with low statistics. From the results presented in Fig. 15 we see that the extrapolation is not optimal. On the other hand we know from simulation that electron tracks can lead to energy deposition in a pixel of about 400 keV. Hence, a new method is needed to calibrate the detector up to these energies. One possibility to do so is to illuminate the detector with a tightly focused laser beam which is triggered to shot pulses with a precisely known amount of photons into one pixel during one frame. For this paper we

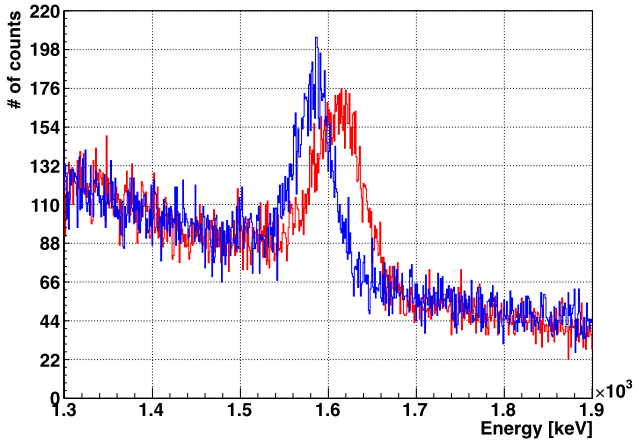

Fig. 17 Measured energy spectrum of pair production and Compton scattering events before (*red*) and after (*blue*) applying the additional high energy calibration

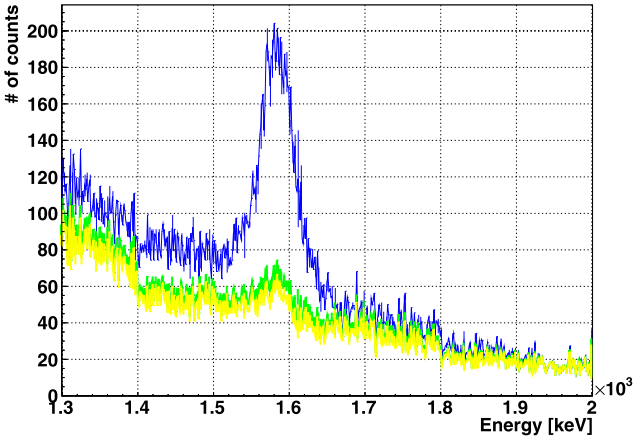

Fig. 18 Reconstructed electron spectrum in the region of interest; all events (*blue*), upper and lower limits (*green/yellow*) for events reconstructed as single electrons

take the energy resolution as it is since it is sufficient for the track investigations which are the main issue in this paper.

4.2 Separation power of neural networks on electron-positron pairs and single electrons

As next we applied artificial neural networks to the data. We divided the region of interest from 1200 keV to 2000 keV into eight equal intervals of 200 keV width. For every interval an individual network i was trained and an optimal cut parameter c_i chosen. Every event of the spectrum was classified by the appropriate network i and assigned a rating R. If the rating of an event R is smaller than the cut parameter c_i, it is classified as a single electron event and vice versa.

The rating R is not a real physical quantity and does not describe some kind of probability. To perform the reconstruction correctly, the network performance for the chosen cut parameters c_i has to be taken into account. In fact, if a particular value c_i is chosen, the network classifies a particular percentage of the single electron events (π_1) and a particular percentage of the two electron events (π_2) correctly. These values are determined in the network training process. If we call the true number of single electron events in a particular energy bin η_1 and the true number of two electron events η_2, then the number of events classified as two electron events κ_2 can be calculated as

$$\begin{aligned}\kappa_2 &= \pi_2 \cdot \eta_2 + (1-\pi_1)\cdot\eta_1 \\ &= \pi_2 \cdot \eta_2 + (1-\pi_1)\cdot(N-\eta_2)\end{aligned} \tag{8}$$

N is the total number of events in a particular energy bin ($\eta_1 + \eta_2 = \mathrm{N}$). Actually, κ_2 is the quantity that we obtain from the data by assigning a rating R to every event.[7] Now the real number of single and two electron events can be calculated by inverting formula (9):

$$\eta_2 = \frac{1}{\pi_1 + \pi_2 - 1}\big(\kappa_2 - (1-\pi_1)\cdot N\big) \tag{9}$$

In the reconstructed spectrum (Fig. 18) the area below the green/yellow lines belongs to the spectrum of Compton scattered photons and the area above the green/yellow lines (and below the blue line) to the pair-production events. The remaining events in the pair production spectrum below the peak energy are pair production events in which at least one of the particles escaped the sensor layer and therefore not the full energy was deposited in the sensor. The green line is the upper limit for the uncertainties in the event classification whereas the yellow line is the lower limit.

5 Conclusions

We investigated the applicability of the semiconductor pixel detector Timepix with a CdTe sensor for future use in the search for the $0\nu\beta\beta$. A pixel-by-pixel energy calibration was performed in the range between 5 keV and 120 keV with high precision. For energies in the range 130 keV to 350 keV the calibration was performed with lower precision but still a resolution of 1.6 % could be achieved at the pair production peak of ^{208}Tl at 1588.8 MeV. Nonetheless the results of the simulations indicate that the energy resolution can be improved by a factor of two.

We investigated the tracking capabilities of the Timepix detector in order to separate different types of events. The separation of muons and α-particles from electrons is very pure. Further, a good separation of single electron tracks from electron-positron tracks could be reached by artificial neural networks. Thus, the tracking ability makes the

[7] As the ANNs are sensitive on statistical fluctuations, we used the average value of the 5 neighbor bins (to the left and right) to smooth the spectrum for the ANNs.

Timepix detector an interesting candidate for future $0\nu\beta\beta$ experiments.

One drawback may be the relatively large surface to volume ratio which almost forbids the choice of a fiducial volume with a certain distance from the surface. But it may turn out that due to the track ability fiducializing is not necessary. A second draw back is the enormous number of detectors that would be needed to achieve a reasonable detector mass. As long as other experimental approaches have not proven to be able to detect unambiguously the $0\nu\beta\beta$ decay, the method proposed in this work might be kept as a possible solution.

Acknowledgements We would like to thank Steffen Taut, Daniel Gehre and Kai Zuber from the Technical University of Dresden for their support and giving us the opportunity to perform the experiments with ^{232}Th in the laboratory for radiochemistry.

This work was carried out within the Medipix collaboration and the COBRA collaboration. The authors thank both collaborations for their support.

Open Access This article is distributed under the terms of the Creative Commons Attribution License which permits any use, distribution, and reproduction in any medium, provided the original author(s) and the source are credited.

References

1. J. Schechter, J.W.F. Valle, Phys. Rev. D **25**, 2951 (1982)
2. F. Simkovic, M.I. Krivoruchenko, A. Faessler, Prog. Part. Nucl. Phys. **66**, 451–466 (2011)
3. H.V. Klapdor-Kleingrothaus, Nucl. Phys. B, Proc. Suppl. **145**, 219–224 (2009)
4. S.R. Elliott, P. Vogl, Double beta decay. Annu. Rev. Nucl. Part. Sci. **52**, 115–151 (2002)
5. J.J. Gomez-Cadenas et al., Sense and sensitivity of double beta decay experiments. J. Cosmol. Astropart. Phys. **2011**, 06 (2011)
6. X. Llopart, R. Ballabriga, M. Campbell, L. Tlustos, W. Wong, Nucl. Instr. Methods A **581**, 485–494 (2007)
7. K. Zuber, Phys. Let. B **519**, 1–7 (2001)
8. S. Rahaman et al., Phys. Lett. B **703**, 412–416 (2011)
9. M. Platkevic, J. Jakubek, Z. Vykydal et al., Nucl. Instr. and Meth. A **591**, 245–247 (2008)
10. J. Giersch, A. Weidemann, G. Anton, Nucl. Instr. Methods A **509**, 151–156 (2003)
11. O.A. Ponkratenko, V.I. Tretyak, Yu.G. Zdesenko, Phys. At. Nucl. **63**, 1282 (2000)
12. J. Jakubek, Nucl. Instr. Methods A **607**, 192–195 (2008)
13. S. Nissen, Implementation of a Fast Artificial Neural Network Library (fann). Department of Computer Science (2003), University of Copenhagen (DIKU)
14. J. Jakubek et al., Nucl. Instr. Methods A **591**, 155–158 (2008)
15. D. Greiffenberg, A. Fauler, A. Zwerger et al., J. Instrum. **6**, C01058 (2011)
16. D. Turecek, J. Jakubek, Z. Vykydal et al., J. Instrum. **6**, C01046 (2011)

III.1.2 Publication: 3D Particle Track Reconstruction in a Single Layer Cadmium-Telluride Hybrid Active Pixel Detector

The publication "3D Particle Track Reconstruction in a Single Layer Cadmium-Telluride Hybrid Active Pixel Detector" (Eur. Phys. J. C **74** (2014), 3013) covers the following issues:

- Presentation of a new reconstruction algorithm for three dimensional trajectories of ionizing particles with a pixelated semiconductor detector.
- Application of a modified algorithm to experimental data acquired with α-particles.
- Successful reconstruction of measured minimal ionizing electron tracks through the cadmium-telluride sensor layer of a Timepix-detector.

My own contributions to the publication:

- Experimental idea.
- Preparatory measurements.
- Experiment preparation and data acquisition at the DESY testbeam.
- Contributions to data analysis together with the co-authors.
- Manuscript writing (corresponding author).

Contribution of the co-authors to the publication (in particular Thomas Gleixner):

- Development of the reconstruction algorithm.
- Simulations.
- Data analysis.
- Contributions to manuscript writing.

Eur. Phys. J. C (2014) 74:3013
DOI 10.1140/epjc/s10052-014-3013-1

THE EUROPEAN PHYSICAL JOURNAL C

Regular Article - Experimental Physics

3D particle track reconstruction in a single layer cadmium-telluride hybrid active pixel detector

Mykhaylo Filipenko[a], **Thomas Gleixner**[b], **Gisela Anton, Thilo Michel**

University of Erlangen-Nuremberg, Erlangen Centre for Astroparticle Physics, Erwin-Rommel-Straße 1, 91058 Erlangen, Germany

Received: 25 March 2014 / Accepted: 30 July 2014
© The Author(s) 2014. This article is published with open access at Springerlink.com

Abstract In the past decades the search for neutrinoless double beta decay has driven many developments in all kind of detector technology. A new branch in this field are highly-pixelated semiconductor detectors—such as the CdTe-Timepix detectors. It comprises a cadmium-telluride sensor of 14 mm × 14 mm × 1 mm size with an ASIC which has 256 × 256 pixel of 55 µm pixel pitch and can be used to obtain either spectroscopic or timing information in every pixel. In regular operation it can provide a two dimensional projection of particle trajectories; however, three dimensional trajectories are desirable for neutrinoless double beta decay search and other applications. In this paper we present a method to obtain such trajectories. The method was developed and tested with simulations that assume some minor modifications to the Timepix ASIC. Also, we were able to test the method experimentally and in the best case achieved a position resolution of about 63 µm for electrons with an energy of 4.4 GeV.

1 Introduction

The main motivation behind the methods and experiments presented in this publication is to demonstrate the possibility of three dimensional (3D) particle trajectory reconstruction within the sensor of a hybrid active pixel detector for a neutrinoless double beta experiment. 3D tracking could help to achieve high sensitivities due to background rejection by particle identification. The neutrinoless double beta decay is a hypothetical, lepton-number violating decay where two neutrons in a nucleus are transformed into two protons and two electrons without anti-neutrino emission, e.g.[1]

$$^{116}\mathrm{Cd} \rightarrow {}^{116}\mathrm{Sn} + 2e^{-}. \quad (1)$$

This lepton-number violating decay is forbidden in the standard model of particle physics. Its observation would prove that neutrinos are Majorana fermions via the Schechter–Valle theorem [1]. This would require modifications in the standard model. The standard model distinguishes between neutrinos and anti-neutrinos and treats them as massless particles. The observation of neutrino oscillations already revealed that neutrinos have non-zero rest mass. If neutrinos were Majorana fermions, the small but non-zero neutrino mass (compared to the masses of the charged leptons) might be explainable with the help of sea-saw mechanisms. Therefore, besides the direct evidence for lepton-number violation, the observation of neutrinoless double beta decay would have an immense impact on our understanding of particle physics [2].

Although the search for the neutrinoless double beta decay is the main reason for our investigations, semiconductor voxel detectors could have other interesting applications as well. When using a thin sensor coupled to a pixelated ASIC, the read-out volume of single pixel is a box with pixel area as ground area and the sensor thickness as height, in our case $55 \times 55 \times 1000\ \mu\mathrm{m}^3$. In order to resolve 3D particle tracks inside the sensor volume it is necessary to obtain position resolution along the height of the sensor. We name a detector that is able to perform this task a voxel detector.

As high resolution voxel detectors, semiconductor detectors might be used for efficient high energy single photon Compton-imaging. The direction of origin of an impinging X-ray photo could be determined by reconstructing the track of the Compton scattered electron. Further, it could allow the usage for low activity tracers in SPECT imaging as the collimator, which absorbs most of the flux, could be avoided. Additionally, Compton-imaging could be used for security application; for instance, if a method for fast and precise detection of nuclear contamination is needed [3,4].

[1] The decay of ^{116}Cd could in principle be observed with a cadmium-telluride semiconductor detectors, wherefore this particular isotope is chosen as an example here.

[a] e-mail: mykhaylo.filipenko@physik.uni-erlangen.de

[b] e-mail: thomas.gleixner@physik.uni-erlangen.de

Published online: 16 August 2014

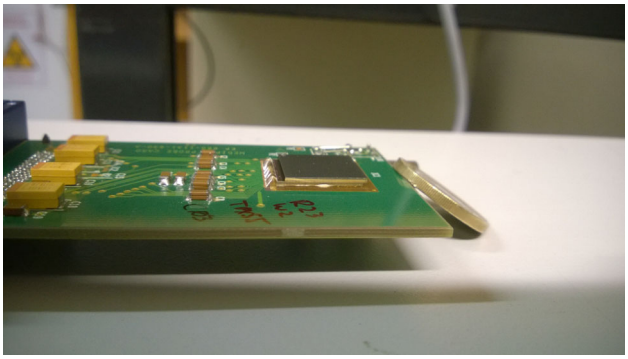

Fig. 1 A Timepix detector with a 1 mm thick cadmium-telluride sensor

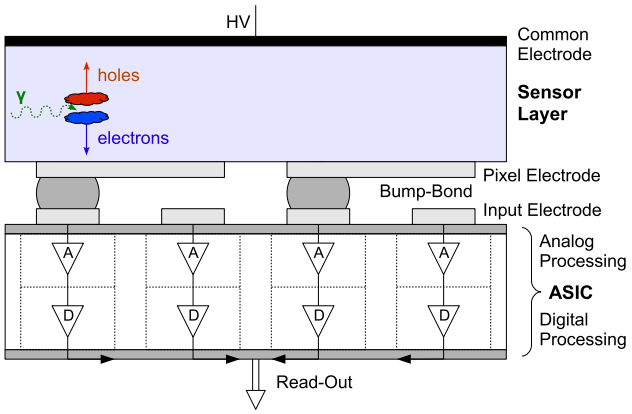

Fig. 2 Schematic cut through a Timepix-detector with a CdTe sensor layer with and block diagram that illustrates the signal processing in the *A* analogue and *D* digital parts of the ASIC. A high-voltage is applied to the sensor volume. The common electrode is at negative HV, the pixel electrodes at approximate ground potential. Electrons and holes are generated by ionizing radiation and drifted by the electric field. During the drift the charge carriers induce mirror charge currents at the pixel electrodes which are integrated and converted to a voltage pulse by the analog electronics in the ASIC

3D imaging of particle tracks could also allow to perform a variety of other important low-background experiments like the observation of the double electron capture. Summing up, the development of voxel semiconductor detectors would enhance the possibilities of detection in various fields.

In this publication we present a method for the reconstruction of such 3D trajectories through the sensor layer. It was developed and optimized with simulations. Also, the method could successfully be applied to experimental data obtained with a Timepix detector [5] and used for the reconstruction of electron tracks through the sensor layer.

The paper is structured as follows: In the second section the Timepix detector is explained as our simulations and experiments are based on this technology. In the third section the reconstruction method is described and in the fourth section the experimental results are presented. Section 5 gives an outlook on the current detector development which could lead to a fully operable voxel detector with about 50 µm voxel size.

2 The Timepix detector

The Timepix detector (s. Fig. 1) is a pixelated hybrid semiconductor detector which was originally developed for X-ray imaging applications [5]. Hybrid in this context means that the sensitive sensor layer and the ASIC are fabricated separately and afterwards connected together via bump-bonds. This has the advantage that different semiconductor materials can be used for the sensor layer. For X-ray imaging it is desirable to have a sensor material with a high atomic number in order to achieve high absorption efficiency. Hence, besides silicon cadmium-telluride was established as a sensor material for Timepix devices. Despite the difficulty of obtaining large high quality cadmium-telluride crystals the advantage of room-temperature operation and an atomic number of 48 and 52, respectively, makes this material preferable (to germanium) for X-ray imaging applications.

A scheme of the Timepix structure and functionality is shown in Fig. 2. The Timepix used in this study consists of a 1 mm thick cadmium-telluride sensor with metal electrode pads (ohmic contacts) as pixel electrodes at the bottom and a common electrode for the high-voltage connection at the top. The sensitive sensor layer is connected pixel-by-pixel to the input pixel electrodes of the ASIC by indium-tin bump-bonds. The pitch of the input pixel electrodes is 55 µm. There are 256 × 256 pixels on the ASIC which corresponds to an active area of 1.4 × 1.4 cm^2. In our detector only every second pixel in each row and column is bump-bonded wherefore the effective pixel size is 110 µm. This has the advantage of better energy resolution at the cost of position resolution. The ASIC is mounted on a printed circuit board and connected to the computer by a USB-FitPix readout [6] for data transfer to the data acquisition computer which can provide up to 60 frames per second. The output data is provided in frames. Each frame is a 128 × 128 matrix of values obtained for every pixel during the frame-time. The frame-time can be preset manually to a fixed time or the frame-start/frame-stop can be controlled externally by a trigger.

The sensor layer can be biased with a voltage up to 800 V. Free electrons and holes produced by ionizing radiation are separated and afterwards drifted by an electrical field in opposite directions. While approaching the pixel electrode the charge cloud induces mirror charges in the pixel electrodes. In each pixel the induced charge is collected and converted into a triangularly shaped pulse by a Krummernacher type preamplifier with an approximate peaking time of about 100 ns. The length of the pulse is about several microseconds which is mainly determined by the falling edge of the pulse.

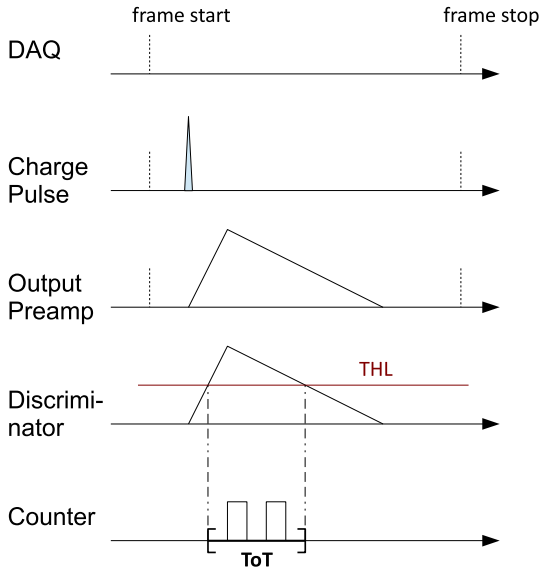

Fig. 3 Operation of the Timepix in the "time-over-threshold" (ToT) mode. After the charge pulse is amplified and converted to a voltage pulse, it is discriminated against a threshold level (THL). The time-over-threshold is the number of clock counts in the time interval of the pulse above the THL

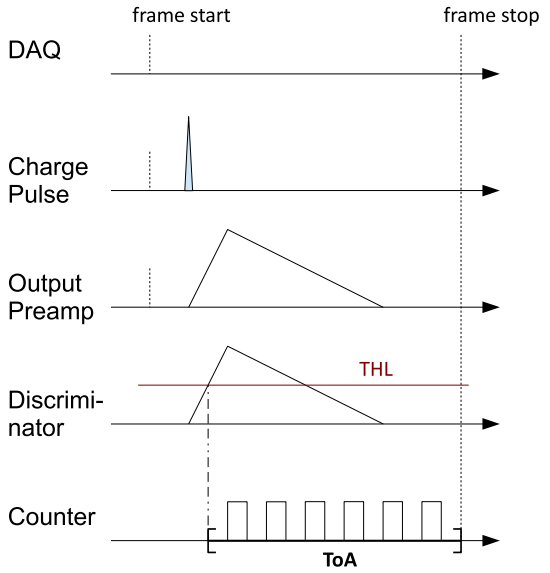

Fig. 4 Operation of the Timepix in the "time-of-arrival" (ToA) mode. After the charge pulse is amplified and converted to a voltage pulse, it is discriminated against a threshold level (THL). The time-of-arrival is the number of clock counts between the first time the voltage pulse rises above the THL and the end of the frame

The gain and the slope of the falling edge of the preamplifier can be set externally by a digital-to-analog converter in the matrix periphery. The pulse in each pixel is discriminated against a global threshold.

The electric post-processing of the signal in every pixel is digital and can be carried out in three different ways. We used the detector only in two modes—the "time-over-threshold" (ToT) mode and the "time-of-arrival" (ToA) mode. Both modes are illustrated in Figs. 3 and 4, respectively.

In the ToT mode a digital register starts counting clock cycles when the pulse rises over the threshold. The register stops once the pulse falls below the threshold and the number of counts in-between is the time-over-threshold. The frequency of clock cycles can be chosen between 10 and 100 MHz. The time-over-threshold is related to the height of the pulse which is a measure for the energy deposited in a pixel. Thus, the time-over-threshold can provide calorimetric information about a detected event. The deposited energy and the ToT are related in a non-linear way. The energy resolution achievable in this mode is 8.0 % (FWHM) at 59.56 keV and 5.4 % (FHWM) at 122.06 keV. Details on the calibration and the energy resolution can be found in [7].

In the ToA mode the register starts counting on the rising edge of the pulse and stops only at the end of the frame. As every frame gets a global time stamp, the ToA provides a timing information for every event. It can be as good as 10 ns for every pixel if a 100 MHz clock is used. The maximum counter value is 11280 which corresponds to a frame-time of 112.8 µs at a 100 MHz clock frequency.

3 Reconstruction method

In order to reconstruct the three-dimensional structure of particle trajectories through the sensor material, it is necessary to determine the depth of interaction z_n^0 in the sensor for every triggered pixel n (Fig. 5). Without loss of generality, we assume that the sensor is pixelated in the xy-plane and the depth of interaction is to be calculated along the z-axis. The sensor anode is at $z = 0$ and the cathode is at $z = d$; d being the sensor thickness.

3.1 Principle of reconstruction

The reconstruction is based on the charge carrier propagation mechanism in the sensor layer. Charge carriers are drifted in z-direction due to an electric field that can be approximated in a CdTe sensor layer by

$$|E_z(z, U)| = U(f_2 + f_1 z + f_3 \exp(-f_4 U z)) \tag{2}$$

which is an empirical fit to experimental data [8]. The parameters f_1 to f_4 are $f_1 = (5.80 \pm 0.09) \cdot 10^5\ \mathrm{m}^{-2}$, $f_2 = (228 \pm 7.5)\ \mathrm{m}^{-1}$, $f_3 = (540 \pm 144)\ \mathrm{m}^{-1}$ and $f_4 = (479 \pm 216)\ (\mathrm{Vm})^{-1}$. U is the voltage difference applied to the sensor volume. The drift velocity for electrons can be calculated as $v_z(z) = \mu_z E(z)$ where μ_z is the mobility of electrons in the z-direction ($\mu_z \approx 1100\ \frac{\mathrm{cm}^2}{\mathrm{Vs}}$ in CdTe). Further, the motion of a charge carrier in the sensor is described by the following equation:

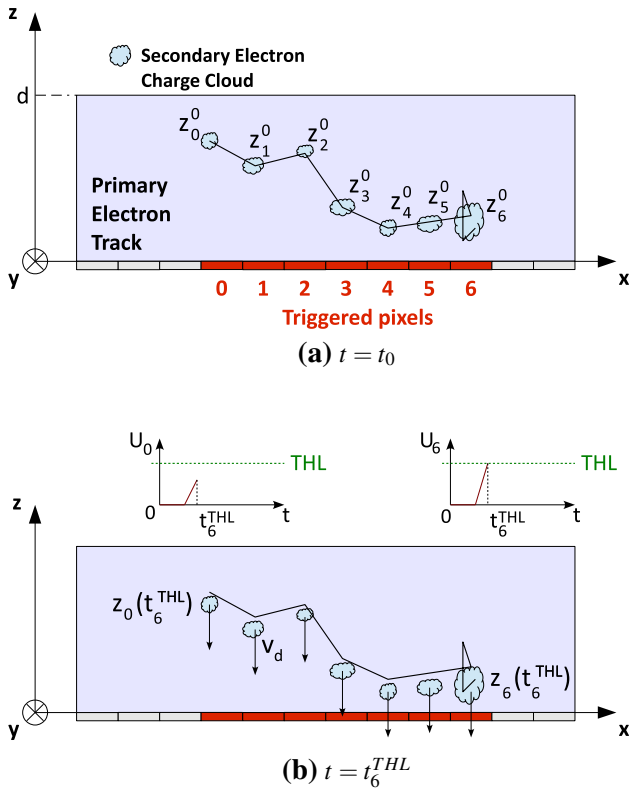

Fig. 5 A cut through a pixelated detector which illustrates the goal of the reconstruction. The depth of interaction z_n^0 should be reconstructed for every pixel. The triggered pixels are *red*. **a** The event happens at t_0; **b** a snapshot at $t = t_6^{THL}$: All electron clouds were drifted towards the pixel electrodes. In pixel 6 the electron cloud is close enough to the electrode for the voltage pulse (U_6) to exceed the threshold (THL). At the same time the voltage pulse in pixel 0 (U_0) has not reached the threshold yet

$$z(t) = z_0 + \int_0^t E(z(t'))\mu_z \mathrm{d}t' = z_0 + \mu_z U \int_0^t f_2 + f_1 z(t') + f_3 \exp(-f_4 U z(t'))\mathrm{d}t'. \quad (3)$$

Since this integral equation has no closed analytical solution for z(t), we used a numerical method to solve for z(t). We divided the total path between the anode and cathode into 20000 segments on which Eq. 2 can be approximated by a linear dependence on every segment i: $|E(U, z)| = U(a_i + b_i \cdot z)$ (for every segment i, the parameters a_i and b_i are calculated). With this approximation Eq. 3 can be solved and we have a sufficient solution for z(t) on every segment.

As stated in the previous section the signal that is actually measured is the amount of charge that is induced in the pixel electrode by the charge cloud of secondary electrons during their drift through the sensor. We consider only the charge induced by the electrons and neglect the charge that is induced by the holes. The mobility of holes is $\mu_h \approx 100\ \frac{\mathrm{cm}^2}{\mathrm{Vs}}$, hence more than 10 times lower than the mobility of the electrons. Also the weighting potential at the cathode is less steep

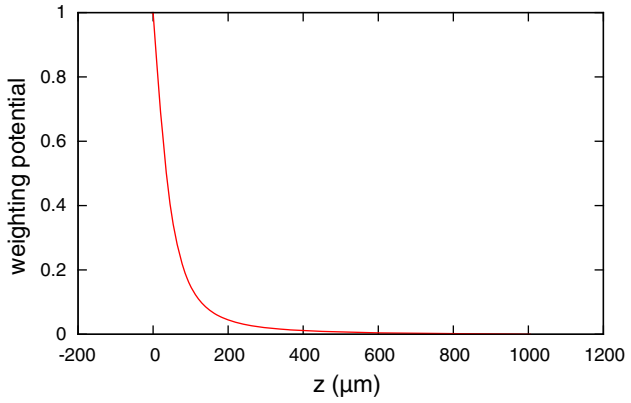

Fig. 6 The weighting potential in a 1 mm thick CdTe-sensor with 110 μm pixel size in z-direction calculated with the method of Castoldi et al. [10]

than at the anode. Therefore, the main contribution of the holes to the signal happens after the integration time of the preamplifier and can be neglected.

Suppose the charge Q_n^{dep} was released at the time t_0 above the pixel electrode n and is drifted from its initial position z_n^0 over a time period t_d. After this time period, the amount of charge that is induced in the pixel electrode Q_n^{ind} can be calculated as [9]

$$Q_n^{ind}(t_d) = \left[W_{pot}(z_n(t_d)) - W_{pot}(z_n^0)\right] Q_n^{dep}. \quad (4)$$

The function W_{pot} is called the weighting potential and takes into account the geometric properties of the sensor with its pixel electrodes. It can be determined by solving the Laplace-equation for a given geometry [10]. For our geometry of electronic pads the weighting potential along the z-axis is shown in Fig. 6. It was calculated with the method of Castoldi et al. [10].

For every pixel the threshold equivalent charge (or energy) is known after it has been determined in a calibration process. We will call this quantity Q_n^{THL}. Suppose this amount of charge was induced in the pixel after the time t_n^{THL}, then Eq. 4 yields

$$Q_n^{THL} = Q_n^{ind}\left(t_n^{THL}\right) = \left[W_{pot}\left(z\left(t_n^{THL}\right)\right) - W_{pot}\left(z_n^0\right)\right] Q_n^{dep}. \quad (5)$$

If a detector could measure t_n^{THL}, the position z_0^n could be determined by solving Eq. 5. Since $z_n(t)$ depends also on z_n^0 (Eq. 3) in a non-trivial way, the equation cannot be solved analytically. Instead it can be evaluated numerically by iteration: We set z_0^n to $\frac{d}{2}$ in the first step ($j = 1$) and for every pixel we calculate the expression

$$\Delta Q_n\left(z_n^0\right) = Q_n^{THL} - \left[W_{pot}\left(z_n\left(t_n^{THL}\right)\right) - W_{pot}\left(z_n^0\right)\right] \times Q_n^{dep}. \quad (6)$$

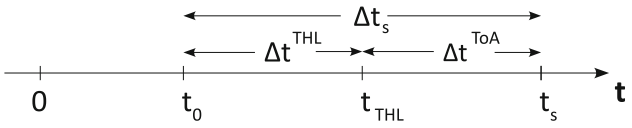

Fig. 7 An illustration of the points in time and time intervals occurring during the drift process. The interaction of the ionizing particle with the sensor happens at t_0. At t_{THL} the charge pulse (in a particular pixel) rises above the threshold. At t_s the frame stops

In the case $\Delta Q > 0$ we increase z_n^0 by $\Delta z_{shift} = \frac{d}{2^j}$ where j is the step number. In the opposite case ($\Delta Q < 0$) we decrease z_n^0 by Δz_{shift}. The deviation of the calculated position from the actual position is smaller than $\frac{d}{2^j}$ after the j-th step. Therefore, we used 30 steps in our analysis which produces a sufficient numerical accuracy for z_n^0.

However, an absolute measurement of t^{THL} would require to measure the time of interaction of the incident particle with the sensor. With a semiconductor this is impossible since the charge signal is always delayed by the time that it takes to induce a signal at the pixel electrode; and this time - in turn - depends on the depth of interaction.

What a detector can measure is a time-of-arrival for the charge signal in every pixel in the track relative to a fixed time-stamp set by the electronics t_s. We will call this quantity Δt_n^{ToA}; the time between t_0 and t_n^{THL} is called Δt_n^{THL}; the time between t_0 and t_s is referred to as Δt_s. This is illustrated in Fig. 7. According to Fig. 7 Δt_n^{THL} can be calculated as

$$\Delta t_n^{THL} = \Delta t_s - \Delta t_n^{ToA}. \tag{7}$$

In the last formula Δt_s is unknown but this quantity is the same for every pixel. By varying Δt_s the center of gravity in z-direction (the z-value averaged over all pixels) is shifted since the Δt^{ToA} values are fixed. It can be calculated as

$$\langle z \rangle = \frac{1}{Q} \sum_{n=0}^{N} z_n^0 Q_n^{dep} \tag{8}$$

where $Q = \sum_{n=0}^{N} Q_n^{dep}$ is the total released charge in the interaction. The ratio of the anode and cathode signal depends on the average depth of interaction [11]. It can be determined after measuring the total induced charge at the anode Q_a ($Q_c = Q$) and at the cathode Q_c and comparing the Q_c/Q_a ratio to a simulation-generated lookup-table. We will call this quantity $\langle z \rangle^{meas}$.[2]

[2] If both sides were pixelated, the weighting potential would be flat within most of the sensor volume. Consequently $W_{pot,A}$, $W_{pot,C}$ and thus $\frac{W_{pot,A}}{W_{pot,C}}$ would be almost constant within most of the sensor volume and the determination of $\langle z \rangle^{meas}$ would not work properly. However, since the cathode is not pixelated, its weighting potential is rather linear like in a plate capacitor, which is quite different from the pixelated anode. Therefore it allows to determine $\langle z \rangle^{meas}$ from the ratio of the anode and cathode signals.

If Δt_s is assumed too high, then we get $\langle z \rangle^{meas} < \langle z \rangle$ because we overestimated the drift distance. In the opposite case we get $\langle z \rangle^{meas} > \langle z \rangle$ because we underestimated the drift distance. Therefore, Δt_s can be determined in the same iterative procedure as z_n^0 under the condition

$$\begin{aligned} \Delta z &= \langle z \rangle^{meas} - \langle z \rangle \\ &= \langle z \rangle^{meas} - \frac{1}{Q} \sum_{0}^{N} z_n(\Delta t_s) Q_n^{dep}. \end{aligned} \tag{9}$$

3.2 Reconstruction procedure

Based on the physics and the method described in the previous subsection a detector has to be able to measure the following quantities for a 3D track reconstruction:

- The total charge induced at the cathode Q_c.
- The charge released over every pixel Q_n^{dep}.
- The time-of-arrival of the charge signal in every pixel Δt_n^{ToA}.

Based on this information, the calibration of the detector (Q_n^{THL}) and the properties for the sensor layer (μ, $E_z(U, z)$, $W_{pot}(z)$) the reconstruction algorithm operates as follows:

1. Compute numerically $z(t)$ for a given electric field configuration $E(U, z)$ in the sensor layer.
2. Determine the real average depth of interaction for the track from the Q_c/Q_a ratio and the lookup-table.
3. Fix an arbitrary value for Δt_s and vary z_n^0 for every pixel under the condition in Eq. 6. In practice it is reasonable to choose a value between 0 and $t_s - t_{max}$ for Δt_s (for instance $\frac{t_s - t_{max}}{2}$), where t_{max} is the drift time from the top of the sensor layer to the bottom.
4. Vary Δt_s under the condition given by Eq. 9 and repeat the previous step to reconstruct the correct positions z_n^0 for every pixel.

We tested our reconstruction method on data produced by the in-house developed Monte-Carlo simulation named ROSI [12,13]. It is based on EGS4 and has a low energy extension with the interaction code LSCAT. For each event the simulation propagates the corresponding particle through the sensor and calculates charge deposition in the sensor layer. For a background electron of 2.8 MeV[3] it produces about 5000–10000 interaction points along the track. Afterwards the drift of the secondary electrons and the signal generation in the pixel electrodes is simulated. The simulation takes into account the diffusion and recombination properties of CdTe

[3] 2.8 MeV is the Q-value of the double beta decay for ^{116}Cd. This would be the isotope under investigation in a neutrinoless double beta experiment with Timepix-based cadmium-telluride detectors.

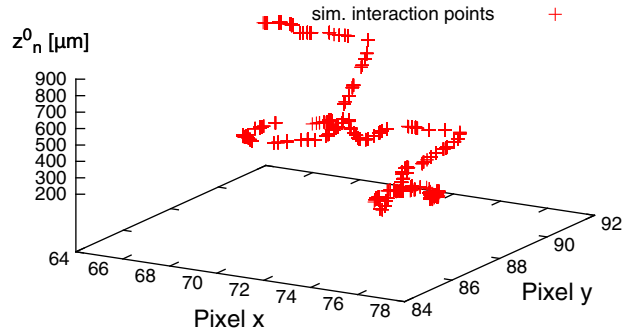

(a) Simulated Track

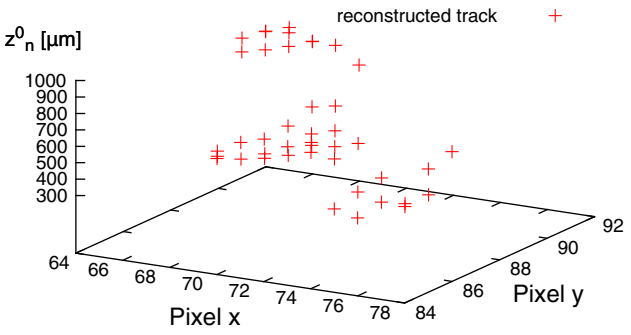

(b) Reconstructed Track

Fig. 8 Example of a simulated track (with all interaction points) and the reconstruction of this track obtained from pseudo-measured data

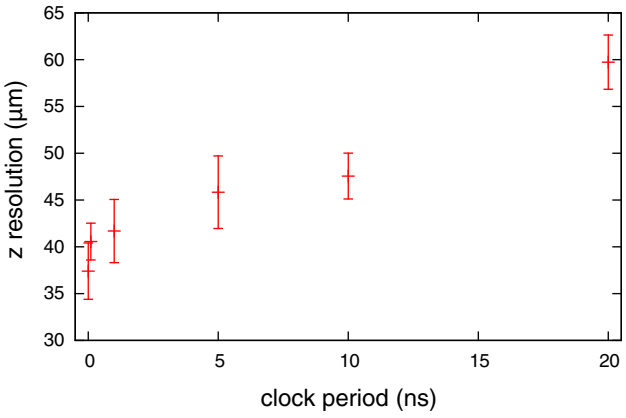

(a) Time Resolution

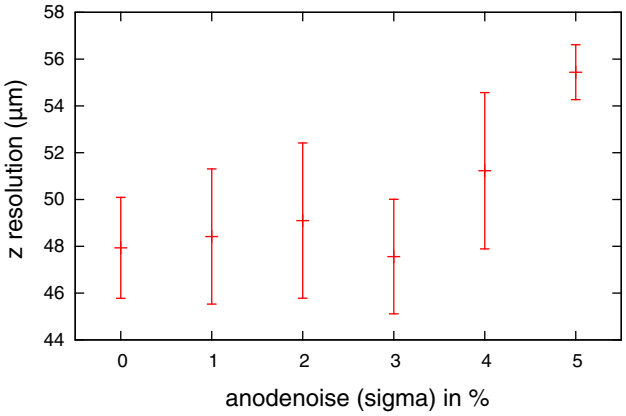

(b) Energy Resolution

Fig. 9 The interdependence between the z-position resolution $FWHM_z$ and the time resolution (**a**); and the energy resolution (**b**). The *error bars* are the given by the standard deviation if the simulation is repeated several times with the same configuration

as well as the repulsion of the charges under their electric field.

In Fig. 8a the complete track (with all interaction points) of a 2.8 MeV electron is shown and in Fig. 8b the reconstructed track. The reconstruction uses the quantities that would be obtained with a detector of 110 µm pixel size, a 1 mm thick sensor layer with 44.8 V applied bias voltage, an energy threshold of 5 keV and a time resolution of 10 ns in every pixel.

The position resolution in z-direction depends on the charge resolution (which is equivalent to the energy resolution) of the cathode and anode signals as well as on the time resolution. Figure 9a shows the dependence of the z-resolution $FWHM_z$ on the time resolution if the energy resolution ($\frac{\sigma(E)}{E} = 2\,\%$) is fixed. Figure 9b illustrates how the $FWHM_z$ depends on the energy resolution under for a fixed time resolution (10 ns).

4 Experimental results

For an experimental test of our method we performed two different experiments. For both experiments we used a Timepix detector with a 1mm thick cadmium-telluride sensor. The detector was bump-bonded and assembled by X-ray Imaging Europe GmbH. The energy threshold of our particular detector was about 7 keV. We used the detector at a bias voltage of 44.8 V. The reason for this is to increase the drift time of the electrons to preferably high values. In contrast to the usual application of imaging where the drift time should be as low as possible for fast counting, we need it to be rather long. The maximum clock frequency that could be used was 100 MHz which corresponds to pulses of 10 ns length. At the usual voltage (500 V) the drift time is about 20 ns which is faster than the peaking time after the preamplifier (about 100 ns). We need the electron drift time to be significantly larger than that in order to measure drift time differences between individual pixels. According to our simulation the drift time at 44.8 V is about 200 ns. We chose a bias of about 45 V but not lower since the charge collection efficiency saturates at about 40–50 V. Hence, the chosen voltage is a reasonable tradeoff between a sufficient charge collection efficiency for a good signal in each pixel and a large drift time for a "time-of-flight" position reconstruction.

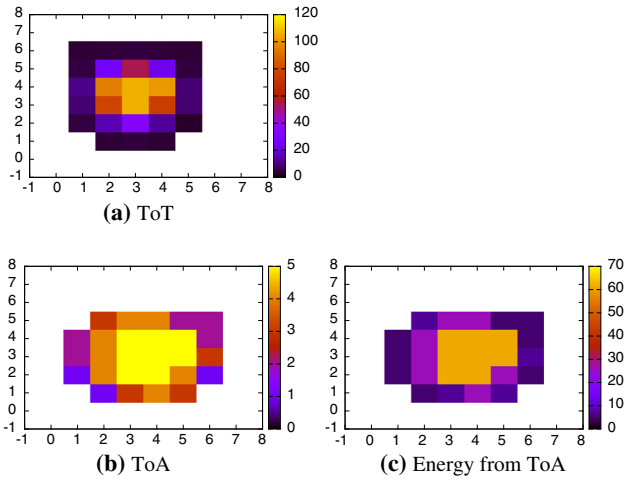

Fig. 10 A typical α-particle event measured in **a** ToT mode; **b** ToA mode. Image **c** shows the event with energy reconstructed from ToA data. The *color* denotes the ToT in clock cycles, the ToA in clock cycles and reconstructed energy in keV, respectively

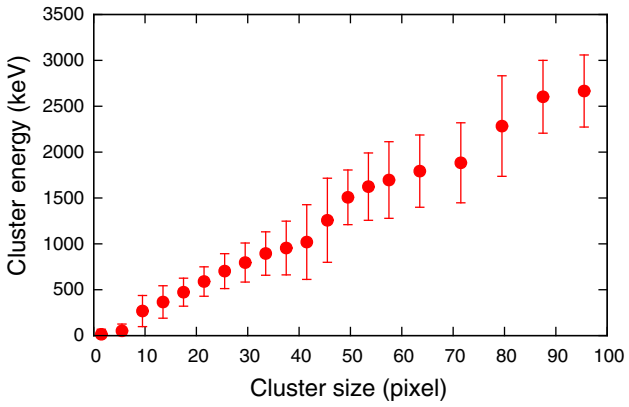

Fig. 11 The correlation between energy and cluster size from α-particle events. The *error bars* show the RMS at each point

Before the measurements we performed a global ToT calibration for the detector. The method of calibration is described in [7]. We used two calibration energies: 59.56 keV from ^{241}Am and 80.99 keV from ^{133}Ba.

4.1 Reconstruction of α-particle energy deposition distributions

Originally, in our method the z-position (depth of interaction) for every pixel triggered in an event is reconstructed from the simultaneous measurement of the total deposited energy, the energy deposited in every pixel and a timing information in every pixel. However, according to Eq. 5 the method can also be adapted to reconstruct the energy deposition in every pixel from the timing information, the total deposited energy and the knowledge of the z-positions. In this case the quantity Q_n^{ind} (which is equivalent to the deposited energy) for every pixel is calculated numerically in 30 iterations with Eq. 6.

With the Timepix it is impossible to obtain all of the three quantities simultaneously. Nonetheless, in order to show the functionality of the method, it was possible to overcome this disadvantage in the following way: We placed a ^{241}Am source with an activity of about 310 kBq close to the sensor surface. The source emits α-particles that deposit a particular energy within the first 15 µm of the sensor layer. Therefore, within good accuracy $z_n^0 = 0$ can be used for all pixels in the reconstruction which removes one parameter.

First, we measured the energy deposition distribution per pixel in the ToT mode. A typical event cluster in ToT mode is shown in Fig. 10a. The colour denotes the deposited energy in keV. A cluster is a set of pixels which are direct neighbours. Usually, there are several such clusters in a single frame. An algorithm recognizes the clusters and they are treated as individual events in the further analysis. By summing up all the energy values in the cluster we obtained the total deposited energy. The total deposited energy is linearly correlated with the cluster size (the number of triggered pixel in an event) as shown in Fig. 11. As the cluster size is not affected by the mode of operation, we can use this correlation to determine the total deposited energy for α-events measured in the ToA mode.

As next, we recorded a similar number of events in the ToA and the ToT mode. A typical event in ToT, ToA and energy reconstructed from ToA are shown in Fig. 10a–c, respectively. Apparently, the dynamic range in the ToA data is lower since the total drift-time across the sensor layer is 200 ns and the clock that we used for this experiment was 48 MHz. Therefore, the maximum number of time slices is limited to 5.

A comparison between the energy distribution obtained in the ToT mode and reconstructed from the data in ToA mode is shown in Fig. 12. The fraction of energy deposited in a pixel is plotted versus the distance from the center of the event. The discrepancy has multiple reasons: In the central region of the cluster the amount of released charge is so high that the induced charge goes over the threshold very quickly and the drift time differences cannot be resolved with a resolution of 21 ns. Additionally, the charge is distributed among the pixels by charge sharing but we treat them as if the charge was initially released in the pixels. The result of this experiment suggests that the method has to be improved in the case of charge sharing but also highlights that the method works in principle.

4.2 Reconstruction of electron tracks

4.2.1 Experimental design

The second experiment was intended to demonstrate that 3D tracks can be reconstructed. Again, as the Timepix in its current version cannot measure all necessary quantities at the

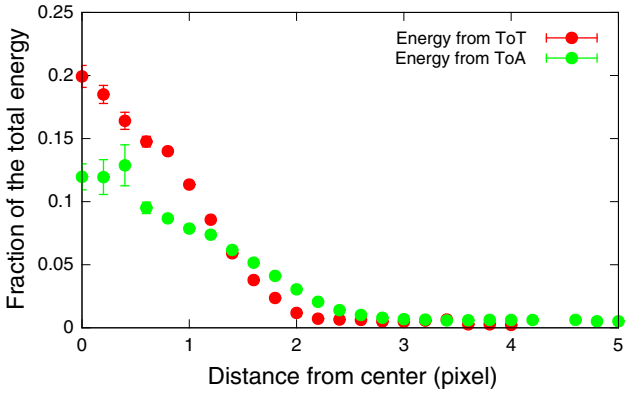

Fig. 12 The distribution of pixel energies of α-events obtained from ToT data (*red*) and reconstructed from ToA data (*green*). The curves were averaged over many events. The *error bars* were calculated as the RMS divided by the square root of the number of triggered pixels in a bin. Their size is governed for example by the underlying event statistics, by the granularity of the pixel matrix and by the shape of the clusters of pixels triggered by α-particles

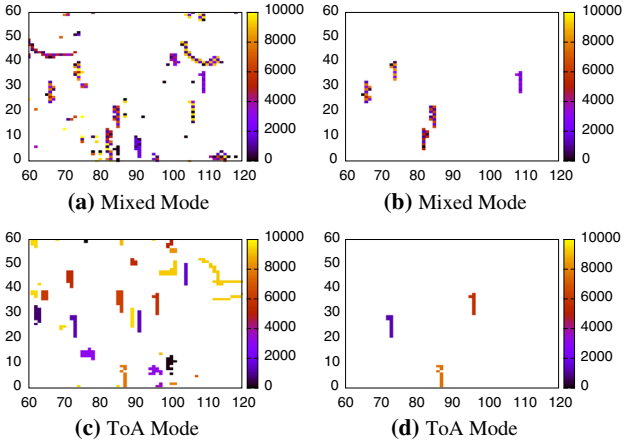

Fig. 13 Typical tracks for the evaluation of the z-resolution before (**a**, **c**) and after (**b**, **d**) track selection in the mixed-mode (**a**, **b**) and in the ToA mode (**c**, **d**). The *colour bar* denotes the measured ToA or ToT in every pixel

same time, we designed our experiment in such a way that the parameters that cannot be measured by the detector directly, can be accessed and determined otherwise.

We used the Timepix in a so-called mixed matrix mode and took advantage of the fact that minimal ionizing particles deposit roughly the same energy in every pixel along its track. The Timepix allows to assign every pixel individually a mode of operation either ToA or ToT. For our experiment we chose the modes in a checkerboard arrangement—every pixel has a diagonal neighbour that is in the same mode and an off-diagonal neighbour that is in the different mode. It is a reasonable approximation to assume that minimal ionzing particles deposit nearly the same energy in every pixel. Hence, one can determine the energy deposited in a pixel that runs in the ToA mode by calculating the average value of deposited energy in the surrounding triggered ToT pixels. The second advantage of minimal ionizing particles is that they propagate through the complete sensor on an almost straight line. Thus, we know that the average z-position of the track is $\langle z \rangle^{meas} = \frac{d}{2}$ without measuring the total charge at the common electrode.

Another way to determine the averaged deposited energy in every pixel is to take data in ToT mode and afterwards without changing the angle between the beam and the sensor layer to take data in ToA mode. From the ToT measurement we can determine the energy deposition in every pixel and afterwards the ToA data can be used for z-position reconstruction under the assumption that approximately the same energy was deposited in every pixel for each measurement in ToT and ToA mode under a fixed angle.

The data with minimal ionizing particles was acquired at the DESY T21 testbeam. We used an electron beam at 4.4 GeV. The sensor layer was positioned under two different angles to the beam direction. In one case the angle was about 42° and we obtained short tracks of 8–9 pixels on average and in the other case (10°) the tracks were 55–56 pixels long in average. The frame-time was 120 µs wherefore two tracks never overlap on one frame. We took data in the mixed, the ToT and the ToA mode.

4.2.2 *Data analysis and results*

For the evaluation of the resolution that we achieved in z-direction we performed a selection of tracks and sorted out tracks which are not meaningful due to the following criteria: first, we rejected tracks where at least one pixel counted a ToA value of at least 9465 which is the maximal ToA value that can be expected with the used frame time and clock frequency. With this cut, tracks were ignored which occurred shortly before or right at the beginning of the frame. For these tracks the exact moments of detection cannot be determined due to the ToA measurement principle of the Timepix. Secondly, the electron beam was in x-direction while the detector was placed in the yz-plane and then tilted along the y-axis. Thus, as the tracks from minimal ionizing events are straight lines, meaningful events should trigger pixels mostly in one x-column. For events which do not produce straight lines due to scattering in the sensor our reconstruction will give false results since the assumption $\langle z \rangle^{meas} = \frac{d}{2}$ is not fulfilled. Hence, we used the following additional criterion for event selection: Only tracks which had twice as much triggered pixels in one x-column than in other columns combined are taken into account. Since hardly any long tracks fulfilled this criteria, we used only the short tracks for the further analysis. At last, we used only tracks with at least 10 triggered pixels to avoid background from low energy events. Figure 13a–d show a sample of tracks before and after event

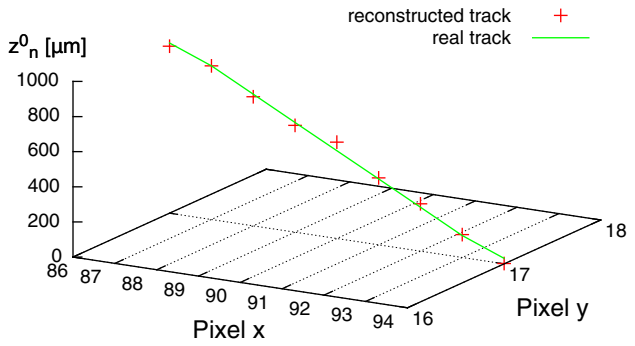

(a) Short Track

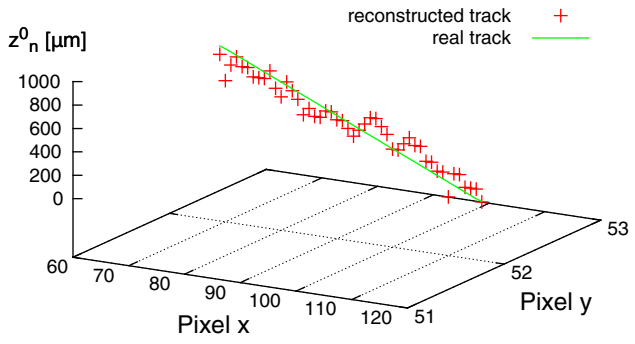

(b) Long Track

Fig. 14 A reconstructed track of a typical short and long track after reconstruction in comparison to the real track. The tracks go parallel to the x-axis wherefore the y-values are the same for all voxels

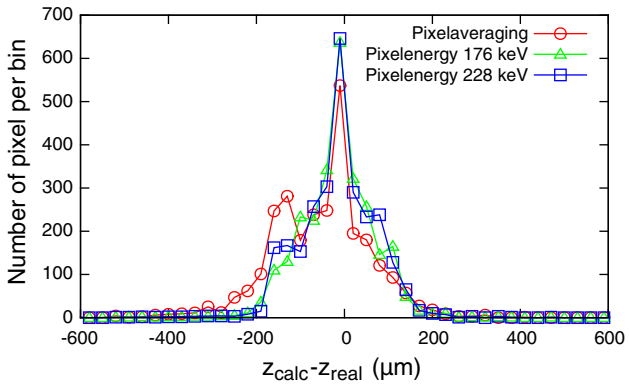

(a) Mixed Mode

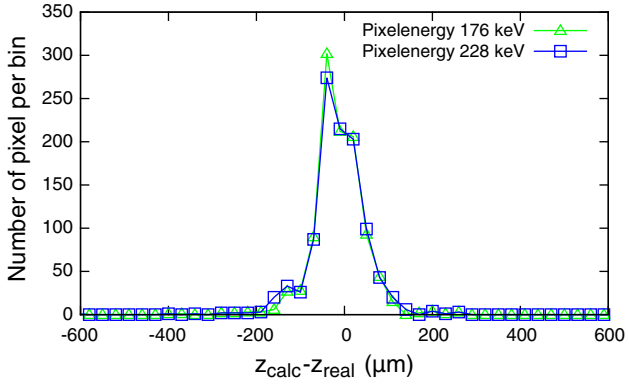

(b) ToA Mode

Fig. 15 The deviations of the reconstructed z-position from the actual track for events measured in mixed mode (**a**) and ToA mode (**b**)

Table 1 Results on the z-resolution obtained in different modes of operation

	Mixed mode (µm)	ToA mode
Neighbours averaging	119	–
All pixel at 228 keV	91	66 µm
All pixel at 176 keV	89	63 µm

selection in the mixed-mode and in the ToA mode, respectively.

The experiment with α-particles showed that our algorithm can give unsatisfying results for charge sharing pixels. Therefore, we removed pixels which are not in the main x-column as these are probably due to charge sharing. Also, we removed pixels with the highest y-coordinate values as these are most probably due to charge sharing from the pixels where the electron entered and left the sensor layer.

A typical track in comparison to the expected track for each case (long and short) is shown in Fig. 14a, b, respectively. At this point it is important to mention that the algorithm is not biased in any way to reconstruct a straight line. The fact that the result of reconstruction is a straight line indeed is a strong indicator that our method works properly. The reconstructed points are scattered close around the actual particle trajectory which indicates a meaningful result.

We calculated the z-resolution as the root mean square (RMS), where the reference z-value in every point was determined by a line fitted through the pixels with the highest and the lowest y-values (green line in Fig. 14). This line is what comes closest to the real particle trajectory. The results are summarized in Table 1. Figure 15a, b shows the deviations of the reconstructed z-position from the actual track.

In the mixed-mode we achieved a z-resolution of 119 µm. By using the data from ToA only and a fixed energy of 228 keV we achieve a z-resolution of 66 µm. This value for the average energy was determined from the ToT measurement as the average deposited energy per pixel. However, since this energy is a constant for all pixels in the reconstruction, it can also be set to a different fixed value. It turns out that the best resolution of 63 µm could be achieved by using the data from ToA mode and a fixed energy of 176 keV for every pixel. For the mixed-mode we obtained a resolution of 91 µm with a fixed energy of 228 keV and 89 µm with a fixed energy of 176 keV.

The experiments were limited to straight tracks from minimal ionizing particles since the available detectors cannot provide all the information required for reconstruction. Nonetheless the next generation of Timepix detectors (Timepix3) [14] will provide a simultaneous read-out of timing and energy deposition information per pixel. Also the readout of a backside signal could be included as for a coplanar-grid-type of detector. With a proposed time resolution of 1.6 ns, a voxel detector with about 50 µm voxel size can be expected. A Timepix3 detector with a CdTe sensor could therefore provide an interesting opportunity for new imaging techniques with voxel detectors.

5 Conclusions and outlook

In this publication we presented and evaluated a method to reconstruct 3D particle trajectories through a sensor layer of a pixelated semiconductor detector. Our simulations suggests that a z-resolution of about 40–50 µm can be achieved under realistic detector performance assumptions.

As a major result, we successfully demonstrated that the method works experimentally and a particle track can be reconstructed from actual data. The achieved z-resolution was 63 µm in the best case.

Acknowledgments We would like to thank Dominik Dannheim and Ralf Diener for their help and giving us the opportunity to acquire data at the DESY test beam facility. Also, we would like to thank the Medpix Collaboration for their support. We are grateful to the Deutsche Forschungsgemeinschaft for supporting Thomas Gleixner.

Open Access This article is distributed under the terms of the Creative Commons Attribution License which permits any use, distribution, and reproduction in any medium, provided the original author(s) and the source are credited.
Funded by SCOAP[3] / License Version CC BY 4.0.

References

1. J. Schechter, J. Valle, Phys. Rev. D **25**, 2951 (1982)
2. P. Vogl, S. Elliott, Ann. Rev. Nucl. Part. Sci. **52**, 115 (2002)
3. B. Plimley et al., Nucl. Instrum. Methods A **654**, 244 (2011)
4. J. Kim et al., Nucl. Instrum. Methods A **683**, 53 (2012)
5. X. Llopart et al., Nucl. Instrum. Methods A **581**, 485 (2007)
6. V. Kraus et al., JINST **6**, C01079 (2011)
7. M. Filipenko et al., Eur. Phys. J. C 73, 2374 (2013)
8. T. Michel et al., Adv. High Energy Phys. **2013**, 105318 (2013)
9. W. Shockley, J. Appl. Phys. **9**, 635 (1938)
10. A. Castoldi et al., IEEE Trans. Nucl. Sci. **43**(1), 256 (1996)
11. W. Li et al., IEEE Trans. Nucl. Sci. **47**(3), 890 (2000)
12. J. Giersch et al., Nucl. Instrum. Methods A **509**, 151 (2003)
13. J. Durst, J. Giersch, Nucl. Instrum. Methods A **591**, 300 (2007)
14. M. van Beuzekom et al., in Proceedings of Science (SISSA, 2011), pp. 1–8

III.2 Comparison of the results with other neutrinoless double beta experiments

The energy resolution that we measured with a CdTe-Timepix detector at 1.588 MeV (pair production peak due to the 2.614 MeV γ-line of ^{208}Tl) is 3.8 % (FWHM). Compared to the two important xenon-based experiments (EXO and Kamland-Zen) the energy resolution is better than in case of EXO (5.8 % at 1.588 MeV [46]) and significantly better than in the case of Kamland-Zen (about 11.7 % at 1.588 MeV [47]). However, in the setup of Kamland-Zen only the scintillation signal is used which usually provides a worse energy resolution than ionization signal based detectors (compare sec. II.2.3). Nonetheless, these two experiments have the big advantage that liquid xenon (EXO) or xenon dissolved in a liquid scintillator (Kamland-Zen) is used, wherefore these technologies are easier to scale up to higher mass and to fiducalize which helps to reduce the background level.

Compared to GERDA, which also uses semiconductor detectors, the energy resolution is worse. The HPGe (high purity germanium) detectors employed in GERDA have an energy resolution of 0.2 % at 2.614 MeV and 0.7 % at 582 keV (thus, an energy resolution better than about 0.5 % at 1.588 MeV) [23].

Since these detectors have no pixelation, active background rejection can be performed mainly by pulse shape discrimination (so far). This technique is useful to reject α- and β-background from the detector surfaces or multi-site events (two events which happen at different parts of the sensitive volume simultaneously) [27] but not to distinguish between single or two electron events in the sensor directly. α-particles as well as multi-site events can be identified easily with the Timepix detector [48]. The advantage that the Timepix would offer in its current form would be a full rejection of α-particle and muon background, and a reduction of the electron background by about 75 % whereas the signal is reduced by 25 % [49]. The correponding background reduction factor for single electron events is 2.2[1] and the increase in sensitivity is about 1.2.

With an energy resolution of 1.5 % (according to simulations) at the Q-value and a background of $1 \cdot 10^{-3} \frac{\text{cts}}{\text{keV} \cdot \text{kg} \cdot \text{a}}$ (which is currently the goal for most upcoming experiments [22]), a sensitivity of 51 meV on the effective Majorana mass could be achieved at an exposure of 2100 kg years = 420 kg $\cdot$ 5 year[2]. GERDA would achieve this sensitivity at an exposure of about 1600 kg years. EXO (in its current form) would achieve this sensitivity at an exposure of roughly 5000 kg year. In Phase-I GERDA achieved a background-level of $2.0 \cdot 10^{-2} \frac{\text{cts}}{\text{keV} \cdot \text{kg} \cdot \text{a}}$ [26] and EXO200 achieved a background level of $1.5 \cdot 10^{-3} \frac{\text{cts}}{\text{keV} \cdot \text{kg} \cdot \text{a}}$ [46]. Therefore, it seems possible to reach the desired background level of $1.0 \cdot 10^{-3} \frac{\text{cts}}{\text{keV} \cdot \text{kg} \cdot \text{a}}$. However, the self-shielding effect of xenon and fiducializing contribute a lot to this low

1 The background reduction factor is defined as the ratio between the background level around $Q_{\beta\beta}$ before and after electron background rejection by pattern recognition.

2 The Timepix detectors used for an experiment of this target mass are assumed to have a pixel pitch of 165 µm, a sensor thickness of 3 mm and be well-calibrated.

background level. Thus, it is questionable if this background level can be achieved with thin CdTe-sensors as well, especially since there is no data on the radiopurity of CdTe-Timepix detectors available yet. In particular the composition of the background is important since backgrounds like α-particles or double Compton events occuring in different parts of the sensor can be identified and rejected very efficiently but events like a β-decay followed by internal conversion (IC) have the same topology as $0\nu\beta\beta$ events (and cannot be distinguished at all).

Although the achieved results may be only partially satisfying (in particular to justify the scalability problems with thin CdTe sensor layers), further enhancement in sensitivity could be achieved as a consequence of two things: On the one hand it can be expected that a full voxel detector will be realized in future by a Timepix-3 detector with backside read out and the reconstruction method that is presented here. Employing 3D tracking with a voxel pitch of about 50 µm for the rejection of single electrons would allow to increase the electron reduction rate to about 6.6 [49]. Also, this would allow to fiducialize the sensitive volume and thus background levels comparable to EXO might be feasible. On the other hand, as shown by the HEXITEC group, pixelated CdTe detectors can provide a very good energy resolution [50]. The HEXITEC has a pixel size of 250 µm and an energy resolution of about 2 % (FHWM) at 59.54 keV. This is about 3.8 times better than the current resuls with the Timepix. According to our results, with this pixel size artificial neural networks can still provide a proper background rejection of single electron background. An evaluation on the achievable sensitivity with this detector is in progress and will be published in the future.

At last, it might be important to state that the experiments which are closest to set new limits and maybe see first real evidence for $0\nu\beta\beta$ are GERDA, KamLand-Zen or EXO200. A $0\nu\beta\beta$ experiment based on the Timepix chip is not feasible in the near future. If significant progress (for instance such as described above) will be made in the field of pixelated CdTe-detectors, simulations indicate that a $0\nu\beta\beta$ experiment with pixelated CdTe-detectors could be meaningful. Its advantage would to be to provide additional confidence about the few events that one measures at $Q_{\beta\beta}$. To put into simple terms: If the track clearly looks like two electrons (as expected for a $0\nu\beta\beta$ decay) and not like a muon or an α-particle, the result could be more convincing. Thus, if an observation of $0\nu\beta\beta$ will be made for ^{76}Ge or ^{136}Xe in the future, an experiment with pixelated detectors might still be interesting to confirm the findings by an observation of $0\nu\beta\beta$ for ^{116}Cd in order to convince the particle physics community that $0\nu\beta\beta$ exists and neutrinos are Majorana particles after all.

IV A New Method for Particle Tracking by Scintillation Light

Contents

The usual way to include tracking in a neutrinoless double beta experiment is to build a time-projection chamber. The sensitive volume is often a liquid or gas (like in EXO or NEXT), or one could have a solid state time-projection chamber like presented in the previous section. Regardless of the sensor material, the functionality for tracking is based on drifting secondary electrons (or holes) through the sensitive volume and detect them by a segmented/pixelated read out at the bottom plane (see section II.2.3).

If materials with sufficient electron life-time are used for the sensor, it is possible to built detectors of large volume by using this technique. Such materials are high quality semiconductor crystals or highly purified noble gases. For instance, the drift distance for electrons in highly purified liquid xenon can exceed one meter [53]. However, if the electrons have to be drifted over such large distances, it is hardly possible to use the detector as a tracking device any more.

The reason for this is the diffusion of charge carriers in the horizontal plane during the drift of the charge carriers in vertical direction. Suppose a charge cloud starting at a particular point in the sensor volume drifts over a distance d in vertical direction with the drift velocity v_z. The radius wherein 90 % of the charge carriers will be randomly distributed (diffusion radius) is given by

$$r_D(d) \;=\; 4\sqrt{D(T,E_z)t} = 4\sqrt{(D(T,E_z)\frac{d}{v_z(E_z)}}. \tag{IV.1}$$

Here $v_z(E_z)$ denotes the drift velocity in z-direction, which depends on the strength of the electric field applied over the sensor volume in z-direction E_z. The diffusion constant D depends on the temperature T of the material and the electric field E_z[1] [51].

For common sensor materials like liquid xenon (that is considered to be realistically scalable to large masses as one single detector) the track length for the two electrons from a neutrinoless double beta decay is about 3 mm. When the diffusion radius is not substantially smaller than the track length, tracking is no longer possible since at the bottom plane any track will have a round indistinguishable form. With formula IV.1 and common values for $T = 165\,\mathrm{K}$, $D \approx 120\,\frac{cm^2}{s}$, $v_z(E_z) \approx 3 \cdot 10^5\,\frac{cm}{s}$ and $E_z \approx 3700\,\frac{V}{cm}$ (values taken from [54, 51] and [55]) in liquid xenon one can calculate the drift distance d after which tracking will be no longer possible. It is roughly $d \approx 5\,\mathrm{cm}$ to 6 cm. This distance is not sufficient for the height of a detector that would be favorable for a large scale neutrinoless double beta experiment - at least several decimeters (if one single detector is used).

A possible solution to this limitation would be to use the scintillation signal instead of the ionization signal for tracking. Scintillation photons, just as secondary electrons, are created along the trajectory of the primary ionizing particle. However, on their way through the sensor material photons travel onto straight lines and do not diffuse. In principle, this would allow to image tracks from a large depth in sensor volume (if a scintillator with sufficiently low self-absorption is used). Within the scope of this thesis, a "proof-of-principle" experiment for this technique was performed successfully and the position resolution was examined. We estimated the resolution to be 170 µm to 250 µm for tracks closely (about 0.25 mm to 0.6 mm) to the focal plane of the imaging optics. This is presented in the second publication.

Although the technique works in principle, the result indicates that the main limitation of the technique is connected to the depth of focus of the optics used for imaging. In order to image sharply (for instance with an blurring circle of no bigger than 10 µm) a volume of 30 cm (about 80 kg of liquid xenon) the distance of the optics to the scintillator has to be large (1 m) but also the focus of the lenses has to be small (15 mm) and therefore the lenses' diameter. In contrast, this reduces drastically the light collection efficiency which decreases the energy resolution or makes tracking impossible at all due to the low number of collected photons. One idea how to deal with this problem is discussed in the outlook section.

For this experiment a novel device, the hybrid photon detector, was used. In order to test the device and ensure a stable operation, it was calibrated beforehand, i.e. its absolute quantum efficiency was determined by the method of Klyshko [56]. The calibration experiment and its results are presented in the first publication. In the last section the

1 The dependence of the diffusion constant D on the electric field E_z is strong in materials like liquid and solid xenon where the mean free path of free electrons between collisions is long and therefore their mean kinetic energy is high [52].

HPD is compared to a similar device, the iCCD. Additionally, some other scintillation light based tracking techniques are presented for comparison (regarding the applicability for a neutrinoless double beta experiments).

IV.1 Publications

IV.1.1 Publication: Detection of non-classical space-time correlations with a novel type of single-photon camera

The publication "Detection of non-classical space-time correlations with a novel type of single-photon camera" (Opt. Expr. **22** (2014), 14) covers the following issues:

- Application of the novel camera (hybrid photon detector - HPD) for coincidence and quantum correlation experiments.
- Determination of the absolute quantum efficiency of the hybrid photon detector (HPD) for wavelengths from 535 nm to 570 nm.
- Determination of the absolute quantum efficiency of the hybrid photon detector (HPD) at 536 nm as a function of the applied voltage.

My own contributions to the publication:

- Preparation of the novel camera (hybrid photon detector - HPD) with periphery for the experiment.
- Design and implementation of the data acquisition system for coincidence measurements.
- Data acquisition.
- Contributions to data analysis (determination of the coincidence spectrum and the measurement time from the HPD raw data).
- Interpretation and evaluation of the results in discussion with the co-authors.
- Contributions to manuscript writing.

Contributions of the co-authors (in particular Felix Just and Andrea Cavanna) to the publication:

- Design and implementation of the optical setup.
- Contributions to data acquisition and analysis.
- Interpretation and evaluation of the results in discussion with the co-authors.
- Manuscript writing (corresponding author: Felix Just).

Detection of non-classical space-time correlations with a novel type of single-photon camera

Felix Just,[1,*] Mykhaylo Filipenko,[2], Andrea Cavanna,[1] Thilo Michel,[2] Thomas Gleixner,[2] Michael Taheri,[1] John Vallerga,[3] Michael Campbell,[4] Timo Tick,[4] Gisela Anton,[2] Maria V. Chekhova,[1,5,6] and Gerd Leuchs[1,6]

[1]*Max Planck Institute for the Science of Light, Günter-Scharowsky-Straße 1/Bau 24, 91058 Erlangen, Germany*
[2]*Friedrich-Alexander University of Erlangen-Nürnberg Erlangen Centre for Astroparticle Physics Erwin-Rommel-Str. 1 91058 Erlangen*
[3]*Experimental Astrophysics Group, Space Sciences Laboratory, University of California Berkeley, CA 94720, USA*
[4]*European organization for Nuclear Research, CERN, CH-1211, Geneve 23, Switzerland*
[5]*Department of Physics, M. V. Lomonosov Moscow State University, Leninskie Gory, 119991 Moscow, Russia*
[6]*University of Erlangen-Nürnberg, Staudtstraße 7/B2, 91058 Erlangen, Germany*
[*]*felix.just@mpl.mpg.de*

Abstract: During the last decades, multi-pixel detectors have been developed capable of registering single photons. The newly developed hybrid photon detector camera has a remarkable property that it has not only spatial but also temporal resolution. In this work, we apply this device to the detection of non-classical light from spontaneous parametric down-conversion and use two-photon correlations for the absolute calibration of its quantum efficiency.

© 2014 Optical Society of America

OCIS codes: (040.0040) Detectors; (270.0270) Quantum optics; (150.1488) Calibration.

References and links

1. I. Rech, A. Ingargiola, R. Spinelli, I. Labanca, S. Marangoni, M. Ghioni, and S. Cova, "Optical crosstalk in single photon avalanche diode arrays: a new complete model," Opt. Express **16**, 8381–8394 (2008).
2. D. A. Kalashnikov, S. H. Tan, M. V. Chekhova, and L. A. Krivitsky, "Accessing photon bunching with a photon number resolving multi-pixel detector," Opt. Express **19**, 9352–9363 (2011).
3. M.P. Edgar, D.S. Tasca, F. Izdebski, R.E. Warburton, J. Leach, M. Agnew, G.S. Buller, R.W. Boyd, and M. J. Padgett, "Imaging high-dimensional spatial entanglement with a camera," Nat. Commun. **3**, 984 (2012).
4. W. E. Moerner and D. P. Fromm, "Methods of single-molecule fluorescence spectroscopy and microscopy," Rev. Sci. Instrum. **74**, 3597 (2003).
5. M. Hamar, J. Peřina Jr., O. Haderka, and V. Michálek,"Transverse coherence of photon pairs generated in spontaneous parametric down-conversion," Phys. Rev. A **81**, 043827 (2010).
6. D. S. Tasca, R. S. Aspden, P. A. Morris, G. Anderson, R. W. Boyd, and M. J. Padgett, "The influence of non-imaging detector design on heralded ghost-imaging and ghost-diffraction examined using a triggered ICCD camera," Opt. Express **21**, 30460–30473 (2013).
7. J. Peřina Jr., O. Haderka, V. Michálek, and M. Hamar, "Absolute detector calibration using twin beams," Opt. Lett. **37**, 2475–2477 (2012).
8. O. A. Shcherbina, G. A. Shcherbina, M. Manceau, S. Vezzoli, L. Carbone, M. De Vittorio, A. Bramati, E. Giacobino, M. V. Chekhova, and G. Leuchs, "Photon correlations for colloidal nanocrystals and their clusters," Opt. Lett. **39**, 1791–1794 (2014).

#214790 - $15.00 USD Received 26 Jun 2014; accepted 26 Jun 2014; published 11 Jul 2014

9. R. S. Aspden, D. S. Tasca, R. W. Boyd, and M. J. Padgett, "EPR-based ghost imaging using a single-photon-sensitive camera," New J. Phys. **15**, 073032 (2013).
10. L. A. Rozema, J. D. Bateman, D. H. Mahler, R. Okamoto, A. Feizpour, A. Hayat, and A. M. Steinberg, "Scalable spatial superresolution using entangled photons," Phys. Rev. Lett. **112**, 223602 (2014).
11. J. Vallerga, J. McPhate, A. Tremsin, and O. Siegmund, "Optically sensitive MCP image tube with a Medipix2 ASIC readout," Proc. SPIE **7021**, 702115 (2008).
12. V. Kraus, M. Holik, J. Jakubek, M. Kroupa, P. Soukup, and Z. Vykydal, "FITPix - fast interface for Timepix pixel detectors," J. Instrum. **6**, C01079 (2011).
13. T. Holy, J. Jakubek, S. Pospisil, J. Uher, D. Vavrik, and Z. Vykydal, "Data acquisition and processing software package for Medipix2," Nucl. Instrum. Methods Phys. Res. A **563**, 254–258 (2006).
14. J. Vallerga, A. Tremsin, T. Michel, J. Alozy, T. Tick, and M. Campbell, "Optical MCP image tube with a quad Timepix readout: initial performance characterization," J. Instrum. **9**, C05055 (2014).
15. X. Llopart, "Timepix a 65k programmable pixel readout chip for arrival time energy and photon counting measurements," Nucl. Instrum. Methods Phys. Res. A **581**, 485–494 (2007).
16. W. H. Louisell, A. Yariv, and A. Siegman, "Quantum fluctuations and noise in parametric processes. I," Phys. Rev. **124**, 1646–1654 (1961).
17. M. Ware and A. Migdall, "Single-photon detector characterization using correlated photons: the march from feasibility to metrology," J. Mod. Opt. **15**, 1549–1557 (2004).
18. D. Klyshko, "Use of two-photon light for absolute calibration of photoelectric detectors," Sov. J. Quantum Electron. **10**(9), 1112 (1980).
19. A. A. Malygin, A. N. Penin, and A. V. Sergienko, "Efficient generator of a two photon field of visible radiation," Sov. J. Quantum Electron. **11**, 939–941 (1981).
20. AAbsolute efficiency and time-response measurement of single-photon detectors. A. Malygin, A. N. Penin, and A. V. Sergienko, "Absolute calibration of the sensitivity of photodetectors using a biphotonic field," Pis'ma Zh. Eskp. Teor. Fiz. **33**(10), 477–480 (1981).
21. D. C. Burnham and D. L. Weinberg, "Observation of simultaneity in parametric production of optical photon pairs," Phys. Rev. Lett. **25**, 84–87 (1970)
22. G. O. Rytikov and M. V. Chekhova, "Detection of two-mode compression and degree of entanglement in continuous variables in parametric scattering of light," JETP **106**, 923–932 (2008).
23. P. G. Kwiat, A. M. Steinberg, R. Y. Chiao, P. H. Eberhard, and M. D. Petroff, "Absolute efficiency and time-response measurement of single-photon detectors," Appl. Opt. **33**, 1844–1853 (1994).
24. V. Gromov, M. van Beuzekom, R. Kluit, F. Zappon, V. Zivkovic, M. Campbell, T. Poikela, X. Llopart, C. Brezina, K. Desch, X. Fang, and A. Kruth, "Development and applications of the Timepix3 readout chip," PoS (Vertex 2011) **046** (2011).

1. Introduction

During the last three decades, several types of multi-pixel detectors have been developed, capable of registering single photons. These include intensified CCD (ICCD) cameras relying on amplification via micro channel plates, electron-multiplied CCD (EMCCD) cameras, and simpler devices, called multi-pixel photon counters, or solid-state photomultipliers. In the latter, there is no possibility of addressing particular pixels as the signals from different pixels are joined together at the output. As a result, due to the cross-talk between the pixels, false multi-photon correlations arise [1], which complicate the extraction of useful information [2]. EMCCD and ICCD cameras are free from this drawback as they enable addressing particular pixels and, although they also manifest cross-talk, one can eliminate its influence by combining pixels into 'clusters' or choosing well separated pixels. With such cameras, despite their relatively low quantum efficiencies, photon counting is a standard technique [3] and ICCD and EMCCD cameras are traditionally used for imaging single-photon emitters such as molecules [4]. They are also applied to the measurement of intensity correlation functions for two-photon light emitted via spontaneous parametric down-conversion (SPDC) [5] and ghost imaging based on this effect [6]. Using SPDC radiation, the quantum efficiency of an ICCD camera was calibrated [7] by means of a fit to the measured correlation functions. Recently, an ICCD camera was also used for spatially resolved characterization of single-photon emitters and their clusters [8]. A huge disadvantage of ICCD cameras (and even more in the case of EMCCDs) for correlation measurements and therefore coincident detection is the necessity for a long measurement

#214790 - $15.00 USD Received 26 Jun 2014; accepted 26 Jun 2014; published 11 Jul 2014
(C) 2014 OSA

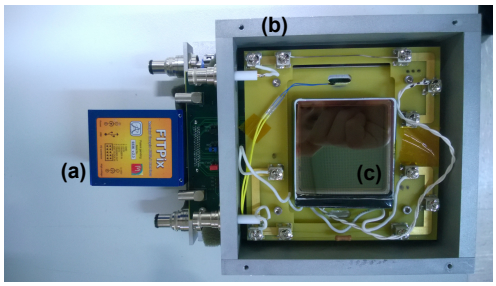

Fig. 1. A photograph of the hybrid photon detector. (a) read-out electronics, (b) PCB board with housing, (c) the tube.

time. Even though ICCD cameras can be gated within time windows as short as a few ns, usually a whole frame can reveal only a single coincidence event. Moreover, the readout times of such devices are usually much longer than the gating which additionally slows down the data acquisition significantly.

The new hybrid photon detector (HPD) can measure not only the position of an incident photon but also its time of arrival. Each individual pixel of the camera matrix is capable of tracking the point in time at which it was triggered by a photon. Even though it can only do so once per frame in the present configuration, many correlation measurement schemes including the characterisation of single photon emitters [8], ghost imaging [9], and superresolution applications [10] might be significantly improved by using this device. In contrast to other detectors of this kind, each pixel can measure events individually at the same time. Furthermore, one can even go one step further and think of more sophisticated correlation measurement schemes in the future, which might lift the once-per-frame constraint entirely. In this work we perform the first coincidence measurements with such a detector. We apply this camera to the detection of non-classical light from SPDC and use two-photon correlations for the absolute calibration of its quantum efficiency.

2. The hybrid photon detector

The hybrid photon detector is a first-of-its-kind device which provides a high temporal and spatial resolution for the detection of single photons in the optical range. The proof-of-principle experiments were carried out by J. Vallerga et al. at the Space-Science-Laboratory in Berkeley [11]. It was further developed by the Medipix collaboration and fabricated by Photonis Inc. (Photonis USA Inc., 6170 Research Road, Suite 208, TX-75033 Frisco, USA). The detector control and read-out (FitPix) was developed at the IAEP in Prague [12]. For the data acquisition the Pixelman software [13] was conceived. Depending on the mode of operation the spatial resolution can be as good as 6 µm; the timing resolution can be $\approx$ 10 ns for a single pixel. The high spatial resolution can be achieved due to the ability of the Timepix to compute the geometric centre of a charge cloud up to an accuracy that well exceeds the limits imposed by the pixel size [14]. Since this method requires a different mode of operation of the Timepix, it was not used for the experiments reported here. A photograph is shown in Fig. 1 and a more detailed description of the HPD prototype we used in our experiment can be found in [14].

The HPD consists of the read-out electronics (a), a printed circuit board (PCB) with housing (b) and the tube (c). The structure and functionality of the HPD tube is illustrated in Fig. 2.

At the top, there is an optically transparent window coated with a bi-alkali photocathode deposited in-house by Photonis USA on the input square window. The size of the cathode (53 mm x 53 mm) is much larger than that of the chip so that the extent does not affect the performance

#214790 - $15.00 USD Received 26 Jun 2014; accepted 26 Jun 2014; published 11 Jul 2014
(C) 2014 OSA

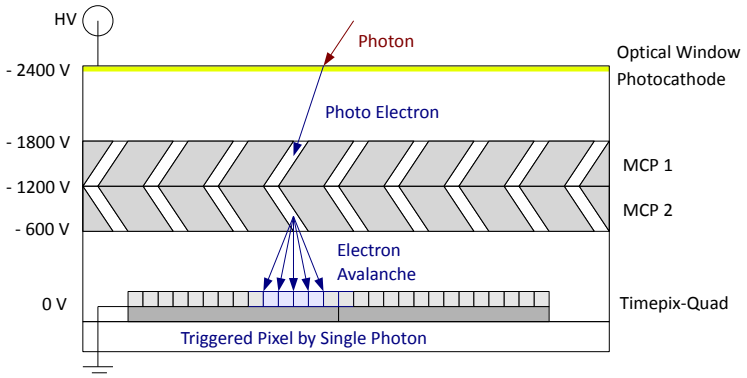

Fig. 2. A schematic cut through the HPD tube.

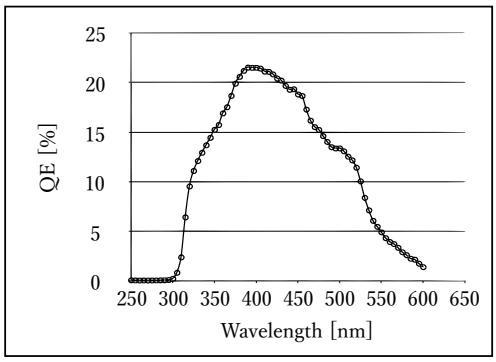

Fig. 3. Quantum efficiency of the photo cathode (measured by Photonis Inc.).

of the HPD. Located 4 mm beneath the window are two microchannel-plates (MCPs) stacked onto each other. Underneath the MCPs, four Timepix application specific circuits (ASICs) [15] are located in a 2x2 layout. During regular operation the cathode is at nominal voltage of -2.4 kV. The top surface of the upper MCP is at -1.8 kV. Both MCPs have a voltage gradient of 600 V across them. Hence, the bottom surface of the lower MCP is at -600 V. The Timepix-ASIC is grounded and the tube is at a vacuum pressure of about 10^{-10} mbar.

Initially Timepix detector – a hybrid active pixel detector – was developed for coloured X-ray imaging. 'Hybrid' in this context means, that unlike in a CCD, the signal processing and the sensitive volume of the detector are made from two different bulks of material. The ASIC, which is responsible for the signal processing, and the sensor material are fabricated separately and afterwards connected to each other by bump-bonds. This allows to use the same ASIC with different sensor materials depending on the particular application. For X-ray imaging, a sensor with high absorption efficiency is desirable and cadmium-telluride can be used. For neutron imaging a silicon sensor with a Litium converter can be used. For the detection of optical photons a thin photocathode has to be used and the photoelectron needs to be amplified in order to produce a signal in the Timepix-ASIC. Since the photocathode and the Timepix-ASIC are separated from each other like in a hybrid active pixel detector, the name 'hybrid photon

#214790 - $15.00 USD Received 26 Jun 2014; accepted 26 Jun 2014; published 11 Jul 2014
(C) 2014 OSA

detector' is used.

At the photocathode, an optical photon is absorbed and a photo-electron is emitted. A (non-absolute) calibration curve of the photocathode can be found in Fig. 3. Due to the voltage difference the photo-electron is pulled towards the MCP. The MCPs (also manufactured by Photonis) are thin (1 mm) pieces of glass with co-aligned pores of 25 μm diameter and a pore bias of 16 degrees. In the HPD, two MPCs are used in a 'chevron' configuration which is used to avoid ion-feedback. A photo-electron entering the pore will produce multiple secondary electrons due to its kinetic energy when it hits the wall of the pore. This process happens many times within the pore which leads to electron multiplication. From one single photo-electron about 10^6 electrons are produced in this process by the two consecutive MCPs. This avalanche of secondary electrons is collected on the input electrodes of the pixels of the Timepix-ASIC.

An important factor affecting the performance of the device is the ratio between the area of the holes and the non-sensitive parts of the MCP. If a photo-electron does not fall into an MCP hole but onto the non-sensitive area, it is not detected. The geometry of the MCP is a hexogonal lattice of 25 μm round pores with the pore centers separated by 32 μm. From this we obtain a probability of 0.55 for an electron to hit a pore.

The Timepix-ASIC has 256 x 256 pixel with a pixel size of 55 μm. Every pixel contains its own amplifier and logical unit which coverts the collected charge into a voltage pulse and also includes a counter. The voltage pulse is discriminated against a global threshold in every pixel. The threshold corresponds to about 1000 electrons. The Timepix can be operated in three different modes. In the 'time-over-threshold' mode, the Timepix returns how much charge was collected in every pixel by the number of digital clock pulses that are counted during the time when the voltage pulse is over the threshold. The second way the camera can be operated in is the counting mode in which each event above the detection threshold increases the counter of a hit pixel. Finally, in the 'time-of-arrival' mode (ToA) the detector provides a timing information for every pixel by the amount of digital clock pulses from the first time the voltage pulse goes over the threshold until the frame ends (Fig. 4). Since we are interested in correlation measurements the only mode of operation considered in this paper will be the ToA mode.

3. Absolute calibration

In conventional calibration methods, the quantum efficiency of the detector under test (DUT) is obtained via comparison with a reference detector. The non-classical state of light emitted by SPDC [16] allows for a reference free, or absolute, method to calibrate the quantum efficiency of a photon counting detector [17]. Such a scheme was proposed as a method for calibration by Klyshko [18] (and hence is often referred to as the *Klyshko* method), and later implemented in experiment [19, 20]. It should be noted, however, that the first measurement of quantum efficiency using SPDC was performed by Burnham and Weinberg [21]. The idea is to utilise the photon-number correlations in SPDC. The Hamiltonian of the process is $\hat{H} \propto \int \mathrm{d}\mathbf{k}_s \mathrm{d}\mathbf{k}_i \hat{a}^\dagger_{\mathbf{k}_s} \hat{b}^\dagger_{\mathbf{k}_i} +$ h.c., where $\hat{a}^\dagger_{\mathbf{k}_s}$ and $\hat{b}^\dagger_{\mathbf{k}_i}$ are the creation operators for photons with wavevectors $\mathbf{k}_{s,i}$ in the signal (s) and idler (i) modes respectively. The quantum state of the emitted photons is obtained by applying the time evolution $|\psi(t)\rangle = \mathrm{e}^{-\frac{i}{\hbar}\hat{H}t}|0\rangle$ and expanding it to the first order only. In other words, we consider the low-gain regime where photons are exclusively created in pairs, $|\psi\rangle = |0\rangle + c|1\rangle_{\mathbf{k}_s}|1\rangle_{\mathbf{k}_i}$, with $|c| \ll 1$. Therefore, from detecting the signal photon, one can infer with absolute certainty that a corresponding photon has to be present in the idler arm.

Let us assume the DUT is exposed to the signal radiation while a second detector, from here on referred to as trigger detector, is placed in the idler arm of an SPDC source. The numbers of

#214790 - $15.00 USD Received 26 Jun 2014; accepted 26 Jun 2014; published 11 Jul 2014
(C) 2014 OSA

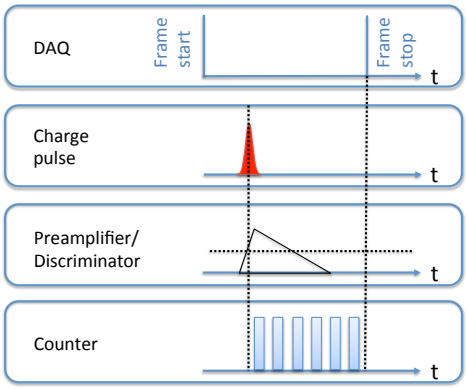

Fig. 4. The operation of the Timepix in the 'time-of-arrival' (ToA) mode. After the charge pulse is amplified and converted to a voltage pulse, it is discriminated against a threshold level. The time-of-arrival is the number of clock counts between the first time the voltage pulse rises over the threshold and the end of the frame and thus the number of clock counts until the frame ends.

counts during a certain time interval are

$$\begin{aligned} N_{\mathrm{DUT}} &= \eta_{\mathrm{DUT}} N, \\ N_{\mathrm{trigger}} &= \eta_{\mathrm{trigger}} N, \end{aligned} \tag{1}$$

where η_{DUT} and η_{trigger} are the quantum efficiencies of the two detectors and N is the number of photon pairs emitted by the source in the said time interval. Accordingly, the number of coincidence events is

$$N_{\mathrm{coinc}} = \eta_{\mathrm{DUT}} \eta_{\mathrm{trigger}} N. \tag{2}$$

For the quantum efficiency of the DUT it follows directly that

$$\eta_{\mathrm{DUT}} = \frac{N_{\mathrm{coinc}}}{N_{\mathrm{trigger}}}. \tag{3}$$

Using coincidence measurements, we are thus able to ascertain η_{DUT} independently of the quantum efficiency of an imperfect trigger detector or any reference whatsoever.

One crucial remark to this method however is that Eq. (3) does not strictly describe the quantum efficiency of the DUT alone, but rather the complete DUT-arm of the setup, i.e., the whole channel starting from the crystal until the detection including any elements in between which could cause losses of any kind [17]. In practice that means one should include the lowest amount of optical elements in the DUT channel possible Any losses that are unavoidable should be characterised thoroughly and taken into account. Fortunately, one of the advantages of the scheme utilising an SPDC source is that the spectral selection can be performed in the trigger channel and thus will not affect the measurement.

#214790 - $15.00 USD Received 26 Jun 2014; accepted 26 Jun 2014; published 11 Jul 2014
(C) 2014 OSA

Another issue arises from the fact that SPCD photons are emitted at a certain angular width. The spread of the emission angle is due to the transverse wave vector components of the pump, the width of the phasematching function (which is given by the length of the nonlinear crystal), and the selected frequency bandwidth [17]. In order to avoid events in the trigger channel which have no corresponding counterpart in the DUT and hence would lead to an artificial decrease of η_{DUT} in Eq. (3), one has to make sure that the angular acceptance of the DUT is greater than that of the trigger detector. Similar arguments, of course, hold for the spectral width.

Finally one also has to take into account that there are always some accidental coincidences, which originate from the overlapping of photon pairs and have to be subtracted from the total number of coincidence events. Those pairs can originate from stray light, overlapping of pairs from the SPDC process or the dark noise of either device. Consequently we used a modified Eq. (3) to obtain the actual quantum efficiency under laboratory conditions [23]:

$$\eta_{\mathrm{DUT}} = \frac{N_{\mathrm{coinc}} - N_{\mathrm{acc}}}{N_{\mathrm{trigger}} - N_{\mathrm{dark}}}. \tag{4}$$

Here N_{acc} denotes the number of accidental events and N_{dark} are the dark counts of the trigger detector during the measurement time.

4. Setup

4.1. Optical setup

A sketch of the optical setup is given in Fig. 5. In order to create the photon pairs, a β-Barium Borate (BBO) crystal of 5mm length was pumped by a cw diode laser operating at a wavelength of 405nm. The crystal was anti-reflection coated for the signal wavelength. The pump power was about 1.5mW and the beam was focused down to a waist of 100 µm to provide angular and spectral widths for the SPDC process, suitable for our experimental conditions. At first, the phasematching was chosen such that the photons in the camera channel were emitted at 560nm and under an angle of 4°, while the trigger photons were emitted at 10° with a wavelength of 1463nm. To ensure detection of correlated photon pairs a bandpass filter of 12nm width was placed in the trigger channel. The wavelengths could be tuned by replacing the filter and adjusting the angle between the optic axis of the crystal and the pump beam accordingly to preserve the alignment. As previously mentioned, it is necessary that the trigger detector is exposed to either a more limited or to exactly the same angular spectrum corresponding to the spectrum in the DUT channel. An iris placed in the far field ensures this condition to be fulfilled. Due to the rather large sensitive area of the detector, we placed the HPD in a box to shield it from ambient light. The trigger photons were then fibre coupled to a single mode fibre and detected by a Scontel superconducting nano-wire detector.

In the last section we stated that for the calibration it is beneficial to do all filtering in the trigger channel, since losses there will not affect the quantum efficiency of the DUT. Nevertheless a dichroic mirror (DM450) and a colour glass filter (CG495) had to be included in the DUT arm. Even though the pump was spatially separated from the signal, fluorescence and scattered light from the pump originating from the crystal could easily saturate the camera because their spectrum almost coincided with the maximum sensitivity range of the HPD photocathode.

4.2. Electronics and data acquisition

To obtain the quantum efficiency from Eq. (3), the number of coincidences between the trigger detector and the DUT has to be determined. To achieve this the following scheme was realized.

The HPD delivers the data not continuously but in frames. Therefore, we synchronized the laser and the HPD data acquisition by a signal generator and a gate to reduce both the dark

#214790 - $15.00 USD Received 26 Jun 2014; accepted 26 Jun 2014; published 11 Jul 2014
(C) 2014 OSA

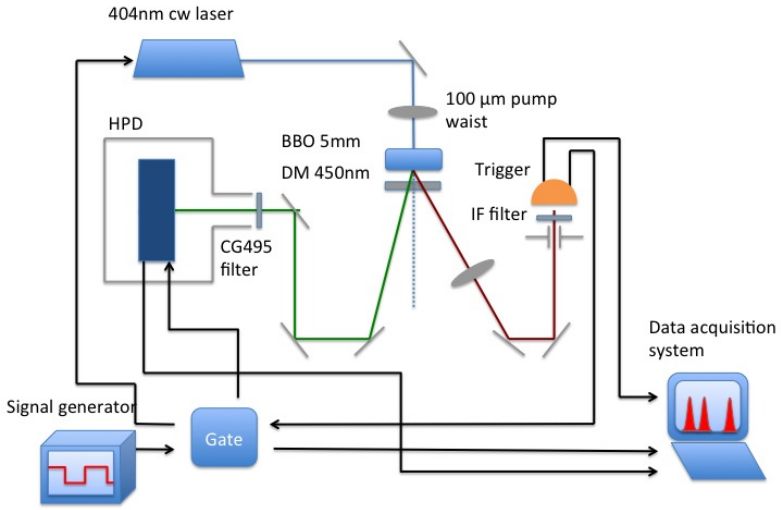

Fig. 5. Optical setup.

noise and the overall photon flux on the camera. A scheme of the electronics is shown in Fig. 6. The signal generator delivered the 'start' signal to the gate at a fixed rate. Its output signal (TTL) was then split into the 'start' signal for the HPD and the 'start' signal for the laser. The 'stop' signal on the gate came from the trigger detector. We discriminated the output of the trigger detector and then sent a TTL signal to the gate. This signal was delayed by 1.2 µs. Upon the arrival of the 'stop' signal, both the frame and the laser were stopped. After that the data was read out from the Timepix chips ($\approx$ 200 ms). As in the ToA mode the time until the frame end was obtained for each pixel individually, we saw coincident events between both detectors at a particular ToA, corresponding to the delay between the trigger detector and the frame end in the HPD. The circuit diagram and the logical scheme are depicted in Fig. 6.

5. Data analysis and results

5.1. Data analysis

Figure 7(a) shows the spatial distribution of detected photon events for one typical frame. Every single photon event is detected as a cluster of multiple triggered pixels ($\approx$ 5 on average) on the matrix. This is caused by the electron multiplication due to electron emission from the walls of the MCP pores. When the electrons are emitted from the wall they usually have some transverse momentum. The number of electrons after amplification is large (10^6) compared to the threshold of a pixel (10^3). Since a small fraction of the electrons is enough to trigger one pixel and because of their transverse spread, several pixels can be excited by a single event. To obtain the timing information for a cluster we averaged over the time-stamps (ToA) of its pixels. The number of coincidences between both detectors during a complete measurement cycle was obtained by the integration over all frames. Accidental coincidence events manifest themselves as a background in the histogram. The time distribution of coincidence events (number of clusters plotted versus ToA) for a single measurement is shown in Fig. 8(a). One can clearly distinguish the peak of coincident events from the background of accidental coincidences. The

#214790 - $15.00 USD Received 26 Jun 2014; accepted 26 Jun 2014; published 11 Jul 2014
(C) 2014 OSA

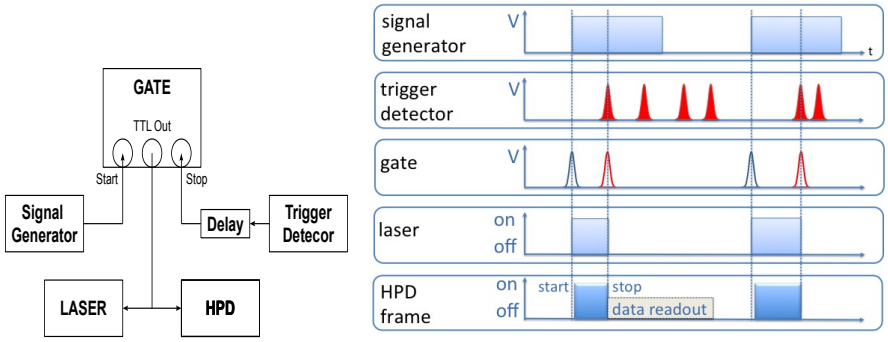

(a) (b)

Fig. 6. (a) Diagram circuit for the coincidence measurement. (b) Scheme of coincidence readout

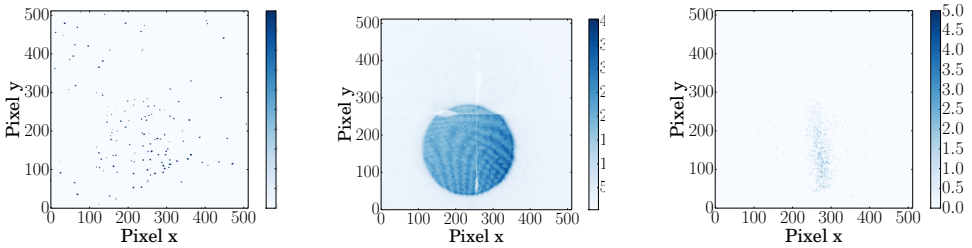

(a) Single Frame (b) All Frames (c) Coincident Events

Fig. 7. (a) Examples of a single frame, (b) the result of the integration over all frames for one measurement cycle, and (c) the post-selected events corresponding to the coincidence peak. The colour bar indicates the number of events.

level of accidental coincidences, given by the background of the coincidence distribution, was determined by taking the average of the distribution, excluding its peak. The peak is centered at about 1275 ns which corresponds to the delay that we introduced into the system. Please note that the abscissae are in clock cycles of 21 ns each (corresponding to a ToA clock cycle frequency of 48 MHz) until the end of the frame. Therefore, events with larger ToA values are actually earlier than events close to the origin (the frame end).

An image of all events integrated over the complete measurement is given in Fig. 7(b). Here we observe the whole SPDC spectrum (all possible phasematching processes). Its circular shape is governed by the aperture of the box that was used to protect the HPD from ambient light. Figure 7(c) shows only events coincident with the trigger. The line that is visible is actually part of an arc of the SPDC radiation (usually emitted along a cone) corresponding to the wavelength range selected by the filter in the trigger arm.

Since the trigger detector provides a rate in counts per second while from the coincidence time distribution the number of counts is obtained, we had to read-out the total acquisition time for the HPD. In Fig. 8(b) the distribution of frame-times for a complete run is shown. The integral of this distribution was used as the total acquisition time. The dark noise of the trigger detector was recorded during the time intervals when the laser was off.

#214790 - $15.00 USD Received 26 Jun 2014; accepted 26 Jun 2014; published 11 Jul 2014
(C) 2014 OSA

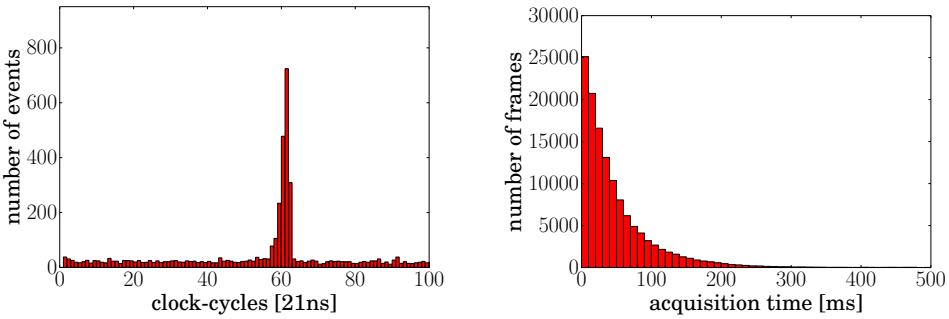

(a) ToA distribution of coincidences

(b) Acquisition time histogram

Fig. 8. (a) Example of an integrated ToA spectrum of one complete measurement cycle for a single wavelength. The coincident peak appears at 20 clock cycles (=1275 ns). (b) Example of a typical acquisition time histogram.

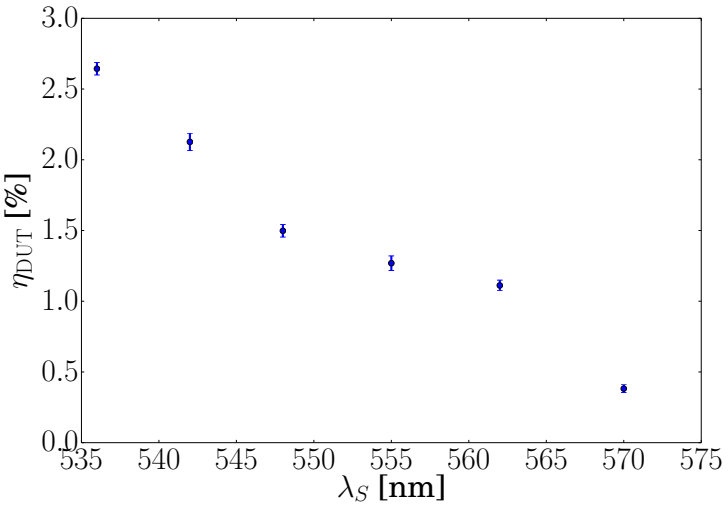

Fig. 9. Quantum efficiency as a function of the wavelength at 2400 V MCP stack voltage.

5.2. Results

Figure 9 shows the quantum efficiency measured as a function of the wavelength. As expected (see Fig. 3), the quantum efficiency increases towards shorter wavelengths. We found the error bars by assuming a Poisson distribution for the count rates and performing the usual Gaussian error propagation. The main contribution to the errors stems from the fluctuations in the dark counts of the trigger detector. Those were assumed to be Poissonian distributed as well. However during some of the measurements we observed a minor systematic drift of the dark count rate and hence the distribution might have non-random contributions which in turn could lead to a slight underestimation of errors. Compared to the quantum efficiency of the photocathode,

#214790 - $15.00 USD Received 26 Jun 2014; accepted 26 Jun 2014; published 11 Jul 2014
(C) 2014 OSA

the absolute quantum efficiency of the HPD is about a factor of 2 lower. As explained in Sec. 2 the open area ratio of the MCPs is about 50%. This corresponds to the ratio between the results of the absolute calibration and the calibration of the photocathode only. Notwithstanding this factor of 2, within the spectral range of our measurements, the quantum efficiency curve follows quite nicely that of the specifications of the photocathode.

The background (stray light and dark counts) of the HPD was also characterised by performing one measurement with a blocked pump laser. Over the whole chip we observed a background of 165 Hz . Under our lab conditions (ambient light, trigger detector noise ect.) this led to an accidental coincidence rate caused by the HPD dark rate of about 0.005 Hz. For comparison, the trigger rates were typically around 20 Hz and the raw coincidence rates ranged from 0.5 Hz and 1.5 Hz depending on wavelength and MCP voltage (see below).

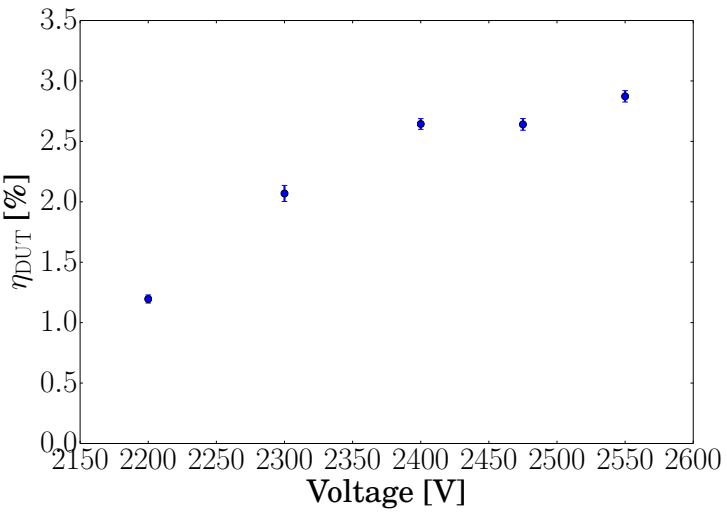

Fig. 10. Quantum efficiency as a function of the MCP stack voltage at 536 nm..

One parameter which directly affects the quantum efficiency of the HPD is the voltage applied to the tube, therefore we also measured η_{DUT} at a fixed wavelength of 536 nm as a function of the voltage. The amplification in the MCP depends directly on the kinetic energy of the electrons involved. At higher voltages the electrons in the pores will experience a stronger acceleration and thus create a bigger avalanche which in turn is more likely to be detected by the Timepix chips. These considerations make it apparent that the MCP gain and thus the quantum efficiency of the tube increases with the voltage. The dependence of η on the voltage is illustrated in Fig. 10. We can see a saturation of the quantum efficiency at high voltages. The reason behind this is that at sufficiently high voltages (and thus amplifications) every electron emitted by the photocathode will result in at least one detection event. The results can be found in agreement with the previous measurements [14]. In Table 1 the results for the calibration at different wavelengths are summarised. Please note that these values are subject to losses due to the absorption in the dichroic mirror and the colour glass (both $\approx 10\%$). Column three of Table 1 gives the quantum efficiency corrected for the filter transmissions.

#214790 - $15.00 USD Received 26 Jun 2014; accepted 26 Jun 2014; published 11 Jul 2014
(C) 2014 OSA

Table 1. Results of the absolute calibration measurements

wavelength [nm]	η_{DUT} [%]	$\eta_{\mathrm{DUT}}^{\mathrm{corrected}}$ [%]	$\delta\eta_{\mathrm{DUT}}$ [%]
536	2.64	3.19	0.04
542	2.13	2.59	0.06
548	1.50	2.05	0.04
555	1.27	1.68	0.05
562	1.11	1.36	0.04
570	0.38	0.48	0.03

6. Conclusion

We successfully implemented the first measurements on nonclassical light with the HPD operating in the single-photon regime. An SPDC source has been used to perform the absolute calibration measurement of the HPD from 535 nm to 570 nm. Furthermore we investigated the effect of the voltage applied to the MCPs on the quantum efficiency. Those first measurements demonstrate the HPD's capability for coincidence acquisition. This opens the door for correlation measurements in general and thus many of the standard applications in quantum optics. We believe that in the future, the HPD's unique capabilities namely the availability of both space and time resolution have the potential to improve the existing experiments or even allow new ones. The main drawback is the long readout time of the chip and the resulting low frame rate. This however will be remedied with the next generation of the Timepix-ASIC [24] which will provide not only higher temporal resolution but also continuous data output.

Acknowledgments

We are very grateful to the Medipix collaboration for the development of the HPD. This work was supported in part by ERA-Net.RUS (project Nanoquint).

IV.1.2 Publication: Three dimensional photograph of electron tracks through a plastic scintillator

The publication "Three dimensional photograph of electron tracks through a plastic scintillator" (accepted for publication in Eur. Phys. J. C (2014)) covers the following issues:

- Introduction to the idea of tracking by scintillation light.
- Design and implementation of an optical system for particle tracking by scintillation light.
- Acquisition and analysis of data obtained with GeV electrons.
- Successful reconstruction of three dimensional trajectories from two dimensional data.
- Examination of the achieved position resolution.

My own contributions to the publication:

- Idea for the technique and the experiment.
- Experimental design.
- Supervision of Patrick Hufschmidt for his bachelor thesis (preparation and adjustment of the optical setup).
- Experiment preparation and data acquisition at the DESY beamline.
- Data analysis (Cleaning of raw data, frame analysis, track reconstruction, evaluation of the position resolution, simulations).
- Manuscript writing (corresponding author).

Contributions of the co-authors to the publication (in particular Patrick Hufschmidt and Timur Iskhakov):

- Preparation and adjustment of the optical setup.
- Contributions to data analysis in discussions.
- Contributions to manuscript writing.

Eur. Phys. J. C manuscript No.
(will be inserted by the editor)

Three dimensional photograph of electron tracks through a plastic scintillator

Mykhaylo Filipenko[a,1], Timur Iskhakov[2], Patrick Hufschmidt[1], Gisela Anton[1], Michael Campbell[4], Thomas Gleixner[1], Gerd Leuchs[2], Timo Tick[4], John Vallerga[3], Michael Wagenpfeil[1], and Thilo Michel[1]

[1]University of Erlangen-Nuremberg: Erlangen Centre for Astroparticle Physics, Erwin-Rommel-Straße 1, 91058 Erlangen, Germany
[2]Max-Planck Institute for the Science of Light, Günther-Scharowsky-Straße 1/Bau 24, 91058 Erlangen, Germany
[3]Experimental Astrophysics Group, Space Science Laboratory, University of California, Berkeley, CA-94720, USA
[4]European Organization for Nuclear Research, CERN, CH-1211, Geneve 23, Switzerland

Received: date / Accepted: date

Abstract The reconstruction of particle trajectories makes it possible to distinguish between different types of charged particles. In high-energy physics, where trajectories are rather long (several meters), large size trackers must be used to achieve sufficient position resolution. However, in low-background experiments like the search for neutrinoless double beta decay tracks are rather short (some mm to several cm, depending on the detector in use) and three dimensional trajectories could only be resolved in gaseous time-projection chambers so far. For detectors of large volume of around one cubic meter (large in the scope of neutrinoless double beta search) and therefore large drift distances (several decimeters to one meter), this technique is limited by diffusion and repulsion of charge carriers. In this work we present a "proof-of-principle" experiment for a method of three dimensional tracking of charged particles by scintillation light: We used a setup consisting of a scintillator, mirrors, lenses and a novel imaging device (the hybrid photon detector) in order to image two projections of electron tracks through the scintillator. We took data at the T-24 beamline at DESY with relativistic electrons with a kinetic energy of 5 GeV and from this data successfully reconstructed their three dimensional propagation path in the scintillator. With our setup we achieved a position resolution in the range of 170 µm to 248 µm.

1 Introduction

Since the beginning of the 20th century tracking detectors have played an outstanding role for discoveries in experimental particle and nuclear physics. After the first cloud chamber was built by Charles Wilson in 1911, it was possible to observe tracks of charged particles [1]. By applying a magnetic field and analyzing the trajectories one was able to distinguish between electrons and positrons which was discovered by a cloud chamber in 1932 [2]. With technological progress ongoing the cloud chamber was replaced with the bubble chamber [1] and the spark or wire chamber [3] which allowed higher event rates, better position resolution and an automated electrical data read-out. This technology was developed further to the gas-filled multi-wire proportional chamber [3] and the gas-filled time-projection chamber [4] which made it possible to reconstruct trajectories in three dimensions.

After the advancement in semiconductor technology silicon strip detectors [5, 6] were developed and used for tracking applications. During the past ten years hybrid active pixelated semiconductor detectors are on the rise and expected to achieve a position resolution down to several µm for vertex tracking applications [7, 8]. Besides these technologies, nuclear emulsions play an important role as a tracking detector in OPERA [9] and scintillating fiber trackers are discussed as a replacement for the downstream tracker in the LHCb upgrade [10].

Although with modern tracking detectors, a very good position resolution (down to several micrometers) can be achieved for the detection of high energetic particles ($E_{kin} >$ 1 GeV), in the case low-background experiments like the direct detection of dark matter or the neutrinoless double beta decay the same technologies cannot be used in the usual manner due to the specific requirements of these experiments. Since the main motivation behind this work is the search for neutrinoless double beta decay [11], the requirements for this specific research goal are discussed below:

In this hypothetical decay two electrons are supposed to be emitted from a nucleus with a sum kinetic energy ranging from about 0.9 MeV to about 4.8 MeV, depending on the nuclide of choice. In a neuntrinoless double beta decay the

[a]e-mail: mykhaylo.filipenko@physik.uni-erlangen.de

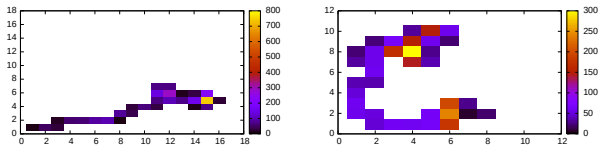

(a) (b)

Fig. 1: Example of a simulated single electron (a) and neutrinoless double beta decay event (b) with 2.8 MeV kinetic energy propagating through a cadmium-telluride sensor as detected with a Timepix-ASIC. The size of a pixel is 110 µm. The length of a track is ≈ 1.5 mm. The color denotes the energy deposition per pixel in keV.

energy of both electrons has to be measured precisely to distinguish it from the neutrino-accompanied double beta decay[1]. Usually in such experiments the decaying material is the sensitive detector volume at the same time because of two reasons: a) The expected event rate is very low (smaller than 1 event per 100 kg of enriched material per year [12]) and therefore a large mass is required (with thin foils it is hard to achieve a high mass). b) Electrons with energies on the MeV scale are easily scattered and therefore lose a significant part of their energy already on very small distances. Therefore, it is convenient to detect the electrons at their point of emission to avoid these losses.

In neutrinoless double beta decay experiments the main problem is the reduction of background (like beta decay events, Compton electrons, photoelectrons, α-particles) which can produce false positive events. Tracking might be a valuable tool to identify such events and sort them out since the topological structure of the trajectory of the two decay electrons (for a neutrinoless double beta decay) is different from other ionizing radiation. On Fig. 1 a simulated electron with a kinetic energy of 2.8 MeV (Q-value of ^{116}Cd, a neutrinoless double beta nuclide) and a simulated neutrinoless double beta event as could be measured in a cadmium-telluride Timepix detector are shown: In this case these two event types can be distinguished by eye but also in more sophisticated cases methods like artificial neural networks can be used to identify different type of ionizing radiation [14–16].

The CSDA range (average track length) of electrons with a low kinetic energy (0.9 MeV to 4.8 MeV) in solid or liquid materials that could be used for a neutrinoless double beta experiment ranges from several millimeters to some centimeters. As a consequence, they are usually completely stopped within one detector segment, such as one pixelated semiconductor sensor layer or one scintillator block and therefore a track reconstruction in the manner of vertex tracking (where the position information from several tracking planes is combined) is not possible.

Nonetheless in future, tracking in neutrinoless double beta experiments could be performed by a pixelated read-out of the ionization signal with high granularity. It means that secondary electrons which were released in a gas or semiconductor material by the primary particle are drifted in an electric field to the collecting electrodes. Conductive wires (in TPCs) or active pixel detectors (like the Timepix) collect the released electrons and generate a signal by charge collection or the induction of currents. In micro pattern gaseous detectors, the electrons are drifted towards micromegas structures or GEM-foils. The transversal coordinates perpendicular to the drift direction can be measured by using at least two read-out planes (wire planes in TPCs) or segmentation of the collecting structure in pixels. In gaseous detectors, the drift time of the electrons is measured to reconstruct the drift distance (z-coordinate) [16].

This method has the disadvantage that the position resolution is limited by the diffusion[2] of charge carriers on their way through the sensor material (gas, semiconductor). This limitation makes it difficult to obtain a sufficient position resolution in a detector with large drift distance. For common materials like liquid xenon in use for neutrinoless double beta experiments the diffusion radius (the spread of the charge cloud in the plane perpendicular to the drift direction, when it arrives in the read-out plane) is larger then the primary particle's track length after the drift through the sensitive full volume (if the drift distance exceed several cm) which makes it impossible to resolve tracks in a large sensitive volume.[3]

This work presents a different approach for the measurement of three-dimensional trajectories of charged particles. The goal is to overcome the diffusion limitation. One possible way to do so is to use the scintillation signal instead of the ionization signal. Scintillation photons are created along the track and do not diffuse on their way through the sensor from the point of origin to the plane where they are detected. One can take advantage of this fact and reconstruct the particle's 3D trajectory from multiple 2D projections of the track imaged with a pixelated single photon detector. This publication presents a "proof-of-principle" demonstration of this method. We used a plastic scintillator, basic optical components (mirrors and lenses) and the hybrid photon detector which is explained in the next subsection.

[1] During a neutrino-accompanied double beta decay, the Q-value is distributed between two electrons and two anti-neutrinos, wherefore the sum energy of the two electrons is a broad distribution from zero to the Q-value of the decay.

[2] Besides diffusion, also the repulsion of charge carriers contributes to the spread of the charge cloud on its way through the sensor. Here, we use the term diffusion as a roundup for diffusion, repulsion and other possible effects that contribute to the spread of the charge cloud on its way through the sensor to the read-out structure.

[3] Tracks from some bottom part (close enough to the read-out plane) could be resolved but not from the full volume which is the goal.

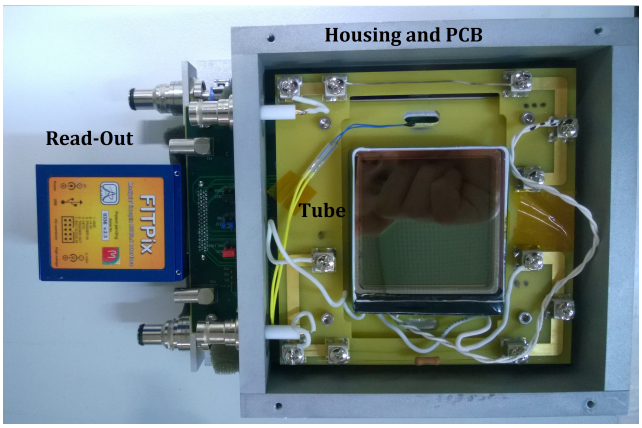

Fig. 2: A photograph of the hybrid photon detector (HPD) connected to a FitPix read-out [19].

1.1 The Hybrid Photon Detector

The hybrid photon detector (HPD) is a first-of-its-kind detector that combines high spatial and temporal resolution for the detection of single optical photons [18]. The detector's image vacuum tube consists of a bi-alkali photocathode which has its highest quantum efficiency of about 20 % in the blue/violet spectral range (390 nm). Underneath the photo-cathode there are two microchannel plates (MCPs) in a chevron configuration. Beneath those are four Timepix-ASIC [21] arranged in a 2×2 layout (512×512 pixels). The tube is sealed under a vacuum pressure of 10^{-10} mbar. Photoelectrons which are released from the photo-cathode by optical photons are multiplied in an avalanche-cascade process in the MCPs. The MCP acts as multi-channel photomultiplier. Therefore, one incident photon on the cathode results in an avalanche of about 10^5 to 10^6 electrons on the Timepix-ASIC electrodes with the MCPs retaining the information of the input location in the charge cloud centroid. The overall voltage difference between the photo-cathode and the Timepix is 2.4 kV. The Timepix-ASIC is at ground potential whereas the photo-cathode is at -2.4 kV. Because the anode is pixelated, many photons can be detected concurrently. Depending on the mode of operation the timing resolution can be as good as 10 ns and the position resolution as good as 6 µm. The sensitive area is 2.8 cm × 2.8 cm. A photograph of the detector is shown in Fig. 2. Details on the HPD can be found in [18].

One Timepix-ASIC has 256×256 pixels with a pixel pitch of 55 µm. Each pixel has its own input electrode, connected to an analog circuitry with pre-amplifier and discriminator, and a digital electronics circuitry. In each pixel the charge is collected and converted into a voltage pulse. This is done by a Krummernacher type pre-amplifier. The voltage pulse in each pixel is discriminated against a global threshold which is equivalent to approximately 1000 e^-. From this point on, the processing in each pixel is digital. It operates in three different ways but in this work only the so-called "'time-of-arrival"' (ToA) mode was employed.

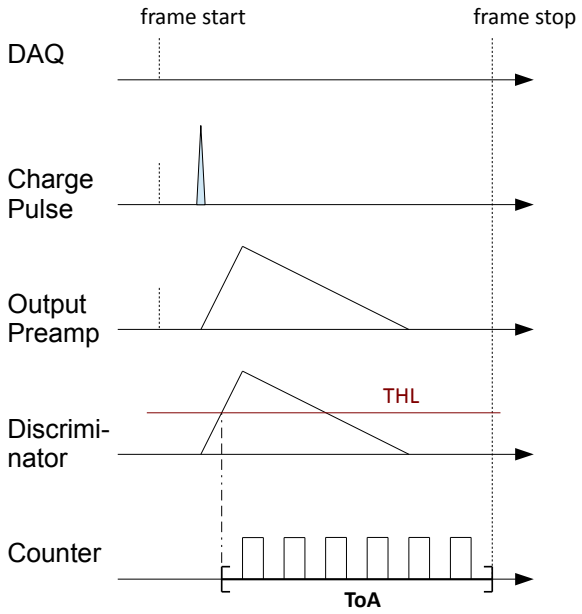

Fig. 3: The operation of the Timepix in the "time-of-arrival"' (ToA) mode. After the charge pulse is amplified and converted to a voltage pulse, it is discriminated against a threshold level (THL). The time-of-arrival is the number of clock counts between the first time the voltage pulse rises over the THL and the end of the frame.

The ToA mode is illustrated in Fig. 3. When the voltage pulse rises above the threshold a digital register starts counting clock cycles until the end of the frame. The number of counted cycles is called "'time-of-arrival"' or ToA. This way, each triggered pixel gets a time-stamp wherefore the ToA provides an absolute timing information for every pixel. A frame can have a fixed frame-time or be opened and closed by an external trigger (timing gate). The fastest possible clock frequency is about 100 MHz wherefore every counted clock cycle corresponds to about 10 ns. Details about the Timepix-ASIC can be found in [21].

2 Experimental Setup

The main idea of the experiment was to reconstruct a three-dimensional particle trajectory from multiple two-dimensional projections. When a charged particle propagates through a scintillator, scintillation photons are emitted isotropically along the track after relaxation of excited states. An optical system can be used to collect the isotropically emitted light for imaging. In the easiest possible scenario just one single lens and one detector can be used to create a two-dimensional

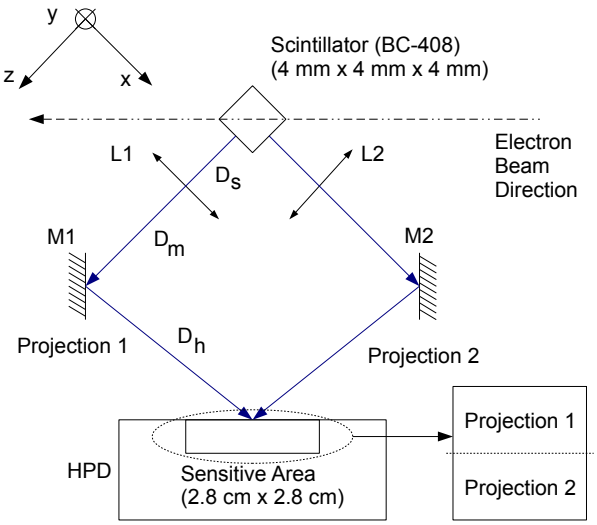

Fig. 4: Schematic view of the setup used for the measurements. It consists of a plastic scintillator, two lenses (L1, L2) and two mirrors (M1, M2) and the HPD. One projection of the electron track in the scintillator is imaged on the top half of the HPD and the other on the bottom half.

image. If the same scintillator is imaged from multiple perspectives the information can be used to reconstruct a three-dimensional trajectory.

For a proof-of-principle demonstration of this method we used a setup as illustrated on Fig. 4. A cubic plastic scintillator (Bicron BC-408) with dimensions of 4 mm $\times$ 4 mm $\times$ 4 mm was imaged from two orthogonal directions. The scintillation photons have a wavelength of about 425 nm. We used two similar Thorlabs LB1761-A bi-convex lenses made of N-BK7 with a focal length of f = 25.4 mm and a diameter of d = 25.4 mm. Two mirrors (Thorlabs BB1-E01) with a diameter of 25.4 mm were employed to adjust the optical path. One side of the scintillator was imaged on the top half of the HPD and one side on the bottom half. We adjusted the optical setup with a laser by imaging two sides of the scintillator on a paper screen held in front of the photocathode. We did not take an actual image with the camera to prevent the camera from taking any damage due to over illumination with the laser.

The distances between the optical elements were $D_s = 34$ mm, $D_m = 25$ mm and $D_h = 77$ mm. With this geometry we calculated a magnification of 3.3 and a light detection efficiency of about 1.5 % per view (perspective) per image, taking into account the geometrical acceptance, the losses in the optical elements and the absolute quantum efficiency of the HPD. Although the scheme suggests, that the angles were 45°, in the real setup the angles were about 4° off. With our geometry, the focal point spread function (or blur circle)

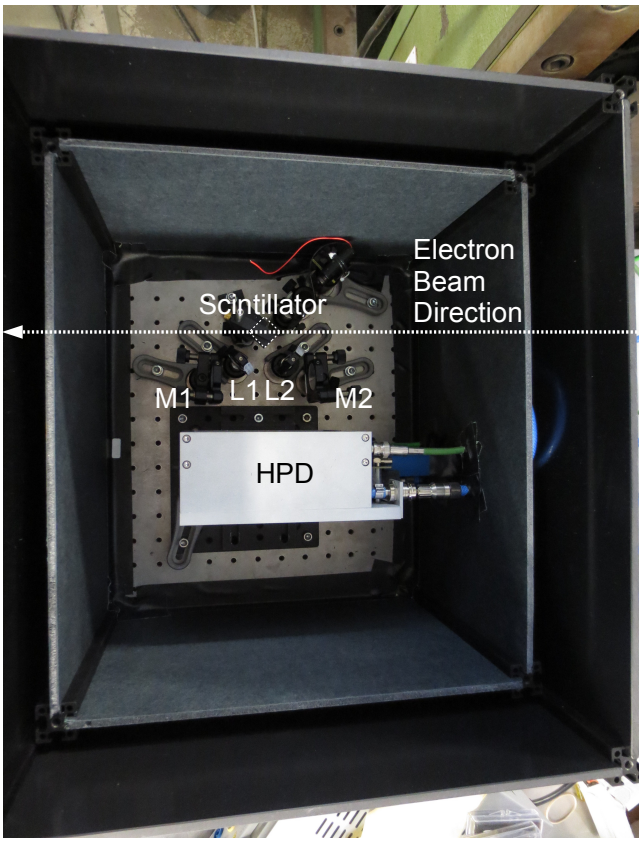

Fig. 5: A photograph of the setup used for the measurements. The detector and the optics were shielded by two layers (black plastic, dark paper board) from external optical photons. The beam direction is shown in the photograph.

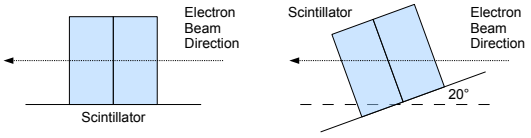

(a) (b)

Fig. 6: The direction of the electron beam through the scintillator.

σ_f at a distance d_f from the focal plane can be estimated as $\sigma_f \approx d_f$. It was calculated as described in [22]. Therefore, we expect to see sharp tracks only from an inner part of the scintillator around the focal plane (about 500 µm to each side of the focal plane).

We used two layers to shield the setup from external optical photons: The inner layer is a dark paper board from Thorlabs; the outer layer are walls made of 5 mm thick black plastic. A photograph of the setup is shown in Fig. 5. The dark rate of the HPD was 2000 counts per second, which corresponds to the intrinsic dark rate of the detector.

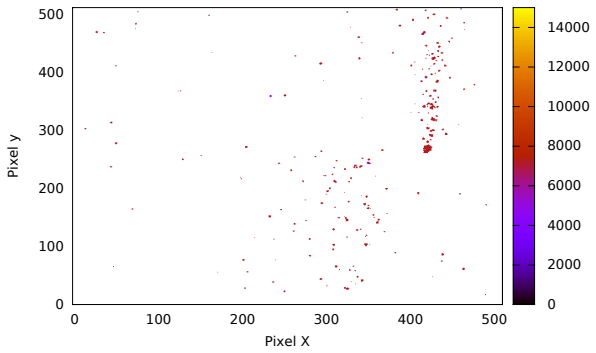

(a)

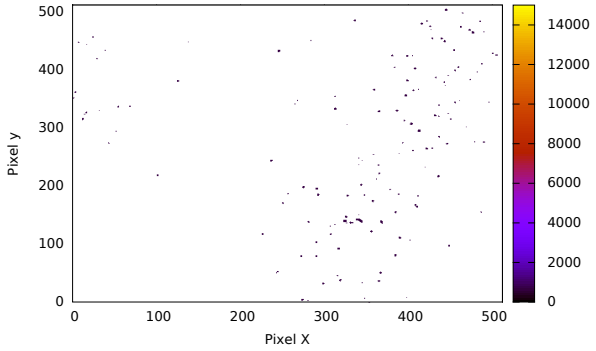

(b)

Fig. 7: Example of two typical frames: One with a track (a) and one with noise only (b). The color bar indicates the time-of-arrival measured in each triggered pixel.

We used the setup at the DESY testbeam T-24 where the scintillator was traversed by electrons with a kinetic energy of 5 GeV. Electrons of this energy can be regarded as minimal ionizing. Most of the time their trajectories through the scintillator are straight lines. Concerning the stopping power of the plastic scintillator at this energy (about 2.45 $\frac{MeV}{cm^2 g}$), we expect about 130 detected photons per view (projection) per image. The flux density of electrons was about $1000 \frac{e^-}{s \cdot cm^2}$.

The maximum digital counter value in the Timepix ToA mode is 11810 and as we used a clock of 10 MHz (100 ns per clock cycle) where the maximum frame integration time that could be used to avoid events with a maximum ToA value of 11810 (and therefore no useful timing information) was 1 ms[4]. Since the read-out speed of the data acquisition system is limited, we could only start a frame every 0.1 s. To avoid dead-time in between and increase statistics (the number of measured events), we used the trigger signal from the beam monitor (two crossed scintillator panels with a PMT attached) for the frame-stop signal in order to have a higher probability to see one electron during one frame. However, as turned out later during the data analysis, our trigger system had a malfunction during the experiment and a large part of the data has to be rejected since the ToA value of the triggered pixels was 11810. Therefore, the actual frame-time fluctuated a lot.

We took data at two different orientations between the scintillator and the beam. In first case the beam transversed the scintillator from one edge of the scintillator to the other as shown in Fig. 4 and Fig. 6a. In the second case the setup was titled by 20° with respect to the beam axis (Fig. 6b).

3 Data Analysis

A typical frame contains either a track (as in Fig. 7a) as expected or some (randomly seeming) hits (Fig. 7b). Such frames happen if the electrons path through the scintillator was out of the optical focus, or possibly the trigger gate closed without any electron passing through the scintillator. This was possible since the sensitive area of the beam monitor was larger than the cross section area of the scintillator in the setup.

Consequently, the first step was a frame selection due to the following criteria: First, we removed frames where less than 400 pixels were triggered. About 130 photons were expected per view (projection) per image and due to the electron avalanche of MCP amplification impinging on the Timepix ASIC, one photon usually triggers 3 to 5 pixels (resulting in about 780 to 1300 triggered pixels for a proper event).

Secondly, for each frame all coincident hits registered with ToA values between 1 and the maximum counter value of 11810 clock ticks were extracted. The condition for coincidence was that their ToA values differ by less than 3 clock ticks, corresponding to the time resolution of the system. These coincident hits were regarded to stem most probably from the same electron passage. Fig. 8 shows an exemplary part of ToA spectrum integrated over 44564 frames. For example, all hits at 1930 clock cycles most probably stem from one electron trajectory.

During this evaluation it turned out, that the time stamp of most events was 11810 clock counts instead of 3 clock counts as expected with the delay to the trigger. Therefore, we have to conclude an unexpected misbehavior occurred in the trigger system and the events between 1 clock cycle and 11810 clock cycles accidentally appeared at a particular time in the frame. Nevertheless, since the triggered pixels appeared in the same frame and have common ToA values, it is very likely that they belong to the same event.

As next we performed a reduced Hough-transform [23] of the frame for each projection, i.e. we calculated the angle between the x-axis and the connecting line of any two triggered pixels in each frame and sorted the angles into a his-

[4] If the ToA in the triggered pixels of an event is 11810, the pixel could have been triggered at any time between $11810 \cdot 100\,\text{ns}$ ($\approx 1\,\text{ms}$) and the end of the frame.

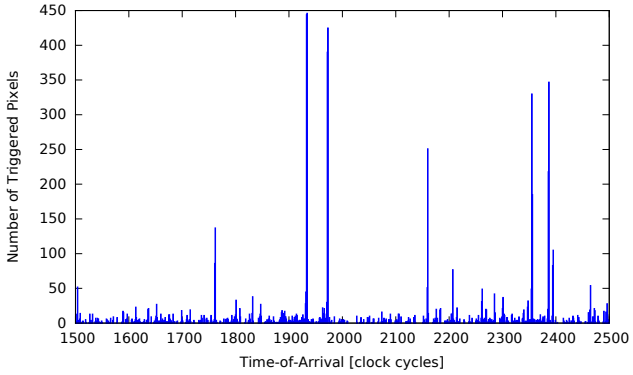

Fig. 8: Examplary part of the ToA spectrum. Each peak belongs to the coincident detection of several photons; thus, to one electron track.

togram. A typical reduced Hough-transformed for one perspective of a frame containing a track (Fig. 10a) is shown in Fig. 10b with the corresponding frame; a "bad frame" is shown in Fig. 10c with the corresponding reduced Hough-transform (Fig. 10d). If a straight line appears in the projection, a clear peak can be seen in the reduced Hough-transform. We integrated in an interval of [-15 °; +15 °] around the bin with the highest bin count and divided this integral by the integral of the remaining histogram. If the ratio was larger than 1 for both projections, the event was regarded in the further analysis, otherwise it was rejected. After these three frame selection steps the resulting number of trajectories was 26 starting from a total of 611 events with meaningful ToA value (< 11810 clock cycles) and a total of 44564 frames. As discussed later, the frame selection probably lead to a selection of tracks in an interval of ≈0.25 mm to ≈ 0.6 mm around the focal plane.

For the three dimensional trajectory reconstruction we "sliced" the two dimensional images along the y-axis, parallel to the x-/z-axis as shown in Fig. 9a. We obtain 512 y-slices in total; 256 y-slices for the xy-plane and 256 slices for the xz-plane. The histograms of two single slices are shown in Fig 9b. The average x-/z- position in every slice is determined by the mean value of a Gaussian fitted to each histogram. The fit is performed with the maximum likelihood method as the number of hits per slice is very low. If the number of hits in the slice is zero, the slice is ignored. If the number of hits in the slice is smaller than 4, the average x-position is used instead of the fit since in these cases the fit frequently failed.

The result of this procedure is shown in Fig. 11b. In this plot, the calculated x-value (on the y-axis) is plotted for every y-slice (on the x-axis). One can see a clear trend belonging to the actual track which is in between deviations due to additional hits on the matrix. Since such hits have the same ToA-value as the actual track, they are most likely reflected

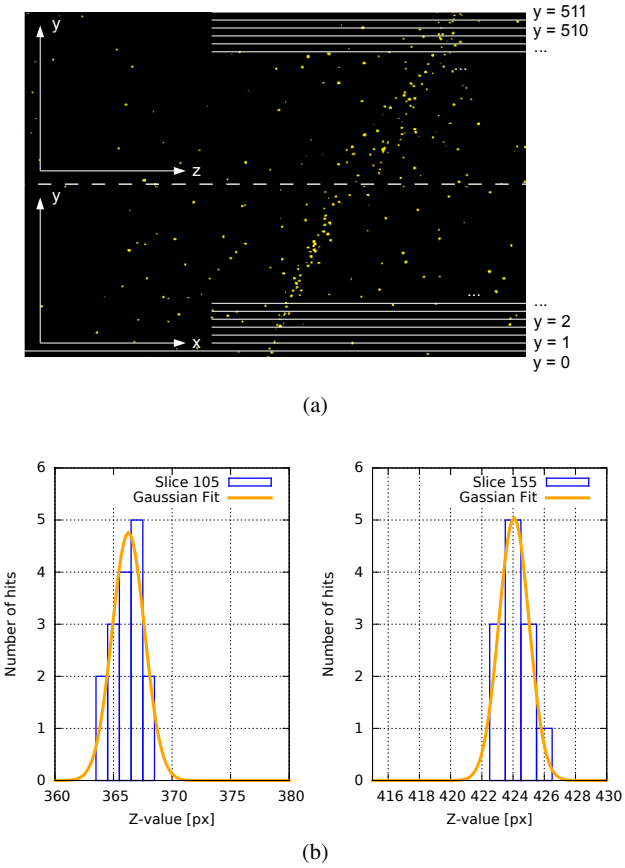

Fig. 9: An illustration of the slicing procedure. Each frame is divided into slices parallel to the x-/z-axis (a). In each slice the mean x-/z-position is determined by a fit with a Gaussian. For each slice we obtain a histogram as in (b). The histograms shown here are summed over several consecutive slices for better statistics.

and scattered photons from the inside and the outside of the scintillator. They do not belong to the track but affect the reconstruction. Therefore, it was necessary to "clean up" the frame before reconstruction.

For this purpose, we calculated the center position for each cluster of adjacent triggered pixels (one photon detection event) and determined the number of neighbouring photon detection events within a chosen radius. After choosing a particular radius, clusters are removed from the frame if the number of neighbours within that radius was below a chosen threshold value. A choice of 30 pixels for the radius and of 8 neighbours for the threshold value produced reasonable and reliable results. One exemplary frame is shown before and after cleanup in Fig. 11a, 11c with the y-slices (Fig. 11b, 11d), respectively. One can see that by this procedure the large deviations from the main line are strongly reduced.

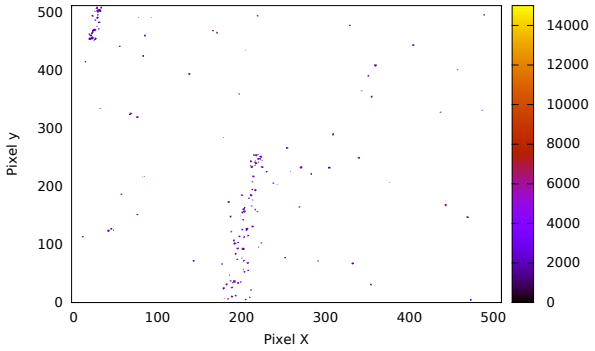

(a)

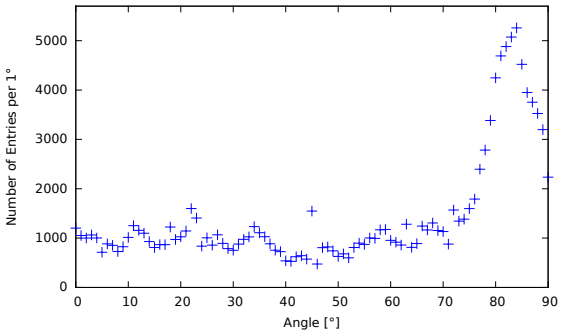

(b)

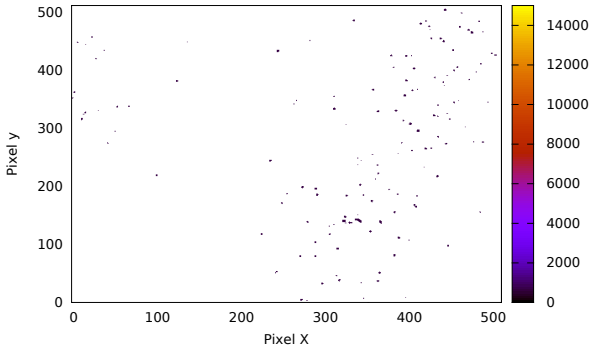

(c)

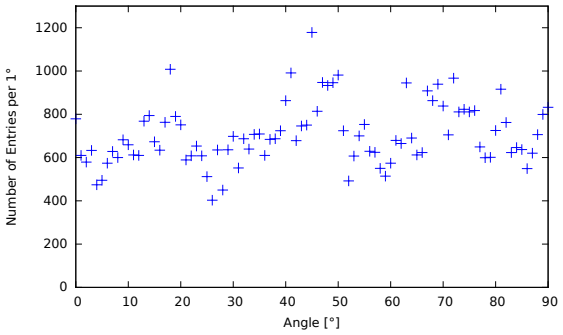

(d)

Fig. 10: Examples of images ((a) and (c)) and their reduced Hough-transforms ((b) and (d)) in the xy-plane. If a track is in the plane, peaks which belong to the direction of the track and a clear plateau appear in the transform. In the opposite case the distribution is flat. The color bar indicates the time-of-arrival measured in each triggered pixel.

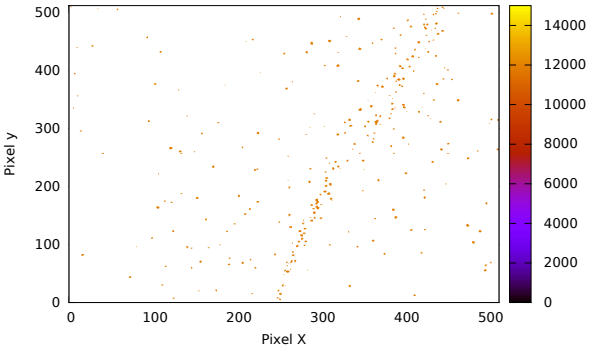

(a)

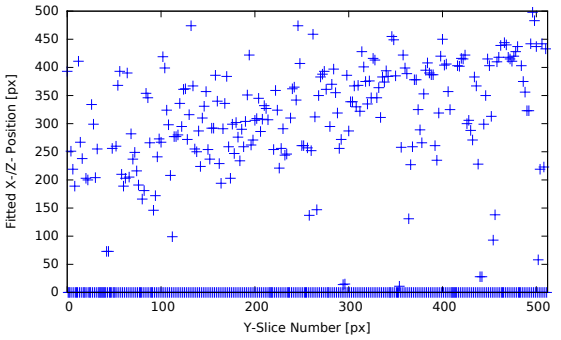

(b)

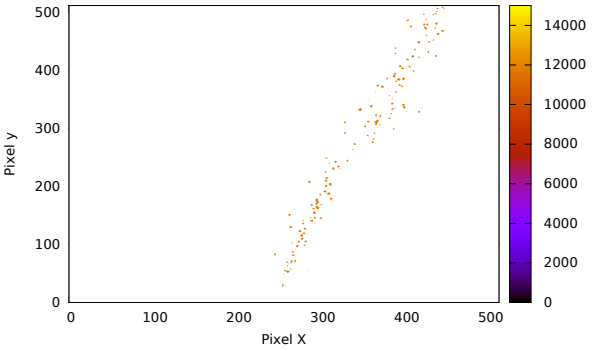

(c)

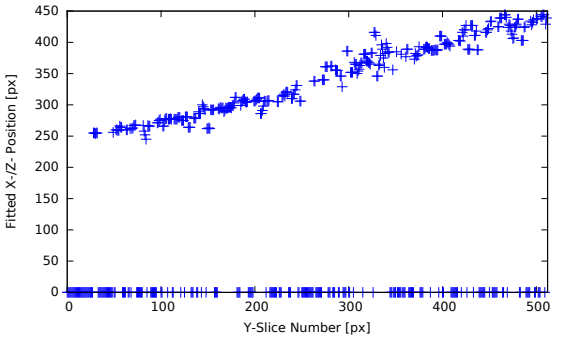

(d)

Fig. 11: Examples of images ((a) and (c)) and the fitted x-/z- position for every y-slice before (b) and after (d) frame cleanup. The color bar indicates the time-of-arrival measured in each triggered pixel.

The reconstruction of the three dimensional trajectories was performed by correlating the y-slices according to their y-value. Every point in the trajectory is referred to as the number of the y-slice, the calculated x-position in that slice in the xy-plane and the calculated z-position in that slice in the zy-plane. As stated above, we did not take an image of the two projections illuminated with a laser that could provide us a precise relation between the xy- and zy-planes. However, in our case of straight tracks a mismatch of the y-coordinate in the xy- and zy-planes causes only a linear shift of the complete track in space and therefore does not affect our resolution results.

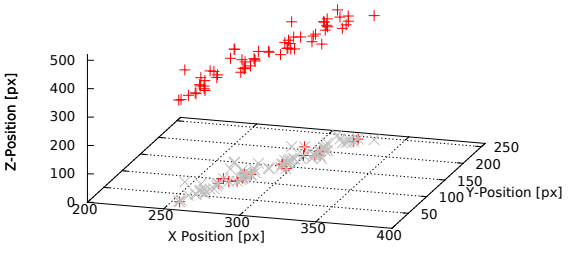

(a)

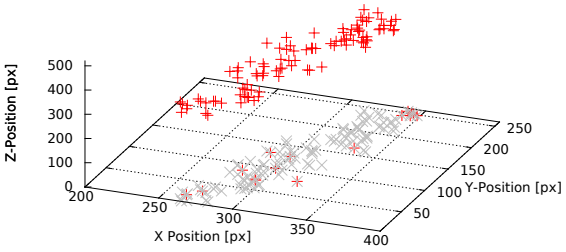

(b)

Fig. 12: Two examples of reconstructed three dimensional electron trajectories. The red crosses are the reconstructed photon positions of the track. The gray crosses represent the projection of the track on the bottom plane for better visibility. The red crosses on the xy-plane are xy-slices that had no matching zy-slices.

4 Results

Two typical reconstructed tracks are shown in Fig 12. As expected one can see straight lines as trajectories. The main reason for the deviations from the straight line or "broadening" is due to the fact that electrons not always propagate through the focal plane of the imaging system and therefore the trajectory is blurred. Depending on the distance from the focal plane, the blurring affects the achievable position resolution. The second limitation to the position resolution is the resolution of the HPD which is governed by the pixel pitch of the ASIC and the distance between the photocathode and the MCP. The intrinsic position resolution of the HPD in the ToA mode is about 160 µm, but the width of the blurring circle can range from zero to several mm depending on the distance from the focal plane.

Before assessing the position resolution, we evaluated the Gaussian width obtained from the Gaussian fits to the slices. This is an estimate for how close two tracks can be next to each other to be distinguishable. This is an important feature since our final goal is to measure curly tracks of low energetic electrons where different parts of the track can be close to each other. The distribution of the Gaussian widths for our selected data (26 events) is shown in Fig. 14.[5]

In order to determine the position resolution, we fitted a straight line to our reconstructed trajectories and considered the distribution of residuals (deviations of the data from the fitted line) in each point in x-direction and z-direction. As the fitted line has very little fit uncertainties due to the large number of points in the track, it can be regarded as the actual track. Hence, the deviations give us an estimate for how close to the actual track a reconstructed point is and how much the positions of the detected photons scatter around the actual track. In Fig 13 the distribution of residuals in x-direction and z-direction is shown.

[5]The histogram contains only 8.6 % of the slices because slices that had less then 4 entries are not included in the histogram. Such slices contain usual only one photon cluster (3 pixels in a row) or a part of it (1 pixel) and therefore no meaningful fit could be performed.

The histogram has a similar shape for both directions. For z-direction the width of the distribution seems to be slightly smaller. The fitted distribution function as shown in the plots is a function of the following form:

$$f(x) = a \cdot \exp\left(-\left(\frac{x}{c}\right)^{b}\right) \tag{1}$$

We obtained this function from a toy Monte-Carlo simulation where the blurring effects of the optical setup are taken into account in the following manner: First, we randomly chose a start position for a photon within an interval of Δd around the focal plane according to a uniform distribution. A uniform distribution is chosen since the electron flux can be regarded as homogeneous over the area of the scintillator. Depending on the distance from the focal plane, photons from one point will not end up in one point on the screen but in a blur circle whose diameter can be calculated as

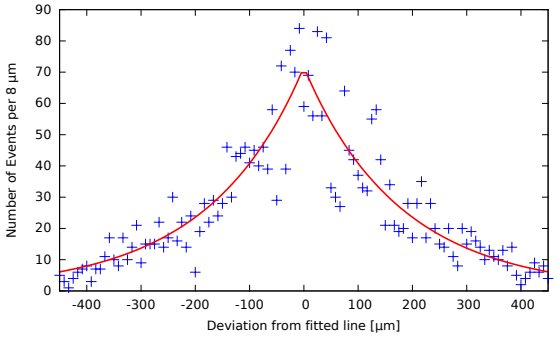

(a) x-direction

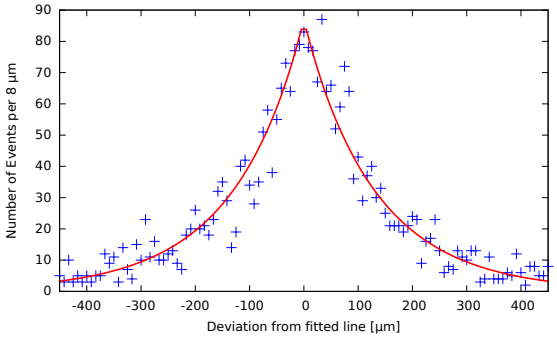

(b) z-direction

Fig. 13: Distribution of the deviations in x- and z-directions. The fit function is given in the text. The resulting fit values are a = 71.8 ± 4.7, b = 0.98 ± 0.11, c = (179.5 ± 16.8) µm (x-direction); a = 87.1 ± 3.8, b = 0.98 ± 0.07, c = (131.1 ± 8.5) µm (z-direction).

$$\sigma_b = f_L \cdot d_L \cdot \frac{1}{\frac{(f_L - g)\cdot g}{\left(1+\sqrt{1+\left(\frac{\Delta d}{g}\right)^2}\right)\cdot \Delta d} + f_L}. \quad (2)$$

Here f_L denotes the focal distance of the lens and d_L its diameter. g is the object distance, i.e. the distance of the focal plane to the lens and Δd is the approximate distance of the photon from the focal plane. The formula can be derived from considerations of geometrical optics as can be found in [22], often used in photography. Then, we calculated the diameter of the blur circle σ_b according to formula 2 depending on the distance Δd from the focal plane. In the final step, the position of the photon on the screen is chosen randomly according to Gaussian distribution with σ_b as its width. We simulated 10^5 events which gives a distribution as shown in Fig. 15. The function which is described by Eq. 1 was obtained as an empirical fit to this distribution.

Although the correspondence of this distribution (Fig. 15) and the result of the experiment is not perfect, the simulation shows that the shape of the distribution is not a Gaussian but can be described by a distribution as given by Eq. 1. We think, that this discrepancy is a result of the frame selection and cleaning where tracks which are too blurred are rejected due to the Hough-transform and photons are removed which are too much off the tracks. This leads to lower tails in the distributions from experimental data.

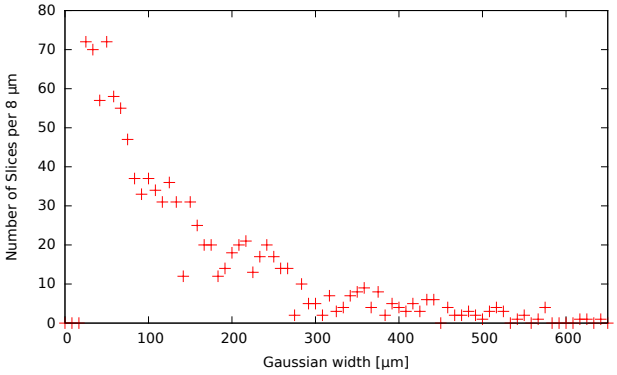

Fig. 14: Distribution of the Gaussian width for the slices of the selected 26 events. The distribution contains only slices which had more than 4 entries (8.6 % of all slices).

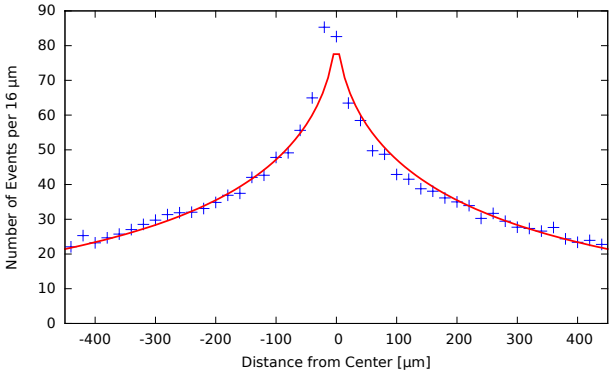

Fig. 15: The distribution obtained from the Monte-Carlo simulation for $\Delta d = 0.4$ mm in same range as the experimental data. The data is scaled to the experimental data by the peak height. The fit function is given in the text. The resulting fit values are a = 86.5 ± 3.2, b = 0.55 ± 0.04, c = (246.3 ± 19) µm

The FWHM of the fitted distribution function was in good agreement for simulation and experiment, when we chose Δd from 0.25 mm to 0.6 mm as the interval around the focal plane in the simulation. Hence, we might conclude that our frame selection lead to a selection of tracks within this interval around the optical plane. The FHWM of the distribution function (Eq. 1) fitted to the experimental data was 248 µm for the x-direction and 170 µm for z-direction. This value can be understood as the position resolution that we obtained with our setup for tracks in a region of roughly 0.25 mm to 0.6 mm around the focal plane.

5 Conclusions and Outlook

We have demonstrated that it is possible to reconstruct three dimensional trajectories of particle propagation through a scintillator by imaging two projections of the track on a pixelated single photon detector (the HPD). With our simple optical setup, which consisted of two mirrors, two lenses and had an optical magnification of 3.3, we could achieve a resolution of 248 µm and 170 µm in x- and z-direction, respectively.

The resolution of the method presented here is mainly limited by the optics used for collecting the scintillation light. However, the main focus was a first "proof-of-principle" demonstration and therefore we concentrated on the easiest possible setup which allowed sufficient light collection efficiency for track imaging, i.e. placing the lens as close to the scintillator as possible. For practical experiments where larger volumes should be imaged a higher depth of focus could be realized with larger lenses and longer image distance between scintillator and lens at the cost of light collection efficiency. If a high light collection efficiency is required for a good energy resolution, photomultipliers can be placed at the other sides of the scintillator for this purpose.

The possible future application could be the search for neutrinoless double beta decay. In this case high resolution particle tracking is a valuable tool to identify background events and enhance the significance of the observation. Another possible application could be high energy single photon Compton imaging where particle tracking could be used to determine the momentum direction of the Compton scattered electron.

An additional application could be beam profile monitoring at particle accelerators: High energetic particles excite the rest gas in the beam pipes which scintillates. An imaging of this beam profile from multiple directions could be useful for beam tuning.

Acknowledgements

We cordially thank the Medipix collaboration for the development of the HPD that we have used. This work was carried out within the Medipix collaboration.

We would like to thanks Ralf Diener and Samuel Ghazaryan from DESY for their support at the T-24 Testbeam line. Also, we would like to thank Dirk Wiedner from the MuPix Group for a share of their beam-time. We would like to thank Felix Just, Andrea Cavanna and Maria Chekhova for their support. Also, we would like to thank Simon Filippov for valuable discussions.

References

1. W.B. Fretter: Ann. Rev. Nucl. Sci. **5** (1955), pp. 145-178
2. C.D. Anderson: Phys. Rev. **43** (1933), pp. 491-494
3. C. Charpak and F. Sauli: Nucl. Instr. Meth. **162** (1979), pp. 405-428
4. H.J. Hilke: Rep. Prog. Phys. **73** (2010), 116201
5. L.M. Montaño: J. Phys.: Conf. Ser. **18** (2005), 368
6. P. Collins et al.: Nucl. Instr. and Meth. A **636** (2011), S185
7. K. Akiba et al.: Nucl. Instr. and Meth. A **661** (2012), pp. 31-49
8. M. Campbell: Nucl. Instr. and Meth. A **633** (2011), pp. 1-10
9. D.D. Ferdinando: Radiat. Meas. **44** (2009), pp. 840-845
10. A. Gallas: Physics Procedia **37** (2012), pp. 151-163
11. S.M. Bilenky and C. Giunti: arXiv:1203.5250 (2012)
12. The EXO-200 Collaboration: Nature **510** (2014), pp. 229-234
13. M. Schumann: arXiv:1310.5217v2 (2013)
14. M. Filipenko et al.: Eur. Phys. J. C **73** (2013), 73:2374
15. T. Michel et al.: AHEP **2013** (2013), 105318
16. V. Álvarez et al.: JINST **8** (2013), P09011
17. E. Aprile and T. Doke: Rev. Mod. Phys. **82** (2010), pp.2053-2097
18. J. Vallerga et el.: JINST **9** (2014), C05055
19. M. Platkevic et al.: Nucl. Instr. Meth. A **591** (2012), pp. 254f
20. D. Turecek et al.: JINST **6** (2011), C01046
21. X. Llopart et al.: Nucl. Instr. Meth. A **581** (2007), pp. 485-494
22. Harold M. Merklinger, Bedford, Nova Scotia: Seaboard Printing Limited (1993), ISBN 0-9695025-2-4
23. R.O. Duda et al.: Comm. ACM **15** (1972), pp. 11-15

IV.2 Comparison of the HPD and the new imaging technique with similar methods

The experience and results obtained in the operation of the HPD can be compared to similar devices, namely the intensified CCD (iCCD), which is presented below. Also, the new imaging technique has similarities with other methods. These are presented in the second subsection.

IV.2.1 Comparison between the HPD and the iCCD

A device which is similar to the hybrid photon detector (HPD) is the so-called iCCD. The structure and functionality of the iCCD is very similar to the HPD: At the top of the device a very thin photocathode is used to covert photons of visible light to photoelectrons. Next, the photoelectrons are accelerated towards a stack of two micro-channel plates (MCPs) where the photoelectrons are amplified. The electron gain is usually between 10^5 and 10^6. The avalanche exiting the stack of MCPs excites an optical phosphor whose light is detected either with a CCD (in the case of the iCCD) or the electrons are detected directly by a 2×2 array of Timepix-ASICs (HPD).

iCCDs are commercially available devices and many different models exist. Here, the comparison is made with reference to the iCCDs fabricated by Andor (Modell iStar 312 [57]) which are typical iCCD devices, widely used for quantum optics experiments. Important characteristics are the quantum efficiency of the photocathode, the timing resolution for coincidence measurements, the spatial resolution and the read-out speed (or rate capability) of the device.

Quantum Efficiency According to the data sheet of the iCCD the quantum efficiency of its photocathode is better for the whole spectral range. No data is provided on the absolute quantum efficiency of the total device (including the MCPs), therefore a direct comparison to our results is not possible. Nonetheless, since the structure of the iCCD is similar to the structure of the HPD, it can be concluded that the absolute quantum efficiency is probably also a factor of about 2 lower than the quantum efficiency of the photocathode only (as in the case of the HPD). Since the photocathode is not specific for the functionality of the particular device (HPD or iCCD), for the next model of the HPD a similar photocathode could be used as for an iCCD to achieve comparable quantum efficiencies.

Position resolution Concerning the position resolution, the Timepix-ASIC has a pixel size of 55 µm whereas the iCCD has a pixel size of 24 µm. CCDs with an even smaller pixel size are commercially available (down to about 2 µm) but the position resolution is not determined by the pixel size only. A centroid method for determining the center of the

electron avalanche after the MCP can substantially improve the spatial resolution. In the case of the HPD it is about 6 µm [59] (compared to pixel size of 55 µm). With the first available HPD (the HPD that we used) the resolution was limited mainly by the distance between the photocathode and the first MCP.

Since the photoelectron has not only a vertical component (perpendicular to the MCP/photocathode) but also a horizontal component (parallel to the MCP/photocathode), its position on the MCP can differ from the position of the incident photon on the photocathode. For the HPD that we used the distance that the photon can travel horizontally was at most about 80 µm, i.e. the position resolution of the HPD was about 160 µm [59]. However, a new HPD was recently fabricated with a so-called "face down window", where the distance between the photocathode and the MCP is reduced to 0.5 mm and therefore a position resolution of 30 µm could be achieved.

The resolution that is achievable with the iCCD is stated to be around 25 µm to 50 µm. The first value is the position resolution that is achievable by the image intensifier (photocathode and MCP) and the second value is provided by the manufacturer as an upper limit for position resolution of the overall device which is calculated roughly as twice the pixel size.

Timing resolution and Read-out speed The frame rate for the HPD that we could use was 4 Hz in the best case (for coincident operation with the APD). Compared to the frame rate possible with the iCCD, 16 Hz (if only a part of the CCDs is read out the frame rate can go even up to 500 Hz [58]), this is rather slow. However, this disadvantage is attributed mainly to the read-out that is connected externally to the HPD. Other read-out techniques exists that allow a frame rate of up to 1.4 kHz [60] for the read-out of a 2×2 Timepix-ASIC but were not employed for the read-out of the HPD yet.

The Timepix clock can be run up to 100 MHz, which allows in principle a time resolution of up to 10 ns per pixel. At a clock of 48 MHz we achieved a jitter of 21 ns (FHWM) in the time coincidence peak which confirms that the achievable timing resolution can be expected to be approximately the inverted clock frequency. The iCCD can be gated with a time resolution of 2 ns. The big difference is, that the iCCD has the same time stamp for every pixel, whereas the HPD provides a timing information for every pixel individually. Thus, within a time window of $11810 \cdot 10\,\text{ns} \approx 120\,\mu\text{s}$[1] the timing information of individual pixels can be recorded and evaluated. For this reason, the HPD does not necessary need an additional trigger (or gate) for coincidence measurements but coincidences can be measured on the whole field of view with a spatial resolution of about 100 µm and a timing resolution up to 10 ns.

A new model of the HPD could employ the successor of the Timepix-ASIC, the so-called Timepix-3 [61]. It has a timing resolution of about 1.6 ns. Furthermore, its read-out

1 11810 is the maximum digital value that a pixel can count for the timing information in one frame.

is not in frames but triggered pixels are read out continuously. Thus, one can imagine a device with a rate capability of up to 8 MHz, a position resolution of 30 µm, a timing resolution of 2 ns in every pixel and very low dead-time for coincidence measurements.

IV.2.2 Other tracking techniques based on light imaging

Of course, besides the new imaging technique which is presented in this work, other scintillation light based techniques exist for tracking of charged particles. Amongst others, these are scintillation fibers [62], the so-called optical time-projection-chamber [64] and "electroluminescence amplified imaging" [68]. These three techniques were chosen here since they are also used to measure three dimensional particle tracks and have in common with the technique developed in this work that scintillation light is used for the trajectory imaging.

Scintillating fiber trackers Scintillating fibers are long light guides that can scintillate and guide their scintillation light on the inside to the end of the fiber. The end of the fiber is optically coupled to a single photon detector such as a photomultiplier or avalanche photodiode (also iCCDs or SiPMs are used in some experiments). If a fiber is penetrated by ionizing radiation the scintillation light generated at the point of interaction is guided through the fiber and measured by the detector at the end of the fiber.

Usually a bunch of such fibers, next to each other, is placed into the pathway of high energetic particles (on the GeV scale), so that multiple scintillating fibers are triggered simultaneously and the data from multiple fibers is combined to reconstruct the particle's trajectory. If half of the fibers are rotated by 90°, 3D trajectories can be reconstructed. Such a detector principle is common for baseline neutrino experiments like NOvA [62].

The diameter of the fibers can range from several centimeters (like in NOvA)[1] to 250 µm [63]. This would allow a voxel size of about 500 µm. However, with this pixel size single electron tracks and two electron track cannot be distinguished any more for the typical track length of MeV electrons in solids [49]. Secondly, the non-sensitive coating of the fibers is about 15 µm thick. In this part of the fiber, a part of the particle's energy is deposited but not measured. This leads to a reduced energy resolution.

At last, for a large volume experiment, many fibers must be used. But since every fiber is a separate piece of material, the surface-to-volume ratio is very high. A low surface-to-volume ratio is crucial for low-background experiments since it is impossible to get rid of contamination on surfaces completely. This is probably the strongest argument against the usage of scintillating fiber trackers for neutrinoless double beta experiments [63].

1 In this case, the core is filled with a liquid scintillator and the light is guided by a wavelength shifting fiber.

Optical time projection chamber The optical time projection chamber is similar to a usual time projection chamber as discussed previously in section II.2.6. The difference between a conventional and an optical time projection chamber is that at the bottom, the charge signal is read out not a by a set of PMTs or meshes but the charge distribution is converted to an optical signal and imaged with an iCCD. The charge signal is converted to a light signal by means of electroluminescent amplification. Usually, an objective is used to enlarge the image of the charge distribution which allows to achieve higher spatial resolution [64].

This kind of device is usually used with a gaseous sensitive medium. Mainly, it was used for detailed studies of dose deposition by ionizing particles. In 2007, it was used to measure the angle correlations in the two proton decay of ^{45}Fe [65]. The position resolution of this device is reported to be around 100 nm. This result was achieved with a TEA (triethylamine) gas at low pressure (10 mbar) and a drift distance of 5 cm. As in the case of the regular TPC, the sensitive volume in height vs. position resolution is limited by diffusion. Therefore, although a really good position resolution can be achieved in low pressure gas (the tracks are rather long) and moderate drift distances, this technique runs into the same problems as a regular TPC concerning the requirements of a $0\nu\beta\beta$ experiment (with tracking).

Track imaging with secondary electrons in a RF-modulated electric field The last technique is maybe the one that reminds most of the method that was investigated in this work. The main idea dates back to 1957 [66]: The sensitive detector volume is filled with a thin gas and observed optically. When an ionizing particle interacts with the gas, the scintillation light is used to switch on an alternating electric field. The field peak strength (about 10 kV/cm) and the frequency (about 20 MHz) are chosen in such a way, that the secondary electrons along the particle's path excite the atoms which emit scintillation light during relaxation. This way from every electron about 10^4 to 10^5 photons are emitted and this amplification is sufficient enough so that tracks can be seen with the naked eye (in a dark room).

In the 80s/90s this concept was discussed again, employing two CCDs which take images of the track from two perspectives, in order to reconstruct a 3D trajectory later [67, 68]. With a gas at low pressure this technique allows a resolution down to 0.6 µm.

The obvious advantage of this technique to the technique presented in this paper is that due to the amplification, the amount of photons is much larger and the collection efficiency is not a highly limiting factor any more. In principle, the distance between the optics and the volume under observation can be increased and one could think about imaging a larger volume (about 30 cm) with sufficient position resolution (about 15 µm)[1]. A disadvantage of this technique might be that the secondary electrons still diffuse (also

1 The calculation is based on Eq. 2 from the publication in sec. IV.1.2 for the width of the blurring circle σ_b and the assumption that from every secondary electron at least one photon is detected.

without any electrical field applied) and if the track is short and the scintillator not fast enough (to trigger the RF-field), the position information is smeared out before the track can be imaged.

Since larger masses are required for $0\nu\beta\beta$, a thin gas is not useful as a target material. The main reason why a thin gas is required for this technique, is the long mean free path of secondary electrons in a thin gas. A long mean free path is necessary for the electrons to acquire sufficient kinetic energy to excite the surrounding atoms by elastic scattering. However, it has been demonstrated that electroluminescent amplification is possible in solid xenon [69]. Also, solid xenon has a fast scintillation component (4 ns) which is faster than the diffusion time of the electron after which the position information is smeared out over a distance larger than 15 µm. Therefore, one could think of demonstrating the functionality of this technique in solid xenon for a later application in a neutrinoless double beta experiment with ^{136}Xe.

At last, it is interesting to state that if the HPD was used as the imaging device with this technique, its time resolution could probably allow to observe the diffusion spread of the charge cloud in real time or even the diffusion of single electrons.

V Summary and Outlook

Within the scope of this thesis several goals were achieved in the field of detector development for neutrinoless double beta experiments. The starting point of the thesis was the successful demonstration of particle identification and background rejection by two-dimensional tracking. The experiments were carried out with a cadmium-telluride Timepix detector. It was demonstrated that α-particles and muons can easily be distinguished from two-electron events since their trajectories are very different. Also, single electrons which are much harder to separate from two-electron events can be identified by neural artificial networks and rejected with an efficiency of about 75 %.

According to simulations, three dimensional tracking yields a much higher separation power between single electron and two-electron events. Thus, new techniques were investigated which would allow for three dimensional tracking in neutrinoless double beta search experiment. It was demonstrated that a hybrid active pixel detector such as the Timepix could be used as a voxel detector if particular, realistic features are added to the functionality. A voxel detector would be able to reconstruct full three dimensional trajectories of particles which propagate through the sensor layer. In a "proof-of-principle" experiment, the current Timepix detector was used to reconstruct three dimensional trajectories of 4.4 GeV electrons with a z-position resolution of 63 µm in the best case.

At the time when this thesis was written, the first Timepix-3 devices were tested with a silicon sensor. The Timepix-3 is the next generation of Timepix detectors. It has the ability to deliver time-over-threshold (deposited energy) and time-of-arrival (time information) data simultaneously for every pixel. Together with a backside read-out, this detector would fulfill all requirements for a voxel detector as proposed in this work. Such a device could also be used for high-energy Compton-imaging where the direction of an incident γ-photon can be determined if its energy is known.

Furthermore, the HEXITEC group has shown that thicker cadmium-telluride sensors (at least 3 mm) can be bump-bonded. With thicker sensors, a medium scale (several tens of kg) neutrinoless double beta experiment with pixelated cadmium-telluride detectors might be realistic in the future. Nonetheless, beforehand an experiment with a ^{208}Tl source as presented here, should be repeated with a voxel detector to determine how good single electron background can be identified by three dimensional tracking. Also, other important quantities like the background level and the composition of background have to be determined. Overall one can state that with currently available pixelated cadmium-telluride detectors a competitive neutrinoless double beta experiment could not be realized.

Since the thickness of the sensor layer (and therefore the scalability of the Timepix technology for low-background experiments) is currently limited by bump-bonding, a new technique for tracking based on the scintillation signal was proposed and investigated. For this purpose a novel device, the hybrid photon detector, was employed. Before the actual tracking experiment the detectors's absolute quantum efficiency was determined. In the range between 535 nm and 570 nm the quantum efficiency drops gradually from about 2.2 % to 0.4 %. In correspondence to the intrinsic geomentry of the detector, the absolute quantum efficiency was 2.2 times lower than the quantum efficiency measured only for the photocathode.

With this device two projections of electron tracks through a plastic scintillator were imaged simultaneously. The electrons had an energy of 5 GeV wherefore their tracks through the scintillator were straight lines. Hence, two projections allowed the reconstruction of full three dimensional tracks with a position resolution ranging from 170 µm to 248 µm. This was a successful "proof-of-principle" demonstration for tracking of charged particles by the scintillation signal in a single layer detector.

Photons travel on straight lines through the scintillator and do not diffuse. In principle this could allow to image particle tracks from a large sensitive volume without diffusion limitations (like in liquid xenon). However, this requires to have a very narrow depth of focus within a large volume. In order realize this, the lenses could be put further away from the sensitive volume which decreases the light collection efficiency. A trade-off between imaging resolution and light collection efficiency is unavoidable.

Maybe, in the case of low event rates (< 0.5 kHz) this problem could be fixed by adaptive optical systems with a real-time variable focus. It could consist of microlenses (devices whose depth of focus can be controlled electrically within few milliseconds) and a two-component scintillator. Such scintillators have a fast decaying component (in the range of nanoseconds) and slow decaying component (in the range of micro- to milliseconds). One optical system would image the track by the fast component with an accuracy of some millimeters and adjust the focal plane of a second optical system with a narrow depth of focus but high imaging resolution. A "proof-of-principle" demonstration for this technique could be the next step towards a scintillation light tracking device based on the technique presented here.

Bibliography

[1] G. Racah: "Sulla simmetria tra particelle e antiparticelle" in Nuovo Cimento **14** (1937), pp.322-328

[2] E. Majorana: "Teoria simmetrica del elettrone e del positrone" in Nuovo Cimento **14** (1937), pp. 171-184

[3] W.H. Furry: "On Transition Probabilities in Double-Beta Disintegration" in Phys. Rev. **56** (1939), 1184

[4] J. Schechter and J.W.F. Valle: "Neutrinoless double-β decay in SU(2)×U(1) theories" in Phys. Rev. D **25** (1982), 2951

[5] F. Simkovic, M.I. Krivoruchenko and A. Faessler: "Neutrinoless double-beta decay and double-electron capture" in Prog. Part. Nucl. Phys. **66** (2011), pp. 451-466

[6] F. Simkovic et al.: "Few active mechanisms of the neutrinoless double beta-decay and effective mass of Majorana neutrinos" in Phys. Rev. D **82** (2010), 113015

[7] K.Zuber: "Neutrino Physics" (2011), ISBN 978-1420064711

[8] S.M. Bilenksy, C. Giunti: "Neutrinoless double-beta decay. A brief review" on arXiv:1203.5250v3 (2012)

[9] J.D. Vergados, H. Ejiri, F. Simkovic: "Theory of neutrinoless double beta decay" on arXiv:1205.0649v2 (2012)

[10] W. Rodejohann: "Neutrino-less double beta decay and particle physics" in J. Mod. Phys. **20** (2011), pp. 1833-1930

[11] S. Goswami, W. Rodejohann: "Constraining mass spectra with sterile neutrinos from neutrinoless double beta decay, tritium beta decay, and cosmology" in Phys. Rev. D **73** (2006), 113003

[12] G.Drexlin et al.: "Current Direct Neutrino Mass Experiments" in Adv. High Energy Phys. **2013** (2013), 293986

[13] G. Cheng et al.: "Dual baseline search for muon antineutrino disappearance at $0.1\,\mathrm{eV}^2 < m_2 < 100\,\mathrm{eV}^2$" in Phys. Rev. D **86** (2012), 052009

[14] T.Köttig: "Sensitivity Studies of CdZnTe Semiconductor Detectors for the COBRA Experiment", PhD Thesis (2012), TU Dortmund

[15] Y. Zdesenko et al: "Sensitivity and discovery potential of the future 2β decay experiments" in J. Phys. G **30** (2004), pp. 971-981

[16] A. Fässler, V. Rodin and F. Simkovic: "Nuclear matrix elements for neutrinoless double-beta decay and double-electron capture" on arXiv:1206.0464 (2012)

[17] F. Simkovic: "Matrix Elements for Neutrinoless Double Beta Decay" in Nucl. Phys. B Proc. Suppl. **229** (2011), pp. 160-164

[18] H.V. Klapdor-Kleingrothaus et al.: "Latest results from the Heidelberg-Moscow double beta decay experiment" in Eur. Phys. J. A **12** (2001), 147

[19] H.V. Klapdor-Kleingrothaus et al.: "Search for neutrinoless double beta decay with enriched ^{76}Ge in Gran Sasso 1990-2003" in Phys. Lett. B **586** (2004), pp. 198-212

[20] Steven R. Elliott, Peter Vogl: "Double Beta Decay" in Annu. Rev. Nucl. Part. Sci. **52** (2002), pp. 115-151

[21] J. Beringer et al. (Particle Data Group): "Review of Particle Physics" in Phys. Rev. D **86** (2012), 010001

[22] J.J. Gomez-Cadenas et al.: "Sense and sensitivity of double beta decay experiments" in JCAP **2011** (2011), 06

[23] The GERDA Collaboration: "The GERDA experiment for the search of $0\nu\beta\beta$ decay in ^{76}Ge" in Eur. Phys. J. C **73** (2013), 2330

[24] The GERDA Collaboration: "Results on Neutrinoless Double-β Decay of ^{76}Ge from Phase I of the GERDA Experiment" in Phys. Rev. Lett **111** (2013), 122503 (arXiv:1307.4720)

[25] B. Schwigenheuer: "Status and prospect of searches for neutrinoless double beta decay" in Ann. Phys. **525** (2013), pp.269-280

[26] The GERDA Collaboration: "The background in the $0\nu\beta\beta$ experiment GERDA" in Eur. Phys. J. C (2014), 74:2764

[27] The GERDA Collaboration: "Pulse shape discrimination for GERDA Phase I data" in Eur. Phys. J. C (2013), 73:2583

[28] J. Argyriades et al.: "Measurement of the background in the NEMO 3 double beta decay experiment" Nucl. Instr. Meth. A **606** (2009), pp. 449-465

[29] Gran Sasso National Laboratory, Official Website: http://www.lngs.infn.it (March 2013)

[30] M.G. Inghram, J.H. Reynolds: "Double Beta-Decay of ^{130}Te" in Phys. Rev. **78** (1950), 822

[31] F.E. Emery, T.A. Rabson: "Average Energy Expended Per Ionized Electron-Hole Pair in Silicon and Germanium as a Function of Temperature" in Phys. Rev. **150** (1965), 2091

[32] J.Cl. Phillipot: "Automatic Processing of Diode Spectrometry Results" in IEEE Trans. Nucl. Sci. **17** (1970), pp.446-488

[33] U. Fano: "Ionization Yield of Radiations. II. The Fluctuations of the Number of Ions" in Phys. Rev. **72** (1947), pp. 26-29

[34] G.F. Knoll: "Radiation Detection and Measurement", New York (1989)

[35] E. Aprile, T. Doke: "Liquid Xenon Detectors for Particle Physics and Astrophysics" in Rev. Mod. Phys. **82** (2010), 2053

[36] P. A. Rodnyi: "Physical Processes in Inorganic Scintillators" by CRC Press (1997), ISBN 978-0849337888

[37] R. Gross: "Manuscript to Lecture, Applied Superconductivity" (2005), Walter-Meiẞsner Institut München

[38] V. Alvarez: "NEXT-100 Technical Design Report (TDR). Executive summary" in JINST **7** (2012), T06001

[39] M. Filipenko et al.: "Characterization of the Energy Resolution and the Tracking Capabilities of a Hydrid Pixel Detector with CdTe-Sensor Layer for a Possible Use in a Neutrinoless Double Beta Decay Experiment" in Eur. Phys. J. C 73 (2013), 2374

[40] S.R. Bandler et al.: "Advances in Small Pixel TES-Based X-Ray Microcalorimeter Arrays for Solar Physics and Astrophysics" in IEEE Trans. on Appl. Supercond. **23** (2013), 2100705

[41] M. Carrettoni: "The CUORE experiment: a search for neutrinoless double beta decay" in J. Phys.: Conf. Ser. **347** (2012), 012031

[42] The EXO-200 Collaboration: "Observation of Two-Neutrino Double-Beta Decay in ^{136}Xe with the EXO-200 Detector" in Phys. Rev. Let. **107** (2011), 212501

[43] The EXO-200 Collaboration: "Search for Majorana neutrinos with the first two years of EXO-200 data" in Nature **510** (2014), pp. 229-234

[44] The KamLAND-Zen Collaboration: "Limit on Neutrinoless $\beta\beta$ Decay of ^{136}Xe from the First Phase of KamLAND-Zen and Comparison with the Positive Claim in ^{76}Ge" in Phys. Rev. Let. **110** (2013), 062502

[45] M. Campbell: "10 years of the Medipix2 Collaboration" in Nucl. Instr. Meth. A **633** (2011), pp.1-10

[46] The EXO Collaboration: "Search for Neutrinoless Double-Beta Decay in ^{136}Xe with EXO-200" in Phys. Rev. Let. **109** (2012), 032505

[47] The KamLAND-Zen Collaboration: "Measurement of the double-β decay half-life of ^{136}Xe with the KamLAND-Zen experiment" in Phys. Rev. C **85** (2012), 045504

[48] T. Gleixner et al.: "Rejection of α-particle background for neutrinoless double beta decay search with pixel detectors" accepted for publication in JINST (2014)

[49] T. Michel et al.: "The Potential of Hybrid Pixel Detectors in the Search for the Neutrinoless Double-Beta Decay of ^{116}Cd" in Adv. High Energy Phys. **2013** (2013), 105318

[50] D.D. Duarte et al.: "Edge effects in a small pixel CdTe for X-ray imaging" in JINST **8** (2013), P10018

[51] E.M. Gushchin, A.A. Kruglov and I.M. Obodovskii: "Electron dynamics in condensed argon and xenon" in Sov. Phys. JETP **55** (1982), 4

[52] M.H. Cohen and J. Lekner: "Theory of Hot Electrons in Gases, Liquids and Solids" in Phys. Rev. **158** (1967), 305

[53] M. Ichige et al.: "Measurement of attenuation length of drifting electrons in liquid xenon" in Nucl. Instr. Meth. A **333** (1993), pp. 355-363

[54] L.S. Miller, S.Howe and W.E. Spear: "Charge Transport in Solid and Liquid Ar, Kr, and Xe" in Phys. Rev. **166** (1968), 3

[55] The EXO-200 Collaboration: "The EXO-200 detector, part I: Detector design and construction", JINST **7** (2012), P05010

[56] D. Klyshko: "Use of two-photon light for absolute calibration of photoelectric detectors" in Sov. J. Quantum Electron. **10** (1980), 1112

[57] Andor iStar 312T Series, Datasheet

[58] C.G. Coates et al: "Optimizing low-light microscopy with back-illuminated electron multiplying charge-coupled device: enhanced sensitivity, speed, and resolution" in J. Biomed. Opt. **9** (2004), pp. 1244-1252

[59] J. Vallerga et al.: "Optical MCP image tube with a quad Timepix readout: initial performance characterization" in JINST **9** (2014), C05055

[60] C. Ponchut et al.: "MAXIPIX, a fast readout photon-counting X-ray area detector for synchrotron applications" in JINST **6** (2010), C01069

[61] M. De Gaspari et al.: "Design of the analog front-end for the Timepix3 and Smallpix hybrid pixel detectors in 130 nm CMOS technology" **9** (2014), C01037

[62] R.B. Patterson: "The NOvA experiment: status and outlook" in Nucl. Phys. B Proc. Suppl. **235**(236) (2013), pp. 151-157

[63] M. Bongrand et al.: "The BiPo detector for ultralow radioactivity measurements" in AIP Conf. Proc. **897** (2007), 14

[64] U. Titt et al.: "A time projection chamber with optical readout for charged particle track structure imaging" in Nucl. Instr. Meth. A **416** (1998), pp. 85-99

[65] K. Miernik et al.: "Two-Proton Correlations in the Decay of ^{45}Fe" in Phys. Rev. Let. **99** (2007), 192501

[66] G. Charpak: “Principe et essais preliminaires d’un nouveau detecteur permettant de photographier la trajectoire de particules ionisantes de un gaz” in J. Phys. Radium **18**, 539-540 (1957)

[67] S.R. Hunter: “Evaluation of a digital optical ionizing radiation track detector” in Nucl. Instr. Meth. A **260** (1987), pp. 469-477

[68] S.R. Hunter et al.: “Optical imaging of charged particle tracks in a gas” in Radiat. Protect. Dosim. **52** (1994), pp. 323-328

[69] E.B. Gordon et al.: “Electronic Excitation of Matrix during Drift of Excess Electrons through Solid Xenon” in JETP **96** (2003), pp. 846-856

List of Publications

[P1] J. Yoo, D. Balakishiyeva, H. Cease, **M. Filipenko**, W.F. Jaskierny, D. Markley, R.B. Pahlka, T. Saab: "Scalability, scintillation readout and charge drift in a kilogram scale solid xenon particle detector" submitted to JINST (2014)

[P2] T. Gleixner, **M. Filipenko**, G. Anton, T. Michel and T. Ziegler: "Rejection of α-particle background for neutrinoless double beta decay search with pixel detectors" accepted for publication in JINST (2014)

[P3] **M. Filipenko**, T. Iskhakov, P. Hufschmidt, G. Anton, M. Campbell, T. Gleixner, G. Leuchs, T. Tick, J. Vallerga, M. Wagenpfeil and T. Michel: "Three dimensional photography of electron tracks through a plastic scintillator" accepted for publication in Eur. Phys. J. C (2014)

[P4] **M. Filipenko**, T. Gleixner, G. Anton and T. Michel: "3D Particle Track Reconstrution in a Single Layer Cadmium-Telluride Hybrid Active Pixel Detector" in Eur. Phys. J. C **74** (2014), 3013

[P5] F. Just, **M. Filipenko**, A. Cavanna, M. Michel, T. Gleixner, M. Taheri, J. Vallerga, M. Campbell, T. Tick, G. Anton, M. V. Chekhova and G. Leuchs: "Detection of non-classical space-time correlations with a novel type of single-photon camera" in Opt. Expr. **22** (2014), 14

[P6] T. Michel, B. Bergmann, J. Durst, **M. Filipenko**, T. Gleixner and K. Zuber: "Measurement of the double K-shell vacancy creation probability in the electron-capture decay of ^{55}Fe with active-pixel detectors" in Phys. Rev. C **89** (2014), 014609

[P7] T. Michel, T. Gleixner, J. Durst, **M. Filipenko** and S. Geißelsöder: "The Potential of Hybrid Pixel Detectors in the Search for the Neutrinoless Double-Beta Decay of ^{116}Cd" in Adv. High Energy Phys. **2013** (2013), 105318

[P8] **M. Filipenko**, T. Gleixner, G. Anton, J. Durst and T. Michel: "Characterization of the Energy Resolution and the Tracking Capabilities of a Hydrid Pixel Detector with CdTe-Sensor Layer for a Possible Use in a Neutrinoless Double Beta Decay Experiment" in Eur. Phys. J. C **73** (2013), 2374

Acknowledgements

Vorwort

Wie ein pfiffiger Leser sofort feststellen wird, fehlt in der unteren Liste ein Dankeschön an meine Eltern, Großeltern und meine Freunde. Das sind alles wunberbare Menschen, die mich nicht nur durch diese Arbeit, sondern schon viel länger begleiten und wissen, wie dankbar ich bin, sie in meinem Leben zu haben. Aus diesem Grund sind sie von dieser Liste ausgenommen - schließlich soll ja dieser Teil der Arbeit nicht länger werden als der Rest davon. Deshalb sind auch sämtliche unten aufgeführten Stichpunkte auch nur als Zusammenfassungen zu betrachten, im Detail müsste ich mich bei allen für noch vieles mehr Bedanken als unten aufgelistet, aber dieses würde zu viel Papier verbrauchen, weshalb ich ausschließlich zwecks Umweltschutz darauf verzichte.

Zusammenfassung der Danksagung

- Als erstes möchte ich meiner Betreuerin und Professorin **Gisela Anton** danken. Sie hatte immer (kritisches!) Vertrauen in die vielen verrückten Ideen, mit denen ich angelaufen kam, und ermöglichte es mir so einige von diesen zu erproben und dabei viele wichtige Teilchenphysik Labore zu bereisen. Sowohl am größten Labor in Europa (CERN) als auch in den USA (FermiLab) durfte ich einen Detektor in den Pionen-Beam halten, wie Klasse ist das denn? Leider, wie das bei Experimenten nunmal so ist, sind einige Sachen auch ordentlich in die Hose gegangen und ich bin sehr dankbar für das Verständnis und die Unterstützung, die ich hatte .. trotz aller Probleme mit Technik, Vakuumleaks, dem amerikanischen Kongress und so einigen weiteren Sachen. Ich hoffe dass ihr diese großartige Neugierde und Offenheit auf Lange erhalten bleibt, so dass noch viele weitere Physik-Querdenker sich in dieser tollen Arbeitsatmosphäre ungehindert entfalten können!
- Gleich als zweites muss ich **Thomas Gleixner** danken, mit dem wir in vier Jahren einiges an tollen Resultaten erarbeiten konnten. Ohne seine Leistungen im erbitterlichen Kampf gegen Segmentation Faults und andere Tücken der elektronischen Datenverarbeitung wäre das Meiste unserer tollen Resultate niemals zustande gekommen. Ich verzichte an dieser Stelle für die vielen tollen “Diskussionen” auf dem Hin- und Rückweg zur Mensa oder zum CERN im Detail zu danken, da eine wissenschaftliche Arbeit sich ja immer anmaßt ein “gewisses Niveau” zu haben :).

- Nummer drei auf dieser Liste ist natürlich **Michael Wagenpfeil**. Es ist toll, dass du dich entschieden hast deine Masterarbeit bei den Chaoten von Zimmer 208 zu machen. Danke für die großartige Arbeit (am DESY, in 108a, bei den Kristallographen, am Rechner in 208..) als auch für den wunderbaren geistigen Dünnpfiff (am DESY, in 108a, am Rechner in 208, auf dem Weg zur Mensa..), der das Niveau bei uns durchgehend auf einem wunderbarem low-level gehalten hat.
- A **Don Thilo M.** quiero mas disculparme que agreceder.. und zwar für den ganzen Stapel an schwarz-weiß Kukuloris, den er korregieren musste. Aber so konnte ich vom Meister selbst lernen und nun denk jeder zweimal darüber nach ob er mir etwas zu korrigieren gibt, falls er es nicht komplett neu schreiben möchte. Ich hoffe doch mal, dass der Stress vorbei ist sobald ich außer Lande bin (haha, un pocito chiste ,-)).
- Desweiteren muss ich mich bei **Jutta Dziwis** für einige Dinge entschuldigen: a) Das Integral aus Länge und Anzahl meiner Dienstreiseanträge verbunden mit meiner Unfähigkeit diese vorschriftsgemäß zu bearbeiten. b) Das Integral aus Choas und Anzahl der Bestellungen für die Xenon-Experimente und c) für meine Unfähigkeit beim Bestellen von Postern dieses mitzuteilen. Ich hoffe wir bleiben trotzdem Freunde :).
- Mein großer Dank geht an alle, die die eigentliche Arbeit getan haben und nicht in der Nase gebopelt, während youtube und facebook im Browser lief. Das sind im besonderen **Thorste Kühn**, **Klaus Kärcher**, **Alfred Kaluza**, **Josef Wissenz** und **Hennry Schlott** vom Physikalischen Institut IV. Es sind **Thomas Spona** und das Team der Mechanikwerkstatt und natürlich das Team der Elektronikwerkstatt. Ich denke, ich habe mehr an wichtigen Dingen von euch gelernt als in so manchem Studiensemester! Vielen Dank für alles!
- I would cordially like to thank **Rolf Schön**, **Enrico Schioppa**, **Jan Vissers**, **Martin van Beuzekom** and the rest of the Medipix group in Amsterdam for a great time at NIKHEF and their amazing help and support with Lasers, Vacuum-Feeds, RelaxD boards and many more. I really appreciate your help and hope to see all of you sometimes!
- Also, I would really like to thank **Jonghee Yoo** for the possiblity to work at FermiLab and collaborate on a solid xenon particle detector! Although experiments with solid xenon are not easy and progress not as fast as we would like to have it, I really hope that the goals that we set will be achieved!
- Mein großer Dank gilt nicht zuletzt **Matthias Weißer** mit dem wir so einigen Spaß im HEX-Bay mit flüssigem Stickstoff und in Grenoble mit frözischer Pasta hatten. Ich hoffe sehr, dass die ersten Messungen mit festem Argon nicht die letzten gewesen sind. Mein Dank gebührt auch **Prof. Magerl**, der es uns ermöglichte am HEX-Bay zu messen, und natürlich den Jungs in der mechanischn Werkstatt dort, die uns immer zu helfen wussten.

- Ein großer Dank geht an **Patrick Hufschmidt** und **Timur Iskhakov** (dessen Namen ich endlich richtig schreiben kann...), die das HPD-Experiment am DESY vorbereitet, aufgebaut und justiert haben. Danke für die tolle Zusammenarbeit.
- Für die tolle Zusammenarbeit möchte ich mich auch bei **Felix Just**, **Andrea Cavanna** und **Maria Chekhova** bedanken. Obwohl es gerade mal 10 mal so lang gedauert hat wie erwartet und es nur einen Dutzend mehr Probleme gab als erwartet, haben wir es geschafft!
- I would like to thank **John Vallerga** for valuable discussions, important comments on everything and his help to start and operate the HPD. Yes, I am a bit slow sometimes but hey, the thing is still running, so it can't be that bad..
- Ich würde gerne der International Max-Planck Research School für die Unterstützung und eine Menge spannenden, neuen Input (insbesondere bei den IMPRS annual meetings) danken. Insbesondere möchte ich mich bei **Heike Schwender** für ihre Geduld bedanken.. Sie hatte es manchmal nicht leicht mit mir..
- Vielen Dank an **Jürgen Hösl**, der mit uns an bis an so manche Grenzen der Strahlungsschutzverordnung gehen musste.
- Ein großer Dank geht an **Ralf Diener**, **Samuel Ghazaryan**, **Dominik Dannheim** und **Dirk Wiedner**, die es uns ermöglichten den DESY Testbeam für unsere Experimente zu nutzen.
- Danke an die **Medipix Collaboration**, insbesondere **Michael Campbell** und **Jerome Alozy** für das Bereitstellen der Medipix und Timepix Detektoren.
- Mein Dank gilt natürlich auch allen Leuten der Erlanger "Medipix Gruppe".
- Danke auch an die Organisatoren und Verantwortlichen des Elitenetzwerks Bayern und des beschleunigten Studieganges in Regensburg und Erlangen für die Möglichkeiten, die sich mir durch diesen Studiengang eröffnet haben.
- Last but not at least, vielen Dank an **Ako Jamil**, **Max Müller**, **Markus Pfaffinger** und **Anastasia Bakst** für Ihre Arbeit mit uns am ECAP und die tollen Ergebnisse, die sie im Rahmen ihrer Abschlussarbeiten, erzielen konnten.

Selbstständigkeitserklärung

Der Verfasser erklärt, dass er die vorliegende Arbeit selbständig, ohne fremde Hilfe und ohne Benutzung anderer als der angegebenen Hilfsmittel angefertigt hat. Die aus fremden Quellen (einschließlich elektronischer Quellen) direkt oder indirekt übernommenen Gedanken sind ausnahmslos als solche kenntlich gemacht.

I hereby declare that I have written this thesis without any help from others and without the use of documents and aids other than those stated above. I have mentioned all used sources and cited them correctly according to established academic citation rules.

Ort, Datum Unterschrift (Mykhaylo Filipenko)